High-Order Simulation of Swirling and Compact Bluff-Body Flows

Thesis submitted for the degree of

Doctor of Philosophy

by

Andrew Brydon

B.Sc.(Hons)

Department of Mathematics and Statistics

Monash University

December 2000

Contents

1 Introduction **1**

2 Numerical Methods **4**

2.1 Introduction 4

2.2 Governing Equations 4

2.2.1 Weak Formulation 5

2.3 Spatial Discretisation 6

2.3.1 Element Representation 6

2.3.2 Element Shape Functions 7

2.3.3 Master Element Transformation 7

2.3.4 Lagrange Polynomials 8

2.3.5 Numerical Quadrature 9

2.4 Temporal Discretisation 9

2.4.1 Steady State - Penalty Pressure Approximation 9

2.4.2 Time Dependant Flow - Projection Equations 13

2.5 Conclusion 15

3 Program Structure **17**

3.1 Overview 17

3.2 Matrix Solution 21

3.2.1 Direct Solvers 21

3.2.2 Iterative solvers 21

3.2.3 Static Condensation 22

3.3 Parallel Partitioning 23

3.4 Parallel Performance 24

3.4.1 Scaled Speedup 25

3.4.2 Fixed Problem Size Speedup 27

3.5 Conclusion 29

4 Vortex Breakdown **30**

4.1 Flow Features 30
4.2 Numerical Studies 34
4.3 Breakdown Mechanisms 35
4.3.1 Flow Configuration 35
4.3.2 Quasi-Cylindrical Approximation 36
4.3.3 Spiral Instability 37
4.3.4 Critical State Transition 38
4.3.5 Trapped Wave Model 40
4.3.6 Critical Rossby Number 42
4.3.7 Vorticity Feedback 42
4.3.8 Shock Jump Analogy 43
4.4 Conclusion 45

5 A Confined Vortex Breakdown Model **46**

5.1 Physical Model 46
5.2 Steady Breakdown 47
5.3 Finite Element Resolution 47
5.4 Breakdown Features 49
5.5 One Dimensional Wave Model 51
5.5.1 Wave Model Results 53
5.6 Unsteady Breakdown 56
5.6.1 Axisymmetric Spectral Element Method 56
5.6.2 Numerical Convergence 57
5.6.3 Transition to Breakdown 59
5.7 Conclusion 63

6 Two Dimensional Wake Flow **64**

6.1 Background 64
6.2 Mesh 64
6.3 Evaluating Strouhal number 66
6.4 Strouhal Number of Cylinder Flow 66
6.5 Effect of Time-Step on Strouhal Number 70
6.6 Two Dimensional Sphere Wakes 71
6.6.1 Sphere Flow features 72

6.7 Conclusion 75

7 Single Sphere Flow **76**

7.1 Problem Geometry 76
7.2 Background 77
7.2.1 Experimental Results 78
7.2.2 Axisymmetric Numerical Results 78
7.2.3 Three Dimensional Numerical Results 79
7.3 Mesh 80
7.4 Simulation Details 82
7.5 Axi-symmetric flow; $Re = 200$ 83
7.6 Non-symmetric steady flow; $Re = 250$ 85
7.7 Shedding flow; $Re = 300$ 90
7.7.1 Flow Quantities 92
7.7.2 Flow Vortex and Vorticity 95
7.7.3 Instantaneous Streamlines 95
7.8 Conclusion 105

8 Double Sphere Flow **106**

8.1 Background 106
8.1.1 Numerical work 106
8.2 Computational Mesh 108
8.3 Simulation Details 109
8.4 Forces on Spheres 109
8.5 Flow Quantities 114
8.6 Flow Vortex and Vorticity 120
8.7 Conclusion 129

9 Conclusion **130**

A Nomenclature **134**

B Cylindrical-Polar Stream Function **136**

List of Figures

3.1 Mesh structure for static condensation 22
3.2 Parallel performance of shear flow problem. Scaled problem size 26
3.3 Parallel performance of shear flow problem. Fixed problem size 28

4.1 Vortex breakdown over a delta wing 31
4.2 Swirling pipe apparatus 31
4.3 Vortex breakdown in divergent pipe flow 32
4.4 Confined cylinder apparatus 33

5.1 Swirling cylinder flow boundaries 46
5.2 Bottom right corner of swirling flow 48
5.3 Existence of breakdown bubbles 49
5.4 Single merged breakdown at $Re = 3500$, $H/R = 3.0$. 50
5.5 Breakdown stream functions, $H/R = 2.5$ 51
5.6 Breakdown stream functions, $H/R = 4.0$ 52
5.7 Axial velocities and minimum eigenvalues for $H/R = 2.5$ 54
5.8 Axial velocities and minimum eigenvalues for $H/R = 4.0$ 55
5.9 Minimum velocity and eigenvalues for $H/R = 2.5$ and $H/R = 4.0$ 56
5.10 Macro-mesh for time-dependant swirling convergence study, $n = 6$, $H/R = 1.5$. 58
5.11 h convergence of swirling cavity spectral element solution 58
5.12 p convergence of swirling cavity spectral element solution 59
5.13 Onset of Vortex Breakdown 60
5.14 Transient vortex breakdown bubble 62

6.1 Spectral element mesh for two dimensional flow past a cylinder 65
6.2 Velocities, pressure and corresponding spectrum 67
6.3 Spectrum for two dimensional shedding wake flow, $Re = 200$ 68
6.4 Strouhal Number vs. Reynolds Number 69

6.5 Effect on timestep on cylinder force 70
6.6 Streamlines of axisymmetric sphere flow. 72
6.7 Sphere flow features at $Re = 200$, $t = 36.5$ 74

7.1 Single sphere problem 77
7.2 Single sphere mesh (M1) with order 4 elements 80
7.3 Single sphere mesh (M2) with order 4 elements 81
7.4 Streamlines around sphere at $Re = 200$ 83
7.5 Vorticity of a single sphere flow at $Re = 200$ 84
7.6 Vortex around a single sphere at $Re = 200$ 84
7.7 Forces on a single sphere at $Re = 250$ 86
7.8 Vortex behind a single sphere at $Re = 250$ 87
7.9 Perspective view of vortex behind a single sphere at $Re = 250$ 88
7.10 Streamlines around a single sphere at $Re = 250$ 89
7.11 Vorticity cross-sections for single sphere flow at $Re = 250$ 91
7.12 Axial vorticity volumes for single sphere flow at $Re = 250$ 92
7.13 Point values in wake of single sphere flow at $Re = 300$ 93
7.14 Forces on single sphere at $Re = 300$ 94
7.15 Axial velocity in wake of sphere, $Re = 300$. Side view 96
7.16 Vortex wake of sphere, $Re = 300$. Top view. 97
7.17 Vortex wake of sphere, $Re = 300$. Side view. 98
7.18 Perspective view of vortex behind Sphere at $Re = 300$ 99
7.19 Axial vorticity in wake of sphere, $Re = 300$. Top view. 100
7.20 Axial vorticity in wake of sphere, $Re = 300$. Side view. 101
7.21 ω_z vorticity in wake of sphere, $Re = 300$. Side view. 102
7.22 Streamlines in wake of sphere, $Re = 300$ side view. 103
7.23 Streamlines in wake of sphere, $Re = 300$. Top view. 104

8.1 Two sphere problem 107
8.2 Forces on two spheres, $S/d = 3.5$ 110
8.3 Forces on two spheres, $S/d = 2.5$ 112
8.4 Forces on two spheres, $S/d = 1.5$ 113
8.5 Stream-wise velocity in wake of two sphere, $Re = 300$. $S/d = 3.5$. Top view . 115
8.6 Stream-wise velocity in wake of two sphere, $Re = 300$. $S/d = 2.5$. Top view . 116
8.7 Stream-wise velocity in wake of two sphere, $Re = 300$. $S/d = 1.5$. Top view . 117
8.8 Stream-wise velocity in wake of two sphere, $Re = 300$. $S/d = 1.5$. Side View . 118

8.9 Stream-wise velocity cross-sections in wake of two sphere, $Re = 300$. $S/d = 1.5$. 119
8.10 Axial vorticity in wake of two sphere, $Re = 300$. $S/d = 3.5$. Top view 121
8.11 Axial vorticity in wake of two sphere, $Re = 300$. $S/d = 2.5$. Top view 122
8.12 Axial vorticity in wake of two sphere, $Re = 300$. $S/d = 1.5$. Top view 123
8.13 Axial vorticity in wake of two sphere, $Re = 300$. $S/d = 1.5$. Side view. 124
8.14 Vortex measure in wake of two sphere, $Re = 300$. $S/d = 3.5$. Top view 126
8.15 Vortex measure in wake of two sphere, $Re = 300$. $S/d = 2.5$. Top view 127
8.16 Vortex measure in wake of two sphere, $Re = 300$. $S/d = 1.5$. Top view 128

List of Tables

2.1 Weights for stiffly stable integration scheme. 14

3.1 Effect of static condensation and preconditioning 23

6.1 Wake length for single sphere. 73
6.2 Axisymmetric sphere flow features. 73

7.1 Boundary layer and element thickness 82

8.1 Drag and lift coefficients of two sphere flows. 112

Summary

In this dissertation, an object-oriented finite element and spectral element library has been developed and applied to two physical problems. The first problem considered is vortex breakdown flow in a confined swirling cylinder, with the second part of the thesis looking at interaction of multiple sphere wake flows.

Chapter 2 introduces a range of numerical techniques used in the current work. A basic outline on the finite element method, along with the spectral element variation of this method, are giving. The penalty pressure treatment is introduced within this context, with the high-order temporal scheme being described for treatment of time-dependant problems.

Chapter 3 overviews the structure of the computation code developed, including aspects of the object-oriented and parallel design of the current code. A series of numerical experiments are reported, showing that the parallel performance is acceptable on the tested hardware.

Chapter 4 deals with vortex breakdown, and reviews a number of existing models of vortex breakdown. Most of these existing models have been applied to vortex breakdown in pipe apparatus. Chapter 5 examines one of the more successful of these theories, the trapped wave model, in the context of the confined apparatus. This theory is shown to do a good job describing the onset of vortex breakdown in the confined apparatus, once allowance is made for the inherently coupled nature of the confined flow.

Chapter 6 outlines a series of simulations on two-dimensional and axisymmetric wake flows, which are used to validate the results of the high-order spectral method for shedding wake flows. In Chapter 7 these results are extended to study flow past a single sphere at higher Reynolds numbers, where the flow develops into a shedding flow with a doubly looped wake.

In Chapter 8 interaction of multiple sphere wakes is examined at a Reynolds number of 300. This Reynolds number corresponds with the shedding wake frequency of the single sphere flow, and is seen to produce a complex interaction between the two shedding wakes.

Chapter 9 provides a summary of the results of this dissertation, along with suggestions of future directions and improvements in the current work.

Candidate's Certificate

This is to certify that the work presented in this thesis has been carried out at Monash University, Australia and has not been previously submitted to any other university or technical institution for a degree or award. The thesis comprises only my original work, except where due acknowledgement is made in the text. The length of this thesis is less than 100,000 words exclusive of figures, tables, appendices and bibliographies.

Andrew Brydon
December 2000

Acknowledgements

I would like to acknowledge the support and guidance of Mark Thompson during the course of this thesis. I would also like to acknowledge the support of the FLAIR group in mechanical engineering at Monash for their on-going support and resources, as well as Joe Monaghan for offering the computational resources of the Epsilon lab. I would like to acknowledge the T-3 group at Los Alamos for their support during my time visiting there.

I would like to thank Robin and James for their technical help, as well as friendship and support during the course of this work.

Finally, I would like to thank all of my friends and family for their love and support over many years. Most of all, I would like to thank Sharen, who's love, support and understanding are beyond words.

Chapter 1

Introduction

Solution of the Navier-Stokes equations has been a core technique in the study of fluid dynamics for over a century. For much of this time, computer simulation has been a key solution technique. However, the gap between what is achievable with current computers and the accurate simulation of fluid flows of interest in the real world is still significant.

Early numerical simulations of fluid flow relied mainly on the finite difference method, which has proved to be quite successful at solving flows on simple flow domains. Recently, the finite volume and finite element methods have become common, especially for use in commercial fluid dynamics codes. There have been literally thousands of papers and hundreds of books written about these techniques. Amongst these, the series of Becker et al. (1981) provides many practical details on the finite element method.

Along with these low order methods, global spectral methods have shown great potential for high accuracy simulation, and have been especially successful in direct numerical simulation of turbulent transition flows. Much of the groundwork for the spectral method is outlined in Gottlieb and Orszag (1977).

A relatively new tool in simulation of fluid dynamics is the spectral element method. While this technique clearly builds on previous finite element and spectral methods, the term spectral element method was first used to describe high order Galerkin methods by Patera (1989). The spectral element method inherits the ability to model complex domains from the finite element method, while also being capable of simulating equations to a high order of accuracy - a property associated with spectral methods. This potential for high order simulations of complex domains, however, comes at a price. The relative complexity of implementation of the finite element method is also associated with the spectral element method. While the spectral element method shares the capability to produce high order

solution with the spectral method, care must be taken to ensure that problems are sufficiently resolved for exponential accuracy to become effective.

As well as advances in the numerical techniques used to study fluid flows, there have also been many changes in the actual computers used to run these simulations. The most drastic change in computing technology has been an exponential increase in the density of computer chips, with a corresponding increase in computer speeds (Moore's 'Law', which states that transistor density will double every 18 months has remained a good approximation for the last 20 years. Moore (1965)). As well as CPU speeds the amount of memory and storage present on systems has increased at a similar pace.

As well as increases in processor speed, the push to simulate more complicated physical flows has led to the increased use of parallel computing; the linking of multiple CPUs to work on a single problem. Implementations of parallel architectures range from relatively small systems sharing common memory, usually on a single motherboard, up to extremely large system with thousands of processors, typically linked by relatively slow networking technology.

While parallel computing offers the possibility of significant speedups for numerical programs, allowing the simulation of significantly more complicated fluid dynamics, this speedup comes at a price. Parallel programming is inherently more complicated than serial programming of the same tasks. Source code compilers, which for decades have successfully optimized FORTRAN programs at levels as good as or better than hand written assembly code, have only been moderately successful at parallelizing programs on shared memory machines. On distributed memory machines automatic code generation is even less advanced, typically working only for so called 'embarrassingly parallel' problems.

With the possibility of high-accuracy parallel simulations in mind, the following work aims to implement and apply a parallel finite element and spectral element code to two fluid dynamics problems. The first problem considered is the simulation of vortex breakdown in a confined torsionally driven cavity. The torsionally driven cavity is a simple apparatus, defined by only two free parameters, and yet exhibits vortex breakdown over a range of parameter values. Vortex breakdown, the sudden change of a compact vortex core into a larger, slowly recirculating zone, is of relevance to the study of industrial mixing problems, aeronautical stability of delta wings and meteorological flows.

In the current work a number of mechanisms for vortex breakdown from existing literature are examined. These mechanisms have typically been formulated in the context of swirling pipe flow, and one of the aims of the current work is to test the effectiveness of one of the more successful pipe breakdown models within the context of confined swirling flow.

The second problem considered in this thesis is the simulation of compact bluff body flow,

which has relevance to many industrial and geophysical applications. In this context, flow past a single sphere and flow past two interacting sphere wakes are studied.

A series of simulations are performed on two dimensional cylinder flow to validate the effectiveness of the current model. Additionally, flow past a single sphere at moderately low Reynolds numbers is simulated over a range where the resulting flow is axisymmetric. Again, this low Reynolds number flow provides and important validation of the current model.

Flow past a sphere is simulated at an increased Reynolds number, where the flow is seen to change from an axisymmetric flow to a simple shedding flow with a single wake frequency. Finally, this work is extending to examine the interaction of shedding wakes behind two spheres at varying separations.

Chapter 2

Numerical Methods

2.1 Introduction

The following chapter outlines the key numerical techniques used in this work. Over the course of this work both the steady and time dependant Navier-Stokes equations are solved. To solve the steady equations, a Galerkin finite element method with a penalty pressure technique is employed. In the penalty method, a penalty term is used to approximate pressure in the steady form of the Navier-Stokes equations, reducing the steady equations to a function of velocity only.

For the numerically more demanding time-dependant swirling and compact bluff body flow simulations a high order spectral element method is employed. While the derivation of the spectral element method is quite similar to that of the finite element method, modifications are introduced to allow for the efficient use of high order elements. For sufficiently smooth problems this method gives the possibility of exponential convergence of the solutions with increasing element order. A multi-step projection scheme with high order boundary conditions is used for the temporal discretisation.

2.2 Governing Equations

The current work deals exclusively with the simulation of the incompressible Navier-Stokes equations. Under the incompressibility assumption the density of the fluid is considered to be constant; an assumption that is equivalent to assuming an infinite sound speed within the fluid. This assumption is reasonable when fluid speeds are considerably less than the sound speed, which is true of the problems parameters considered in the current work.

To reduce the number of free parameters the Navier-Stokes equation can be non-dimensionalised. These equations can be written as

$$\frac{\partial \mathbf{u}}{\partial t} + (\mathbf{u} \cdot \nabla)\mathbf{u} = -\nabla p + \frac{1}{Re}\nabla^2 \mathbf{u} \tag{2.1}$$

$$\nabla \cdot \mathbf{u} = 0 \tag{2.2}$$

where $\mathbf{u}$ is the non-dimensionalised velocity vector and p is the non-dimensionalised pressure. The Reynolds number, Re, is a dimensionless parameter defined as $Re = \frac{UL}{\nu}$ for a typical velocity U, typical length L and kinematic viscosity ν.

The flow domain, indicated here as $\overline{\Omega}$, can be separated into an interior Ω region and a boundary $(\partial\Omega + \Gamma)$. The boundary sections denoted by $\partial\Omega$ represent parts of the boundary with essential boundary conditions and the boundary sections represented by Γ are boundaries with natural (derivative) boundary conditions. The boundary conditions for the Navier-Stokes equations are then written as

$$\mathbf{u} = \mathbf{u}_b \qquad on \qquad \partial\Omega \tag{2.3}$$

$$\frac{\partial \mathbf{u}}{\partial n} = \tau_{\mathbf{n}} \qquad on \qquad \Gamma \tag{2.4}$$

where $\frac{\partial \mathbf{u}}{\partial n}$ is the derivative in the direction normal to the boundary Γ.

2.2.1 Weak Formulation

A common way to solve equations (2.1) and (2.2) is to introduce the method of weighted residuals (see Becker et al. (1981) for full details). In this approach equations (2.1) and (2.2) are integrated over the domain Ω with respect to the vector weight function $\mathbf{w}$ and scalar weight function w_p respectively. The weak form of these equations is

$$\int_\Omega \left(\frac{\partial \mathbf{u}}{\partial t} + (\mathbf{u} \cdot \nabla)\mathbf{u} + \nabla p - \frac{1}{Re}\nabla^2 \mathbf{u} \right) \cdot \mathbf{w} \cdot \mathbf{dx} = 0 \tag{2.5}$$

$$\int_\Omega (\nabla \cdot \mathbf{u})\, w_p \, dx = 0. \tag{2.6}$$

To reduced the order of the highest derivatives, occurring in the viscous and pressure terms, integration by parts is performed on equation (2.5) to yield

$$\begin{aligned} &\int_\Omega \left(\frac{\partial \mathbf{u}}{\partial t} + (\mathbf{u} \cdot \nabla)\mathbf{u} \right) \cdot \mathbf{w} \ \mathbf{dx} \\ &+ \int_\Omega \left(\frac{1}{Re}\nabla \mathbf{u} \cdot \nabla \mathbf{w} - p\nabla \cdot \mathbf{w} \right) \ \mathbf{dx} \\ &+ \int_{\partial\Omega+\Gamma} \nabla\, (\mathbf{u} \cdot \mathbf{n}) \cdot \mathbf{w}\, ds = 0. \end{aligned} \tag{2.7}$$

On the essential boundary $\partial\Omega$ values of $\mathbf{u}$ are known and need not be solved. The corresponding weight functions $\mathbf{w}$ are also set to zero at these points to maintain a consistent system of equations. On the boundary Γ the value of $\nabla\mathbf{u}\cdot\mathbf{n}$ is the specified boundary value $\tau_{\mathbf{n}}$ from equation (2.4). Substituting these boundary values simplifies the weak form of the Navier-Stokes equations to

$$\int_\Omega \left(\left(\frac{\partial \mathbf{u}}{\partial t} + (\mathbf{u}\cdot\nabla)\mathbf{u} \right) \cdot \mathbf{w} + \frac{1}{Re}\nabla\mathbf{u}\cdot\nabla\mathbf{w} - p\nabla\mathbf{w} \right) \mathbf{dx} = -\int_\Gamma \tau_{\mathbf{n}}\mathbf{w}\, ds \tag{2.8}$$

$$\int_\Omega (\nabla\cdot\mathbf{u})\, w_p\, dx = 0 \tag{2.9}$$

with the essential boundary condition

$$\mathbf{u} = \mathbf{u}_b \quad on \quad \partial\Omega. \tag{2.10}$$

2.3 Spatial Discretisation

To approximate the flow equations in the spacial coordinates the finite element method, along with the spectral element method variation, have be used in the current work. Both of these techniques rely on the underlying idea of splitting the simulation domain into a number of discrete areas, generally refered to as elements.

2.3.1 Element Representation

A key feature of finite and spectral elements is the reduction of the global system (2.8) and (2.9) to a series of coupled element equations. This greatly simplifies the solution process on complex domains, as the system can be built on a geometrically regular domain (the master element) and assembled back into a global system for solution. Since the master element is defined as having a regular coordinate system, the same element construction routine can be used for geometrically different elements.

The composition of the global domain Ω from n_e elements Ω_e, and the corresponding splitting of the boundary Γ into n_{be} boundary elements Γ_{be}, gives the element version of equations (2.8) and (2.9) as

$$\sum_{n_e} \left[\int_{\Omega_e} \left(\left(\frac{\partial \mathbf{u}}{\partial t} + (\mathbf{u}\cdot\nabla)\mathbf{u} + \nabla p \right) \cdot \mathbf{w}_e + \frac{1}{Re}\nabla\mathbf{u}\cdot\nabla\mathbf{w}_e \right) \mathbf{dx} \right] = -\sum_{n_{be}} \int_{\Gamma_{be}} \tau_{\mathbf{n}}\mathbf{w}_e\, ds \tag{2.11}$$

$$\sum_{n_e} \left[\int_\Omega (\nabla \cdot \mathbf{u})\ w_p \, \mathbf{dx} \right] = 0 \tag{2.12}$$

This decomposition is made possible by restricting the element weight functions $\mathbf{w}_e$ to be non-zero only on a corresponding element Ω_e. Nodes on the boundaries of elements will usually be members of adjoining elements (or boundary elements), and it is these nodes that couple the elements together into a global system.

2.3.2 Element Shape Functions

To produce a discrete representation of (2.11), the flow variables $(\mathbf{u}, p)$ are represented as a sum of local trial functions,

$$\mathbf{u} \approx \sum_{s=1}^{n} \hat{\mathbf{u}}_s \hat{\phi}_s \tag{2.13}$$

$$p \approx \sum_{s=1}^{m} \hat{p}_s \hat{\psi}_s \tag{2.14}$$

where n and m are the respective orders of approximation of the trial functions $\hat{\phi}$ and $\hat{\psi}$. In general n and m will not be equal.

The finite element and spectral element methods are both examples of Galerkin methods where the test functions $(\mathbf{w}, w_p)$ are chosen from the same space of functions as the trial functions, so for each element the set of weight functions

$$\mathbf{w} = \hat{\phi}_t^{(\alpha)} \mathbf{e}_{(\alpha)}, \qquad t = 1..n \tag{2.15}$$

$$w_p = \hat{\psi}_t, \qquad t = 1..m. \tag{2.16}$$

are used.

2.3.3 Master Element Transformation

To avoid having to build the local equations in a different coordinate system for each element, it is convenient to transform the equations to a so-called master element. This element is defined with coordinates (ξ, η, ζ) in the range $-1 \leq \xi, \eta, \zeta \leq 1$.

To perform the change in coordinates from master element to global coordinates, the positions can be expanded as a sum of shape functions in the same way as equation (2.14), so that

$$\mathbf{x}(\xi) \approx \sum_{j}^{n} \mathbf{x}_j \hat{\phi}_j(\xi) \tag{2.17}$$

where the constants $\mathbf{x}_j$ are the nodal positions supplied by the mesh geometry.

To perform differentiation with respect to the global coordinate $\mathbf{x}$, the Jacobian matrix J is constructed by differentiating equation (2.17). In three dimensions the Jacobian is a 3×3 matrix, with component (α, β)

$$J^{(\alpha,\beta)} = \frac{\partial x^{(\alpha)}}{\partial \xi^{(\beta)}} = \sum_{j=1}^{n_e} x_j^{(\alpha)} \frac{\partial \hat{\phi}_j(\xi)}{\partial \xi^{(\beta)}} \tag{2.18}$$

where $\mathbf{x} = (x^{(1)}x^{(2)}, x^{(3)})$. Inversion of the Jacobian matrix, which is once again a 3×3 matrix, gives

$$J^{-1} = \left(\frac{\partial \xi^{(\alpha)}}{\partial x^{(\beta)}} \right) \tag{2.19}$$

so that the global derivative of the shape functions ϕ are

$$\frac{\partial \hat{\phi}_j}{\partial x^{(\alpha)}} = \sum_{\beta=1}^{3} J^{-1(\alpha,\beta)} \frac{\partial \hat{\phi}_j}{\partial \xi^{(\beta)}} = \sum_{\beta=1}^{3} \frac{\partial \xi^{(\beta)}}{\partial x^{(\alpha)}} \frac{\partial \hat{\phi}_j}{\partial \xi^{(\beta)}} \tag{2.20}$$

2.3.4 Lagrange Polynomials

Lagrange polynomials have the property that

$$h_p(x_q) = \delta_{pq} \tag{2.21}$$

where the delta function $\delta_{pq} = 1$ when $p = q$ and zero otherwise, and the points x_p represent the nodal points of the polynomial. The Lagrange polynomial can be written as

$$h_p(x) = \frac{\prod_{q=0, q\neq p}^{P} (x - x_q)}{\prod_{q=0}^{P} (x_p - x_q)} \tag{2.22}$$

The choice of how to place the nodal points of the element is critical to the efficiency of the Galerkin techniques. For finite elements (which are almost always low order), a regular spacing of internal element nodes is common. To achieve accurate integration, Gauss-Legendre numerical quadrature is used. While this is the most accurate form of integration, it requires a loop over the quadrature points, and for each quadrature point a loop over all of the element shape functions. As the order of the polynomials (and therefore quadrature) is increased this process becomes increasingly expensive.

In the spectral element method the nodal points are place on the zeros of the Gauss-Lobatto-Legendre (GLL) polynomials. This is then combined with Gauss-Lobatto-Legendre quadrature which sums quadrature weights at the same GLL zero points. Using equation (2.21) it is then possible to loop over the quadrature points, which are also the nodal points, once only. Since a second loop over the nodal points is not required, the efficiency of the element sum is dramatically improved for high order elements.

2.3.5 Numerical Quadrature

To effectively integrate the equations (2.8) and (2.9) it is necessary to use numerical quadrature. As discussed in the previous section, the choice of quadrature rule will greatly affect the efficiency of the numerical method.

For low order elements, as used in the finite element method, the number of quadrature and nodal points is low and it is benificial to use the most accurate quadrature scheme available. Gauss-Legendre quadrature is employed. This quadrature rule sums over quadrature points in the interior of the elements. A one dimensional Gauss-Legendre quadrature with k points will integrate a polynomial of order $(2k + 1)$ exactly, and the multi-dimensional quadature is simply generated from a tensor product of the one dimensional quadratures.

For the higher order spectral element method the use of Gauss-Legendre quadrature becomes excessively expensive. Instead, the Gauss-Lobatto-Legendre quadrature points are used. This quadrature rule includes both end points of the domain. By choosing the nodal points to be at the integration points of the quadrature rule, the time complexity of the integration loop is reduced substantially.

When using the finite element method to solve the Navier-Stokes equations in cylindrical polar coordinates, the use of Gauss-Legendre quadrature provides an additional advantage. Integration of elements with nodes on the the pole ($r = 0$) need only be evaluated on the interior of the element (on the Gauss-Legendre quadrature points). This means that the presence of terms in the Navier-Stokes involving the reciprocal of r do not pose a problem. When the spectral element method is in use, however, the same is not true; the quadrature points are the nodal points which will include the axis. To resolve this, Gauss-Radau-Legendre quadrature is used on these elements. The Guass-Radau-Legendre points include only one end point (in this case $\xi = 1$) rather than both. The nodal points of the element are also adjusted to sit on the Gauss-Radua-Legendre points which do not involve the pole. Use of this quadrature rule allows for exponential convergence of the spectral element method for problems involving a coordinate singularity.

2.4 Temporal Discretisation

2.4.1 Steady State - Penalty Pressure Approximation

The seemingly simplest approach to dealing with time derivatives in the Navier-Stokes equations is to make the assumption of steady flow, which involves neglecting the $\frac{\partial u}{\partial t}$ terms from the Navier-Stokes equations. With time derivatives dropped from equation (2.8) the steady

Navier-Stokes system in weak form is

$$\int_\Omega \left((\mathbf{u}\cdot\nabla)\mathbf{u} + \nabla p - \frac{1}{Re}\nabla^2\mathbf{u} \right) \cdot \mathbf{w}\ \mathbf{dx} = 0 \tag{2.23}$$

$$\int_\Omega \nabla\cdot\mathbf{u}\ \mathbf{dx} = 0 \tag{2.24}$$

giving a coupled set of equations in three velocity components ($\mathbf{u}$) and one pressure variable (p). This coupling of the pressure with all velocity components leads to a large (and therefore computationally expensive) system to be solved. As a way of decoupling the pressure variable, the penalty method (Chorin (1967)) is introduced, with the continuity equation approximated as

$$\nabla\cdot\mathbf{u} \approx -\frac{1}{\lambda}p \tag{2.25}$$

where λ is a large constant. Clearly, as $\lambda \to \infty$ equation (2.25) approaches the continuity equation (2.2). This modified continuity equation can then be used to provide an approximation for pressure in the momentum equation to give the following modified momentum equation

$$\int_\Omega \left((\mathbf{u}\cdot\nabla)\mathbf{u}\cdot\mathbf{w} + \lambda(\nabla\cdot\mathbf{u})(\nabla\cdot\mathbf{w}) + \frac{1}{Re}\nabla\mathbf{u}\cdot\nabla\mathbf{w} \right)\ \mathbf{dx} = 0. \tag{2.26}$$

Although the modified equation is no longer dependant on the pressure, the equation is still non-linear due to the presence of the advection term $(\mathbf{u}\cdot\nabla)\mathbf{u}$. To deal with this non-linearity, the solution procedure employed is to start with an initial guess for $\mathbf{u}$ and apply a global Newton-Raphson approximation to equation (2.26).

The pressure term $\lambda(\nabla\cdot\mathbf{u})(\nabla\cdot\mathbf{w})$ acts to couple the velocity components of the equations, requiring the solution of (2.26) as a coupled system of velocity components. Another feature of this term is the presence of the large constant λ. The discretisation of the the $(\nabla\cdot\mathbf{u})(\nabla\cdot\mathbf{w})$ term results in the presence of off-diagonal terms that are of similar size to the diagonal matrix terms. When this term is multiplied by the penalty parameter a very poor condition number for the global system results. This poor condition will causes very slow convergence when iterative techniques are used to solve the system. As a result of this poor conditioning, the only viable way to solve the penalty system is by the use of direct solvers.

Equation (2.26) can be analytically linearized using the Newton-Raphson method. Starting with an initial guess for velocity $\mathbf{u}_0$ the linearized momentum equation

$$\int_\Omega \left((\mathbf{u}_0\cdot\nabla)\delta\mathbf{u}\cdot\mathbf{w} + (\delta\mathbf{u}\cdot\nabla)\mathbf{u}_0\cdot\mathbf{w} + (\lambda\nabla\cdot\delta\mathbf{u})(\nabla\cdot\mathbf{w}) + \frac{1}{Re}\nabla\delta\mathbf{u}\cdot\nabla\mathbf{w} \right)\ \mathbf{dx} = \tag{2.27}$$

$$-\int_\Omega \left((\mathbf{u}_0\cdot\nabla)\mathbf{u}_0\cdot\mathbf{w} + (\lambda\nabla\cdot\mathbf{u}_0)(\nabla\cdot\mathbf{w}) + \frac{1}{Re}\nabla\mathbf{u}_0\cdot\nabla\mathbf{w} \right)\ \mathbf{dx} \tag{2.28}$$

is solved iteratively by incrementing $\mathbf{u}_0$ by $\delta\mathbf{u}$ at each iteration.

The Newton-Raphson method theoretically exhibits second order convergence and in the current work has been seen to converge within three or four iterations. It does, however, have a relatively small radius of convergence which requires an accurate initial value $\mathbf{u}_0$; a poor initial guess causes the iterative process to diverge. An appropriate initial guess is obtained by using a lower Reynolds number result as the initial guess for the current Reynolds number solution. Higher Reynolds number results are similarly attained by stepping up in Reynolds number.

The major disadvantage of the direct solution technique is that the sparse matrix system is filled in by factorisation. The sparse global matrix becomes a dense banded system, with the bandwidth being determined by the geometry of the mesh. While the actual value of the bandwidth is mesh-dependent it will typically be proportional to $nn^{(\frac{1}{nd})}$ where nn is the number of mesh nodes and nd is the mesh dimension. This produces a total matrix storage requirement proportional to $nn^{(1+\frac{1}{nd})}$. For a 100×100 first order mesh in two dimensions, this requires approximately $2 \times 100^2 \times (100 + 100) \times 2$ matrix values or 64 megabytes of storage in double precision. While this is within the limits of current desktop machines, a three-dimensional $100 \times 100 \times 100$ mesh requires approximately $3 \times 100^3 \times (100^2 + 100^2) \times 3 = 1.8 \times 10^{11}$ matrix values, or 1.44 Terabytes of storage. Clearly the penalty method is not suitable for three-dimensional or high resolution simulations.

Finite Element Approximation

To employ the finite element technique to solve the the equations (2.27), the velocity $\mathbf{u}$ is approximated in terms of the element shape functions $\hat{\phi}_j$,

$$\mathbf{u} = u^{(\alpha)}\mathbf{e}_\alpha \approx \sum_s \hat{u}_s^{(\alpha)}\hat{\phi}_s\mathbf{e}_\alpha \tag{2.29}$$

where $\mathbf{e}_\alpha$ is the unit vector in the α coordinate direction. For Cartesian flows the coordinate directions $(\alpha_1, \alpha_2, \alpha_3)$ are identified with the directions (x, y, z).

Similarly, the element test functions are element shape functions denoted as $\hat{\psi}_t$ where the index t indicates a given test function in the range $1 \leq t \leq m$, so that the family of test functions is

$$\mathbf{w} = \left\{w_t^{(\alpha)}\mathbf{e}_\alpha\right\} = \left\{\hat{\psi}_t^{(\alpha)}\mathbf{e}_\alpha\right\} \tag{2.30}$$

Each term in equation (2.26) can then be approximated using these expansions. These element expansions are

$$\int_\Omega (\nabla u^{(\alpha)}) \cdot (\nabla w^{(\alpha)})\,\mathbf{dx} \quad = \quad \int_\Omega \left(\frac{\partial u^{(\alpha)}}{\partial r}, \frac{\partial u^{(\alpha)}}{\partial z}\right) \cdot \left(\frac{\partial w^{(\alpha)}}{\partial r}, \frac{\partial w^{(\alpha)}}{\partial z}\right) \mathbf{dx}$$

$$= \int_\Omega \sum_{\beta=1}^{3} \frac{\partial u^\alpha}{\partial x^{(\beta)}} \frac{\partial w^\alpha}{\partial x^{(\beta)}} \, \mathbf{dx}$$

$$\approx \int_\Omega \sum_{\beta=1}^{3} \hat{u}_s^{(\alpha)} \frac{\partial \hat{\phi}_s}{\partial x^{(\beta)}} \frac{\partial \hat{\psi}_t}{\partial x^{(\beta)}}, \, \mathbf{dx}, \tag{2.31}$$

$$\int_\Omega (\mathbf{u} \cdot \nabla)\mathbf{u} \cdot \mathbf{w} \, \mathbf{dx} \approx \int_\Omega \sum_{\beta=1}^{3} \left(\sum_{\gamma=1}^{3} u_t^{(\gamma)} \hat{\phi}_t \frac{\partial}{\partial x^{(\gamma)}} \right) \hat{u}_s^{(\beta)} \psi_t^{(\beta)} \, \mathbf{dx}, \tag{2.32}$$

and

$$\int_\Omega (\nabla \cdot \mathbf{u})(\nabla \cdot \mathbf{w}) \, \mathbf{dx} \approx \int_\Omega \left(\sum_{\beta=1}^{3} \frac{\partial \hat{\phi}_s}{\partial x^{(\beta)}} \hat{u}_s^{(\beta)} \right) \left(\sum_{\alpha=1}^{3} \frac{\partial \hat{\psi}_t^{(\alpha)}}{\partial x^{(\alpha)}} \right) \, \mathbf{dx}. \tag{2.33}$$

The integration over the domain Ω is performed using Gaussian quadrature so that the shape functions $\hat{\phi}$ and $\hat{\psi}$ in the previous equations are evaluated at the Gaussian quadrature points.

Axisymmetric Cylindrical Polar Coordinates

As written, equations (2.1) and (2.2), and consequently equation (2.27), are only valid in Cartesian coordinates. Extra terms are needed to allow for the simulation of flow in axisymmetric cylindrical-polar coordinates. To do this, it is useful to define the operator

$$\nabla_c = (\frac{\partial}{\partial r}, 0, \frac{\partial}{\partial z}) \tag{2.34}$$

where the coordinate directions are identified with the cylindrical polar coordinates (r, θ, z). This allows the Navier-Stokes equations to be written as a group of terms resembling the Cartesian expressions, with additional terms to allow for the change of coordinate system. Using this notation, the axisymmetric form of equation (2.26) is

$$\begin{aligned} \int_\Omega \left((\mathbf{u} \cdot \nabla_c)\mathbf{u} \cdot \mathbf{w} + (\lambda \nabla_c \cdot \mathbf{u})(\nabla_c \cdot \mathbf{w}) + \frac{1}{Re} \nabla_c \mathbf{u} \cdot \nabla_c \mathbf{w} \right) \, \mathbf{dx} \\ + \int_\Omega \left(\frac{-u_\theta^2}{r}, \frac{u_r u_\theta}{r}, 0 \right) \cdot \mathbf{w} \, \mathbf{dx} \\ + \lambda \int_\Omega \left(\frac{u_r u_\theta}{r^2} + \frac{u_r}{r} \left(\frac{\partial w_r}{\partial r} + \frac{\partial w_z}{\partial r} \right) + \frac{w_r}{r} \left(\frac{\partial u_r}{\partial r} + \frac{\partial u_z}{\partial r} \right) \right) \, \mathbf{dx} \\ + \frac{1}{Re} \int_\Omega \left(-\frac{u_r}{r^2}, -\frac{u_\theta}{r^2}, 0 \right) \cdot \mathbf{w} \, \mathbf{dx} = 0 \end{aligned} \tag{2.35}$$

With the change of coordinates the integral weighting $\mathbf{dx}$ becomes $rdrdz$, since the integral over θ gives a constant 2π for all equations. This leaves two terms in equation (2.35) that involve $1/r$ terms, even after being multiplied by the integral weighting. In the finite element method the pole singularity is avoided by using the Gauss-Legendre quadrature weights,

which do not include the points on the edge of the element corresponding to $r = 0$. When using the spectral element method, Gauss-Radau-Legendre quadrature is used on elements containing the $r = 0$ axis. Since the nodal points are chosen to correspond with the quadrature points in the spectral element method, nodal points on the axis are not required, which resolves the problem of the coordinate singularity.

Applying the method of weighted residuals to the extra terms gives the following additional terms in the element matrices. For the diffusion contribution,

$$\begin{aligned} \frac{1}{Re}\int_\Omega (-\frac{u_r}{r^2}, -\frac{u_\theta}{r^2}, 0)\cdot \mathbf{w}\,\mathbf{dx} &= \frac{1}{Re}\int_\Omega \left(-\frac{u_r}{r^2}w_r - \frac{u_\theta}{r^2}w_\theta\right)\mathbf{dx} \\ &\approx \frac{1}{Re}\int_\Omega \sum_{\beta=1,2} -\frac{u_s^{(\beta)}}{r^2}\hat{\phi}_s\hat{\psi}_t^{(\beta)}\,\mathbf{dx}. \end{aligned} \tag{2.36}$$

For the convection terms,

$$\int_\Omega \left(-\frac{u_\theta^2}{r}, \frac{u_r u_\theta}{r}, 0\right)\cdot \mathbf{w}\,\mathbf{dx} \approx \int_\Omega \left(\sum_p \left(-u_p^{(1)}\hat{\phi}_p\hat{\psi}_t^{(1)} + u_p^{(2)}\hat{\phi}_p\hat{\psi}_t^{(2)}\right)\frac{u_s^{(2)}\hat{\phi}_s}{r}\right)\mathbf{dx} \tag{2.37}$$

and for the penalty pressure

$$\begin{aligned} &\lambda\int_\Omega \left(\frac{u_r u_\theta}{r^2} + \frac{u_r}{r}\left(\frac{\partial w_r}{\partial r} + \frac{\partial w_z}{\partial r}\right) + \frac{w_r}{r}\left(\frac{\partial u_r}{\partial r} + \frac{\partial u_z}{\partial r}\right)\right)\mathbf{dx} \approx \\ &\lambda\int_\Omega \left(\frac{\hat{\phi}_s\hat{\psi}_t^{(1)}}{r}\hat{u}_s^{(1)} + \sum_{\alpha=1,3}\frac{\partial\hat{\psi}_t^{(1)}}{\partial x^\alpha}\hat{\phi}_s\hat{u}_s^{(1)} + \sum_{\alpha=1,3}\frac{\partial\hat{\phi}_s}{\partial x^{(1)}}\hat{u}_s^{(\alpha)}\hat{\psi}_t^{(1)}\right)\mathbf{dx}. \end{aligned} \tag{2.38}$$

2.4.2 Time Dependant Flow - Projection Equations

While the steady approximation offers a simple implementation, a desire to simulate transient phenomenon requires the use of a more sophisticated temporal discretisation. While it is theoretically possible to solve the equations (2.1) and (2.2) as a large coupled non-linear system in $\mathbf{u}$ and p at each timestep, it is more computationally efficient to break down this task into smaller components.

In the projection technique of Chorin (1968), the Navier-Stokes equations are solved by performing the following two-step process. Firstly, the momentum equation (2.1) is evolved without considering the pressure term,

$$\frac{\mathbf{u}^* - \mathbf{u}^n}{\Delta t} + (\mathbf{u}^n\cdot\nabla)\mathbf{u}^n = \frac{1}{Re}\nabla^2\mathbf{u}^n \tag{2.39}$$

to obtain an intermediate velocity $\mathbf{u}^*$. The pressure is then re-introduced by solving the expression

$$\frac{\mathbf{u}^{n+1} - \mathbf{u}^*}{\Delta t} = -\nabla p^{n+1}. \tag{2.40}$$

Co-efficient	1st Order	2nd Order	3rd Order
γ_0	1	3/2	11/6
α_0	1	2	3
α_1	0	-1/2	-3/2
α_2	0	0	1/3
β_0	1	2	3
β_1	0	-1	-3
β_2	0	0	1

Table 2.1: Weights for stiffly stable integration scheme. Karniadakis et al. (1991)

Summing equation (2.39) and (2.39) gives an approximation to the full momentum equation, although pressure is evaluated at the time-step $n+1$, whereas the diffusive terms are evaluated at time-step n.

By taking the divergence of (2.40) and applying the constraint that $(\nabla \cdot \mathbf{u}^{n+1}) = 0$ the equation

$$\nabla^2 p^{n+1} = \frac{\nabla \cdot \mathbf{u}^*}{\Delta t} \tag{2.41}$$

is formed. This elliptic equation for p can be solved numerically giving the required pressure to enforce the incompressibility condition. Once the new pressure is found it is relatively straightforward to evaluate equation (2.40) to find the new incompressible velocity $\mathbf{u}^{n+1}$.

High Order Splitting Scheme

The use of differing time values for $\mathbf{u}$ and p in equations (2.39) and (2.40) leads to a first order error in the accuracy of the time-stepping scheme. To overcome these accuracy limitations the multi-step scheme of Karniadakis et al. (1991) is used. In this technique mixed implicit/explicit time-stepping weights are employed with the advective terms being approximated explicitly and the pressure and diffusion terms being treated implicitly.

Using the differencing weights of table (2.1) the three step scheme involves solving the equations

$$\frac{\mathbf{u}^* - \sum_{i=0}^{J_i-1} \alpha_q \mathbf{u}^{n-q}}{\Delta t} = \sum_{q=0}^{J_e-1} \beta_q \left[(\mathbf{u} \cdot \nabla)\, \mathbf{u} \right]^{n-q}, \tag{2.42}$$

$$\frac{\mathbf{u}^{**} - \mathbf{u}^*}{\Delta t} = -\nabla p^{n+\frac{1}{2}}, \tag{2.43}$$

$$\frac{\gamma_0 \mathbf{u}^{n+1} - \mathbf{u}^{**}}{\Delta t} = \nu \nabla^2 \mathbf{u}^{n+1}, \tag{2.44}$$

where α_q and β_q are integration weights, and q represents the order of accuracy of the time-stepping scheme.

Solving equation (2.43) once again involves solution of the Poisson equation

$$\nabla^2 p^{n+\frac{1}{2}} = \nabla \cdot \left(\frac{\mathbf{u}^*}{\Delta t} \right) \tag{2.45}$$

but here the higher order boundary condition

$$\frac{\partial p^{n+1}}{\partial n} = -\nu \mathbf{n} \cdot (\nabla \times \nabla \times \mathbf{u})^{n+1} \quad \text{on} \quad \partial\Omega \tag{2.46}$$

is used to maintain accuracy at the boundaries. Since the value of $\mathbf{u}^{n+1}$ is unknown an explicit approximation is used;

$$\frac{\partial p^{n+1}}{\partial n} \approx \sum_{q=0}^{J_e - 1} -\beta_q \nu \mathbf{n} \cdot (\nabla \times \nabla \times \mathbf{u})^{n-q} \quad \text{on} \quad \partial\Omega. \tag{2.47}$$

The final step is to solve the diffusion equation

$$\left(\nabla^2 - \frac{\gamma_0}{\nu \Delta t} \right) \mathbf{u}^{n+1} = - \left(\frac{\mathbf{u}^{**}}{\nu \Delta t} \right) \tag{2.48}$$

with the appropriate Dirichlet boundary conditions on $\mathbf{u}$.

The first equation, (2.42), is trivial to solve using spectral elements since the spectral element method gives a diagonal mass matrix. The simple approach to solving this system used in the current work is to apply an iterative solver with Jacobi preconditioning. As equation (2.42) has a diagonal matrix when using the spectral element method, the diagonal Jacobi preconditioner turns out to be an exact solver, and the iterative solver will converge in one iteration. While it is possible to implement specialized code to deal with this case, the total time taken in this step is a negligible part of the total solution time and does not justify the extra coding complexity.

The second step, the solution of equation (2.45), is the most time consuming. The iteration count for the pressure Poisson equation is seen to be much higher than in the solution of the other matrix systems. A GMRES solver is used as the iterative solver in all of the current simulations.

The final step, (2.48), requires the solution of a series of Helmholtz equations; one equation per dimension. In practice these systems are seen to converge more rapidly than the pressure system at moderate and high Reynolds numbers.

2.5 Conclusion

The basic methods used in the course of this thesis have been outlined in chapter. Use of the finite element method, along with it's spectral element method variation, have been discussed

in terms of simulating the Navier-Stokes equations. Use of the penalty solver is discussed, including necessary modification to deal with simulations using cylindrical polar coordinates. As an alternate method of time discretisation, a high order multi-step projection technique is discussed as a way of solving the time-dependant Navier-Stokes equations.

In the next chapter some details of the implementation of these techniques are discussed, including implementation of these techniques on a distributed memory parallel architecture. An outline of the expected performance of the resulting code is also discussed.

Chapter 3

Program Structure

One of the disadvantages of finite and spectral element methods is the complex coding requirements; especially when compared to techniques such as the finite difference method. In addition to the complexity of these techniques, the use of parallel programming adds further complexity when compared with the more traditional serial programming model.

The approach taken in this thesis to overcome some of this complexity is to abstract the details of the finite/spectral element method into a C++ based object-oriented library. This library is also responsible for handling the bulk of the distributed programming.

3.1 Overview

Parallel programming offers substantial potential for increasing the available computing power for complex fluid dynamics problems. Presently, parallel computing seems to offer the only viable path for simulating large three-dimensional flows, even at moderate Reynolds numbers. In particular, 'Beowulf' style clusters of networked PC-style hardware are becoming increasing popular. This potential comes at a price, and that price is almost always complexity of the code required to utilize such computers.

The Multiple Instruction Multiple Data (MIMD) model of programming, typical of cluster programming, works at a relatively low level. In this thesis, the Messaging Passing Interface (MPI) library (Snir and Gropp (1998)), which implements this programming model, is used for all parallel communications. While MPI offers a powerful set of instructions, these operations are at a relatively low level, typically dealing with arrays of native data types which are explicitly passed between processors.

In this context, it is useful to first state a basic algorithm of the finite element method;

- Generate mesh
- Set initial conditions for the fields $\mathbf{u}$ and P.
- Build global matrix. For each element,
  - Build element matrix ek.
  - Assemble element matrix into global matrix K.
- Apply forward elimination of global system (required for direct solution), or apply preconditioning of global system (required for iterative solvers).
- For each iteration of the steady-state solver, or time-step of the time-dependant solver,
  - Build load vector by assembling element load vectors ef.
  - Perform back substitution of the global matrix for the direct solver or invoke the iterative solver.

While it possible to extend this description further to the level of structured programming constructs (FORTRAN code being common in many text books), the approach taken here is to operate on higher level objects referred to in the above description.

The following is a list of some of the key classes of objects operated on in the current code,

- *Mesh*.

  The *Mesh* class stores elements, and communicates global mesh information. Access to the members of the *Mesh*, which includes the *Element*s and *Boundary*s of the mesh, is allowed only by use of the appropriate iterators. Iterators allow access to the members of the class via the helper classes, *element_iterator* and *boundary_iterator*. This allows variations in the storage structure, especially between serial and parallel implementations, to be isolated. Code using this *Mesh* class need not know about the parallel storage used by the class.

  The current implementation requires that the parallel distribution of the mesh be fixed before iterative solution or time evolution begins. The *MeshTransporter* class is used to move elements between meshes. Along with an abstract *MeshDistribution* class this allows for the details of mesh distribution to be isolated. While the mesh is a parallel object, storing data on many processors, all heavy communication work is delegated to the MeshTransporter class. This removes much of the complexity from the mesh definition.

As well as storing elements, the mesh stores a collection of mesh boundaries. The structure of the mesh boundaries parallels that of the mesh itself, with boundaries consisting of a set of boundary elements distributed across the processors. A corresponding *BoundaryTransporter* is used to distribute the *ElementBoundary* objects.

- *GlobalFields*.

  The fields $\mathbf{u}$ and p are represented as *GlobalFields*, which are stored as continuous sections of the global data. The storage of the field continuously across processors simplifies many global operations, but also requires a different numbering system for the field data to that of the global mesh.

- *GlobalLayout*.

  The *GlobalLayout* stores the mapping between the mesh identifiers, the numbering used by the elements to number the nodes, and the values stored by the global fields. The use of different numbering systems for the mesh and global fields allows different processor topologies to be used without the need for renumbering the mesh, while still allowing global fields to have elements stored continuously over the processors.

  As well as storing the solution identifier of local nodes, the *GlobalLayout* class stores the solution identifier of nodes which are visible to the local processor (that is, are nodes of local elements), but are stored in the global field on a remote processor.

- Global system.

  The global matrix system $Ax = f$ is represented as high order objects.

  - *ElementMatrix* and *ElementVector*.

    These local quantities are defined on an element, and can be manipulated in terms of the master element without requiring knowledge of the global structure. To allow for sum factorisation (Karniadakis and Spencer, page 124), the three dimensional structure of the elements is maintained, so that the element vector is addressable as $ef(i, j, k)$ and the element matrix as $ek(i, j, k, r, s, t)$ where i, j, k and r, s, t represent x,y and z directional node counts respectively.

  - *GlobalMatrix* and *GlobalVector*.

    The global matrices and vectors are abstract classes that allows for the changing of the matrix storage scheme to suit the problem and execution environment. In particular, it is possible to change between serial and parallel implementations, or between dense and sparse storages.

The global matrix and vector provide an interface between the element level matrix and vector respectively. Element matrices and vectors are added to the global system during the assembly process, and the element matrix and vector can be extracted from their global counterpart by providing a reference to the required element.

The main operation that the global system provides is global multiplication, which is used extensively during the iterative solution process. For global matrices that provide direct solution, the global solver will operated on the global matrix data directly.

For the finite element method, it is convenient to store the matrix as either a banded storage matrix, or for the iterative solution, as a sparse matrix. This ability is provided by the PETSc numerical library (Balay et al. (2000)).

For the spectral element method, where the storage is more dense, the global matrix is implemented as a collection of element matrices stored on each processor. A hash table is then used to look up the element matrix corresponding to a given element.

- *EquationBuilder.*

  The equation builder is used to build the element level matrix and vector. Since a significant amount of time is spent building the global system (the load vector in particular, since the linear matrix terms are stored), a FORTRAN implementation of the build routines is used, as FORTRAN compilers were seen to be significantly better at optimizing tight matrix loops than the more abstracted C++ equivalent.

- *GlobalSolver.*

  The global solver works with the global matrix and global vector to solve the global linear system. The implementation is based on the PETSc library (Balay et al. (2000)).

  While the PETSc library provides a flexible array class of it's own, the fully sparse structure used by PETSc is relatively inefficient for the spectral element method, where there is a significant amount of structure in the element system. PETSc does, however, allow for the use of shell matrices, passing off the matrix multiplication work to user code. In this work, a global shell matrix class is defined which uses BLAS (Dongarra et al. (1988)) library routines to multiply the element matrices. The element matrix size is typically of order 100×100 in two dimensions and 1000×1000 in three dimensions, so that the speed advantage of the optimized BLAS routines over an unstructured sparse matrix multiply are significant.

3.2 Matrix Solution

The solution of the matrix system

$$Kx = f \tag{3.1}$$

for a matrix K and vectors x and f is typically the most time consuming step of the finite and spectral element method solution process. Different numerical techniques are employed to solve this system depending on the nature and size of the matrix K.

3.2.1 Direct Solvers

When using the penalty method of section 2.4.1, multiplication of the pressure term by the penalty parameter λ leads to a poorly conditioned system, making the use of iterative solvers prohibitively slow. In this case the use of direct solvers (Gaussian elimination) is the only viable solution strategy.

While the global system (3.1) is sparse, particularly when using a low order finite element method, the effect of forward elimination is to fill-in a band of the matrix. The bandwidth of this fill-in is determined by the maximum difference in node numbers between nodes which share a common element.

The technique used for direct solution of the global system in this thesis is to use the banded dense solver of the LAPACK linear algebra library (Anderson et al. (1999)). For large problems this involves a large amount of memory. However, when the memory is available the global system is solved quickly compared to iterative solvers.

3.2.2 Iterative solvers

For three-dimensional and high accuracy calculations, the use of direct solvers is prohibitively expensive. In these situations, the use of iterative solvers is necessary.

In this work PETSc's GMRES solver is used. When solving for a finite element system, it is possible to use incomplete LU (ILU) decomposition for the preconditioner. When using the spectral element method, to allow for the storage as structured element matrices, only diagonal (Jacobi) preconditioning has been used.

Unfortunately, the use of diagonal preconditioning leads to relatively high iteration counts when solving the pressure Poisson equation. In contrast, the Helmholtz equations of (2.42) are seen to converge relatively quickly; usually an order of magnitude faster than the pressure system.

While the use of the GMRES with Jacobi preconditioning has produced satisfactory results, more efficient preconditioning is clearly one area where the current work could improve

in terms of efficiency.

3.2.3 Static Condensation

Static condensation involves the separation of the solution variables into those nodes that are connected to multiple elements (the mortar nodes) and those that are on the interior of the elements. Full details of this technique are given in Karniadakis and Sherwin (1999).

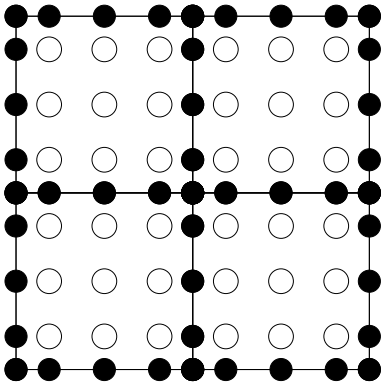

Figure 3.1: Mesh structure for static condensation. Open circle are interior nodes, closed circles represent mortar nodes.

The approach is to initially factorize the element systems into internal and mortar nodes, so that a global system consisting only of mortar nodes can be solved. Mortar nodes, the closed nodes shown in Figure 3.1, are those that are in contact with more than one element or boundary. Conversely, the interior nodes interact only with nodes of the same element. In this example mesh (of rather low resolution) the mortar nodes are 45 of the 81 nodes. As the order of the mesh is increased the relative number of interior nodes increases.

Factorisation by static condensation need only be done once when the matrix system is constant, as is usually the case. Once the global system has been solved, back-substitution can be performed to evaluate the internal values. This factorisation can be done at an element matrix level, and is performed using optimized LAPACK routines.

The advantages of this technique are that the global system size is reduced, so that the work per iteration is less. Smaller systems also typically take fewer iterations to solve. Karniadakis and Sherwin also suggest that the condition number of the reduced system is improved, and hence static condensation also acts as a form of preconditioning.

To test the effectiveness of the static condensation technique, the startup flow of flow past a two dimensional cylinder is simulated for 100 time-steps using a 64 element seventh

order mesh. The flow equations use the multi-step projection technique of section 2.4.2 with order 1 coefficients for the temporal discretisation. The effect of using Jacobi (diagonal) preconditioning on the factored system is also compared. The wall time compares the physical time elapsed while solving the time-stepping part of the simulations. The time involved in the initial factorisation is not included as this one-off cost is relatively small for simulations involving many time-steps.

Preconditioned (diagonal)	Static Condensation	Iterations	time/iter. ($s \times 10^{-3}$)	Wall time (s)
No	No	88332	37.1	3280
Yes	No	61330	37.4	2293
No	Yes	27387	10.2	279
Yes	Yes	13983	11.4	159

Table 3.1: Effect of static condensation and preconditioning on user time

Table (3.1) gives an indication of the effectiveness of using static condensation. For this moderate sized two-dimensional problem, the elapsed wall time is reduced by more than a factor of 10, with savings from reduced work per iterations and reduced iteration counts contributing similar amounts. The number of degrees of freedom in the global system is reduced from 3248 to 944 for this particular mesh. The differences seen in the norms of velocity and pressure at the end of the run, as well as values at several points within the flow, are within the tolerance specified in the iterative solver.

3.3 Parallel Partitioning

A determining factor in the efficiency of parallel programs is the total amount of communication required between processors. In the finite element and spectral element methods, the main factor affecting the required communication is the parallel layout of the elements across processors. Ideally, the distribution of elements gives an equal workload (or equal number of elements) for each processor while minimizing the number nodes that are required on multiple processors, which happens when a node is a nodal point of elements that reside on different processors.

To attempt to minimize the amount of communication between processors, the multilevel k-way graph partitioner algorithm of Karypis and Kumar (1997) has been used, via Karypis' ParMetis partitioning library. While this method is particularly good at reducing the number of inter-processor communications, it unfortunately does not produce a balanced work pattern

for the low number of elements usually considered in spectral elements. Since the number of elements per processor can reasonably be as low as 10 when using three-dimensional spectral elements, it is common for ParMetis to return parallel layouts that are imbalanced by up to 40%.

An advantage of the spectral element method, however, is that solution for each element requires a relatively large amount of work, and hence tends to be less sensitive to having many inter-processor communications. Because of this it has proved feasible to use an extremely simple partitioner, simply distributing the elements based on their element number. This number is generated with the mesh, and tends to be continuous over blocks. The two opposing factors of load-balancing and parallel communication mean that the parallel results from the two partitioning methods are very similar and either can be used relatively successfully.

3.4 Parallel Performance

In this section the parallel performance of the numerical code is examined. To test this performance a series of simulations are performed on varying numbers of processors.

The test machine, 'avalon', consists of 140 Linux machines with 533Mhz 21164 alpha CPUs. The machines are connected with full-duplex 100Mbps fast-ethernet networking. While the parallel code has been tested on a number of MPI implementations including MPICH, LAM and a Compaq proprietary MPI implementation, the following results refer only to the LAM implementation. Preliminary results with MPICH show very similar performance to LAM for moderate to large problem sizes. The main reason for choosing LAM over MPICH in the current work is a more convenient execution environment.

The test problem considered is startup flow of a driven cavity. An initially stationary fluid in a unit box has a boundary condition of $\mathbf{u} = (1, 0, 0)$ applied at $t = 0$ to the upper lid. The flow, with a Reynolds number of 100, is then integrated forward in time for 100 steps with a time-step of 0.01. The second order multi-step scheme of section (2.4.2) is used and a constant element order of nine is used for all simulations.

To measure the efficiency of the simulation the wall time per iteration is measured. The initial set up time, covering such one-off operations as reading the mesh, building the global matrix and performing static condensation are not included in this measure since this time is amortized as the number of time-steps is increased. The data fields $(\mathbf{u}, p)$ are written out at the beginning and end of the run, since the simulations of later chapters save data fields at an interval similar to this.

3.4.1 Scaled Speedup

In the first experiment, the number of elements per processor is varied to use a regular mesh of $(N.nprocs) \times N$ element, where N is constant and *nprocs* represents the number of processors used. The wall time per iteration is then used for comparison. For a perfectly efficient parallel program the total time taken per iterations should be constant. As the number of degrees of freedom increases the number of iterations performed per time-step increases and this increases the relative amount of time spent in the matrix multiplication stage of the computation compared to other, typically less parallel steps such as writing out results and synchronization between time-steps. This type of speedup gives a measure of the performance results achieved when parallel computing is used to run bigger simulations in similar amounts of time.

Figure 3.2 shows the performance of the parallel code measured on a scaled problem size. The three cases considered are a two-dimensional box, with 100 ninth-order elements per processor. In three-dimensions a box with 8 ninth-order elements per processor is used for lower numbers of processors, which 4 elements per processors are used for the larger problems.

The first observations to be made is that for all of the tested problems the scaling is close to the ideal linear speedup. This is more impressive given that the testing is done on 100Mbps fast-ethernet, which exhibits high latency and low bandwidth, especially when compared with other more expensive parallel communication technologies.

The three dimensional problems scales significantly better than the corresponding two dimensional problem. In three dimensions the relative number of nodes occupying multiple processors is actually higher than the two dimensional problem, but this is more than offset by the increase in total computation time. For the high order elements used, the cost of an individual element multiplication increases by an order of approximately 100, and this increase in work per iterations reduces the relative effect of communication and other serial operations.

The increasing problem size accounts for the greater than parallel speedup for low number of processors. As the problem size is increased in proportion with the number of processors the total workload is increased by a larger factor since the iteration count is also increased. This extra work tends to reduce the relative time taken performing one-off serial operations, such as storing results and serial book-keeping operations.

The larger three-dimensional problem, used with fewer processors, shows a relatively rapid drop in speedup for eight processors, although the speedup is still more than eight times that achieved on one processor. A possible reason for this is that as the problem size increases, the amount of memory per processor increases slightly, and it's likely that the core size becomes

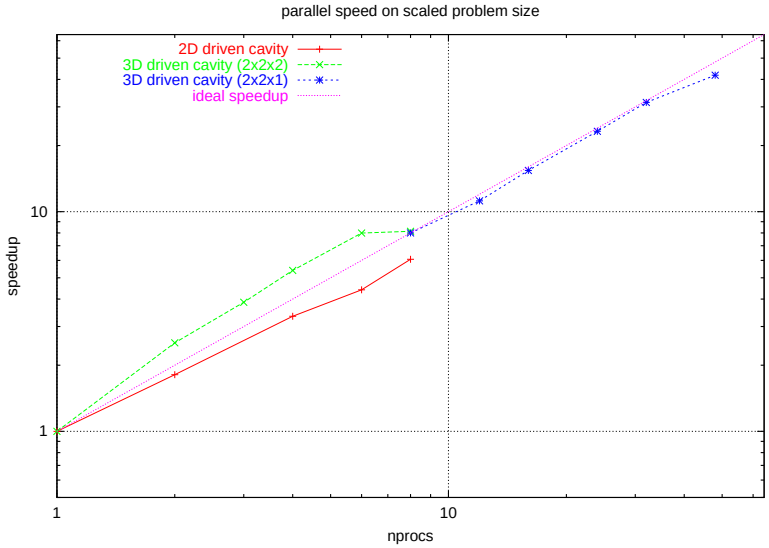

num procs	rank	N	time/iter. (s^{-3})	speed up
1	2	10×10	32.19	1.00
2	2	20×10	35.62	1.81
4	2	20×20	38.57	3.34
6	2	30×20	43.81	4.41
8	2	40×20	42.44	6.07
1	3	$2 \times 2 \times 2$	182.1	1.00
2	3	$4 \times 2 \times 2$	143.7	2.53
3	3	$4 \times 3 \times 2$	141.2	3.87
4	3	$4 \times 4 \times 2$	134.8	5.40
6	3	$4 \times 4 \times 3$	136.7	7.99
8	3	$4 \times 4 \times 4$	178.9	8.14
8	3	$4 \times 4 \times 2$	78.30	8.00
12	3	$4 \times 4 \times 3$	84.03	11.2
16	3	$4 \times 4 \times 4$	81.26	15.4
24	3	$6 \times 4 \times 4$	80.87	23.2
32	3	$8 \times 4 \times 4$	79.93	31.4
48	3	$8 \times 6 \times 4$	90.01	41.8

Figure 3.2: Parallel performance of shear flow problem. Scaled problem size

slightly larger than the available memory.

In the smaller three-dimensional case, used with up to 48 processors, the speedup is near linear up to 32 processors, and starts to drop off above this. Above 32 processors, the workload of four elements per processors starts to become overwhelmed by the communication time. In the high resolution cases considered in later chapters, the number of elements used in 64 processor simulations was between 10 and 35 elements per processor, and based on the above benchmarking, it is expected that the communication overhead of these simulations is quite low.

3.4.2 Fixed Problem Size Speedup

In the second experiment, the number of elements is fixed as the number of processors is increased. For an increasing number of processors this results in progressively less work to be done by each processor. This type of measure gives an indication of the type of speed up when using parallel computing to perform the same task in a shorter amount of time.

Figure 3.4.2 shows the results of testing the parallel code on two fixed problems; one two-dimensional and the other three-dimensional. The two-dimensional simulation occurs on a 20×20 ninth-order element box consisting of around $33,000$ nodes, whereas the three dimensional simulation on a $4 \times 4 \times 2$ box mesh has just over $26,000$ nodes. The three-dimensional problem requires more total work per iterations however, since an order p element multiplication is $O(p^4)$ for $(p+1)^2$ nodes in two dimensions and $O(p^6)$ for $(p+1)^3$ nodes in three dimensions, giving an increase in complexity of $O(p)$, or approximately 10 times more work for the current meshes.

The results of the fixed problem size scaling is encouraging. For what is a moderate problem size speedups of order six are given on eight processors. While some overhead is incurred, the total speedup more than justifies the use of parallel simulation.

The two testing methods employed represent two extremes; the first technique of varying the number of elements with increasing parallelization tends to provide an optimistic measure of parallel performance while using a fixed number of elements tends to give an overly pessimistic view of the parallel performance. Both techniques can be useful if viewed as giving an upper and lower bound on the speedups that are likely to be achieved in practice. Using either measure it is clear that the parallel spectral element method is capable of significant speedups with high-latency relatively low bandwidth parallel technology.

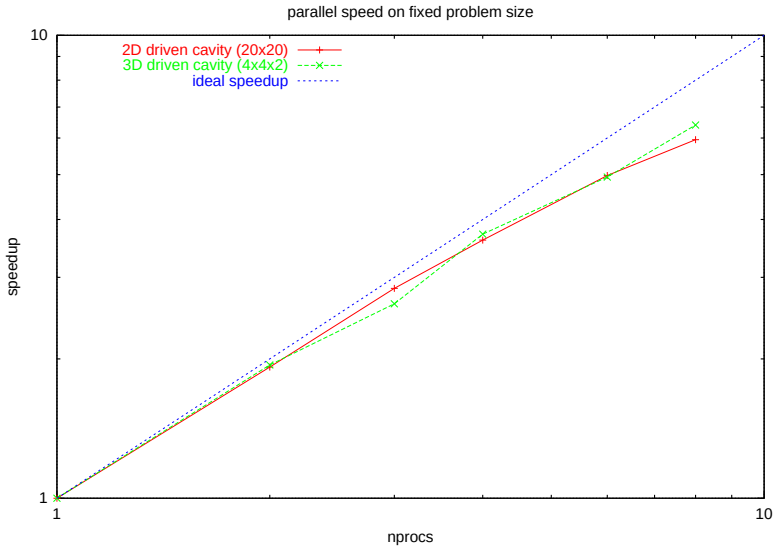

num procs	rank	N	time/iter. (s^{-3})	speed up
1	2	20×20	121.9	1.00
2	2	20×20	63.5	1.92
3	2	20×20	42.9	2.84
4	2	20×20	33.7	3.61
6	2	20×20	24.5	4.98
8	2	20×20	20.5	5.95
1	3	$4 \times 4 \times 2$	520.2	1.00
2	3	$4 \times 4 \times 2$	267.6	1.94
3	3	$4 \times 4 \times 2$	197.8	2.63
4	3	$4 \times 4 \times 2$	139.9	3.72
6	3	$4 \times 4 \times 2$	105.3	4.94
8	3	$4 \times 4 \times 2$	81.26	6.40

Figure 3.3: Parallel performance of shear flow problem. Fixed problem size

3.5 Conclusion

This chapter outlines an object-oriented approach to implementing a parallel finite/spectral element method in C++. Through a careful choice of key classes it has been possible to abstract many of the more complicated details of the parallel implementation to provide a powerful set of classes for solving PDE's associated with these numerical methods.

Simple benchmarks show that for large scale problems, such as those to be tackled in later chapters, the current implementation provides significant speedups, even on relatively low end parallel hardware.

In the following chapters these methods are applied to two problems. The first problem examined is vortex breakdown flow in a confined cylinder, where both the steady and unsteady flows are examined. Secondly, shedding flow past a sphere is simulated, and interaction of multiple sphere wakes is studied.

Chapter 4

Vortex Breakdown

Vortex breakdown has been defined as the sudden transition of a flow from a concentrated axial core to a relatively large region of retarded flow. A divergence of flow away from the core is typically observed, and such events are often associated with a change from laminar to turbulent flow.

Vortex breakdown was first observed in an aeronautical context by Peckham and Atkinson (1957) who observed vortex breakdown over delta wings at high angles of attack. The strong vortex cores produced by such wings were seen to suddenly form turbulent, asymmetric regions.

Vortex breakdown is thought to be of importance in swirling flows through nozzles and diffusers, in tornado models, and as a possible mechanism for describe transition to turbulence (Escudier (1988)).

4.1 Flow Features

The first observed occurrence of vortex breakdown, breakdown over a delta wing, is an unstable, three dimensional and possible turbulent phenomenon. A concentrated core of high vorticity is seen to suddenly expand and become turbulent. A visualization of this delta wing breakdown, by Werlé (1960), is shown in Figure 4.1.

As a way of addressing the complexity of the delta wing flow, several experiments with better defined characteristics have been devised. The most common experimental apparatus for considering breakdown has been the diverging duct apparatus of Figure 4.2. Here, a rotating flow field is pumped into a diverging tube apparatus. This apparatus was first examined by Harvey (1962), and has since been considered by Kirkpatrick (1964), Sarpkaya (1971a),

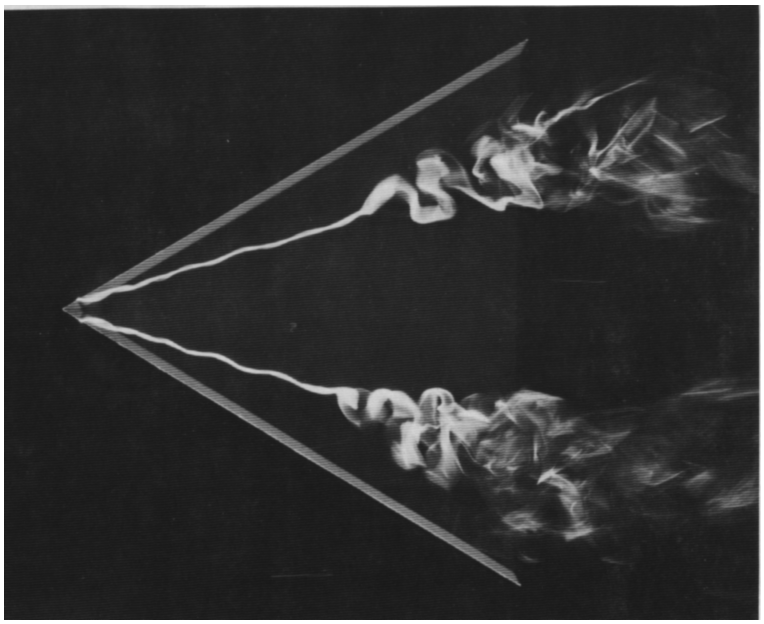

Figure 4.1: Vortex breakdown over a delta wing. Visualization by Werlé (1960), from Dyke (1982)

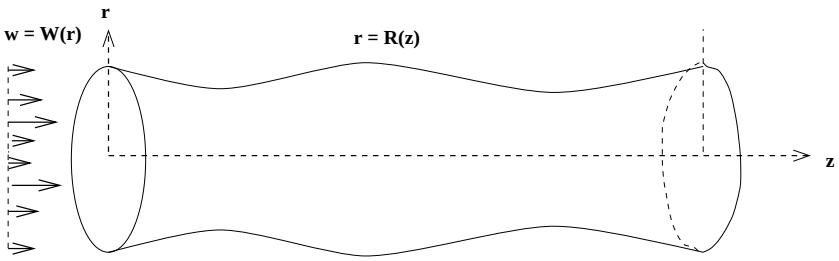

Figure 4.2: Swirling pipe apparatus

Faler and Leibovich (1977), Escudier and Zehnder (1982). In all of these experiments, slightly differing pipe profiles, $R(z)$, were considered.

The results of Sarpkaya (1971b) offer some of the most complete experimental results for diverging pipe vortex breakdown. From these results, it is known that breakdown in a duct progresses from an initially axisymmetric swirl to an eventual 'bubble' type breakdown. It is seen that the initial core forms a so called spiral breakdown, with a turbulent region forming behind the breakdown. With increasing input swirl, the spiral vortex is seen to gradually become more symmetric in character, eventually forming the so-called bubble breakdown. The rear of this region is not clearly defined and typically involves turbulent flow behind the bubble.

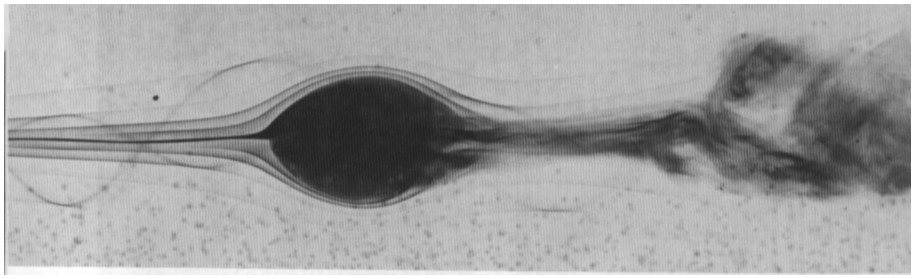

Figure 4.3: Vortex breakdown in divergent pipe flow. Visualization by Sarpkaya (1971b), from Dyke (1982)

Escudier (1984) considered flow in the confined cylinder apparatus of Figure 4.4. This configuration has the advantage of offering a well defined problem, with only two free parameters; the Reynolds number and aspect ratio. Escudier examined the $(Re, H/R)$ parameter space to produce a so called stability diagram indicating the number of breakdown bubbles present over a range of problem parameters. An indication was also given of the parameter range for the problem to remain time independent. In contrast to the previously studied flows, increases of input speed, in this case facilitated by an increase in driving speed, can return the flow to a stable configuration in which no breakdown bubbles are present.

Bar-Yoseph et al. (1992) have demonstrated that vortex breakdown can occur between two rotating spheres. This is perhaps expected, since with relatively large sphere diameters compared to the inter-sphere gap, this apparatus produces a flow pattern that is locally similar in structure to the swirling cavity system. It was seen that boundary layers formed on the inner sphere meet and form a strong vortex core in a similar way to the cylinder apparatus.

Mory and Yurchenko (1993) observed vortex breakdown in a rotating tank, with suction

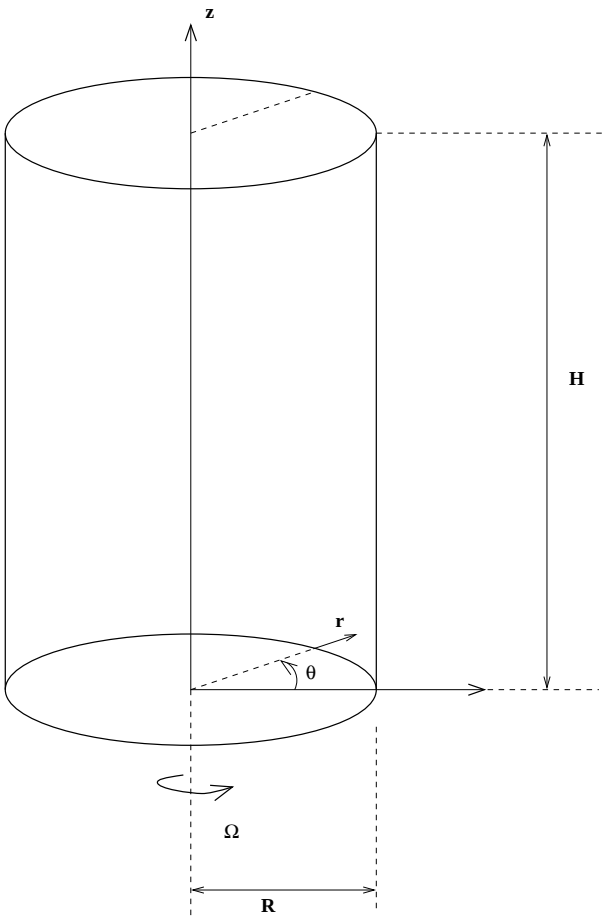

Figure 4.4: Confined cylinder apparatus, base rotation rate of Ω.

applied through a tube on the bottom of the axis of rotation. The suggested form of the boundary layers was similar to that of the confined cylinder experiment, although the rotation rate and vortex axial velocity could be varied independently.

4.2 Numerical Studies

Several numerical studies have been made of vortex breakdown. Earlier work often suffered from a lack of numerical resolution, and as more suitable computers have become available it has become obvious that vortex breakdown simulations are generally quite sensitive to numerical resolution.

Grabowski and Berger (1976) performed an early numerical investigation of vortex breakdown in a divergent tube. A lack of resolution means that the results gave at best a qualitative picture of vortex breakdown.

Lopez (1990) performed an extensive numerical comparison with the confined cylinder experiment of Escudier (1984). Good agreement was seen between the two sets of results; in particular the so called stability diagram of Escudier was reproduced numerically. For the two parameter space of Re and aspect ratio H/R, the number of observed breakdown bubbles was seen to coincide.

Some doubt has been cast on the numerical accuracy of the Lopez & Brown's work in Graham et al. (1995), especially in light of the use of unstretched grids near the bottom boundary layer. Vortex breakdown in the confined apparatus is caused by the bottom boundary producing a locally strong central core of vorticity, suggesting that a lack of boundary layer resolution could be a significant problem. However, the interior flow is largely inviscid, suggesting that the conclusions draw from this paper are not necessarily invalidated. The most likely result of under-resolving the lower boundary layer would be a reduction in the effective Reynolds number, causing vortex breakdown to require slightly higher numerical Reynolds numbers.

Daube (1991) analyzed the flow in a confined cylinder of Figure 4.4 with both fixed and stress free boundary conditions on the top surface. The fixed boundary flow showed good agreement with the experimental work of Escudier. The stress free boundary flow was seen to also undergo vortex breakdown, although no mechanism for vortex breakdown was put forward.

Both Spall et al. (1987) and Breuer and Hänel (1993) examined the breakdown numerically in three dimensions for flow through a rectangular duct. These flows exhibited both bubble and axisymmetric type breakdowns.

Beran (1994) performed a series of axisymmetric, inviscid calculations on the swirling

pipe apparatus of Figure 4.2, and demonstrated that the final state of breakdown is, in some cases, dependent on the way the the vortex is initially applied. In particular, a comparison between instantaneous application of the vortex with a ramping process was performed.

4.3 Breakdown Mechanisms

Hall (1972) gave the first comprehensive review of possible mechanisms for vortex breakdown, providing three groupings of the theory for vortex breakdown. These classifications will be considered, and expanded on in the light of recent literature.

The three groupings of Hall, as well as three additional proposals can be summarized as

1. Vortex Breakdown is analogous to boundary layer separation. These are usually examined by use of the Quasi-Cylindrical equations. Gartshore (1962), Hall (1967), Bossel (1969), Bossel (1971).

2. Vortex breakdown is a consequence hydrodynamic instability. Ludweig (1962), Ludweig (1970), Lessen et al. (1974).

3. Vortex Breakdown depends on transition from a supercritical to a sub-critical state. Squire (1960), Benjamin (1962), Benjamin (1967), Bossel (1969).

4. A grouping, closely related to the previous criteria, is based on the idea of a trapped wave model. Leibovich (1970), Leibovich and Randall (1973), Randall and Leibovich (1973), Bilanin and Widnall (1973), Sarpkaya (1971b), Sarpkaya (1974), Tsai and Widnall (1980), Darmofal and Murman (1994).

5. Spall et al. (1987) have suggested that existing criteria are equivalent to a local Rossby number criteria.

6. Brown and Lopez (1990) have proposed that vortex breakdown can be explained in terms of a feedback mechanism generating negative vorticity.

Clearly, many of these categories are related and several of the criteria could be said to fit into more than one category. In particular it is likely that criteria 1, 3 and 4 are equivalent.

4.3.1 Flow Configuration

All of the existing theories have been applied to flow through a duct with swirling input, as indicated in Figure 4.2.

This problem can be stated as follows.

Consider a flow in cylindrical polar coordinates. The velocities can be written as (u, v, w) for coordinates (r, θ, z). Initially, the flow consists of a vortex, with profile to be specified, with a typical velocity W in the z direction and a swirl velocity Ω. At some upstream point $z = z_0$, the axial velocity is specified as $w = W(r)$. The geometry of the pipe is specified by defining the outer boundary as $r = R(z)$.

4.3.2 Quasi-Cylindrical Approximation

Upstream of the breakdown point, the flow is seen to vary only gradually in the axial direction. By assuming that the flow is laminar, incompressible, and axisymmetric, as well as neglecting derivatives in the axial (z) direction, we have the so-called quasi-cylindrical equations of Hall (1967).

$$\begin{aligned}
\frac{v^2}{r} &= \frac{1}{\rho}\frac{\partial p}{\partial r}, \\
u\frac{\partial v}{\partial r} + \frac{uv}{r} + w\frac{\partial v}{\partial z} &= \nu\left(\frac{\partial^2 v}{\partial r^2} + \frac{1}{r}\frac{\partial v}{\partial r} - \frac{v}{r^2}\right), \\
u\frac{\partial w}{\partial r} + w\frac{\partial w}{\partial z} &= -\frac{1}{\rho}\frac{\partial p}{\partial z} + \nu\left(\frac{\partial^2 w}{\partial r^2} + \frac{1}{r}\frac{\partial w}{\partial r}\right), \\
\frac{\partial u}{\partial r} + \frac{u}{r} + \frac{\partial w}{\partial z} &= 0.
\end{aligned}$$

The boundary conditions come from symmetry at the axis; $u = v = \partial w/\partial r = 0$ at $r = 0$, a prescribed pressure at the outer boundary, say $p = P(z)$ at $r = R(z)$, and an inflow condition giving $v = v_0(r)$ and $w = w_0(r)$ at $z = z_0$.

Since these equations are parabolic, the solution can be solved for increasing z values. increasing z. Breakdown is then considered to occur when the solutions fail to converge.

The solution of these equations can predict a breakdown Reynolds' number and position which is qualitatively correct. Hall (1967) evaluated the quasi-cylindrical equations for a configuration comparable to that of Kirkpatrick (1964), and attempted to make quantitative comparisons. Due to the limited resolution, and variations in model parameters, it was considered that the difference in position of one and a half bobble diameters was not unreasonable.

The overall characteristics of the vortex breakdown that seem to be in reasonable agreement are

- larger positive pressure gradients (facilitated by duct divergence in these experiments) induce vortex breakdown more quickly.
- the vortex breakdown behavior is largely independent of Reynolds number.

- increase in swirl parameter are seen to move the breakdown point upstream.

Unfortunately, the quasi-cylindrical equations offer no model of the flow once breakdown has occurred. Neither does the model necessarily give a physical mechanism for the breakdown, but rather a means of predicting the occurrence.

It should be noted that Hall (1972) claimed that the criticality of the flow (as described by Squire (1960) and Benjamin (1962)) drops from a supercritical to a sub-critical state. This compares favorably with the critical state model (mechanism 3) to be examined later, as well as remaining consistent with the analogy to boundary layer breakdown. This analogy suggests that once information can travel back upstream the boundary layer equations will break down.

This model has been extended by Berger and Eriebacher (1995) who modified the equations to allow for diffusion in the radial direction. The equations show similar behavior to the quasi-cylindrical equations, and they have demonstrated that change in problem parameters cause the correct qualitative changes in breakdown behavior. In particular, it is once again observed that increase in input swirl leads to the movement of the breakdown bubble upstream. Again, no mechanisms behind the behavior are offered.

4.3.3 Spiral Instability

Ludweig (1962) proposed that vortex breakdown is a result of a spiral instability in the flow. It is proposed that when the criteria

$$\left(\frac{5}{3} - \frac{r}{v}\frac{\partial v}{\partial r}\right)\left(\frac{r}{v}\frac{\partial w}{\partial r}\right)^2 - \left(1 - \frac{r}{v}\frac{\partial v}{\partial r}\right)\left[1 - \left(\frac{r}{v}\frac{\partial v}{\partial v}\partial r\right)^2\right] > 0 \tag{4.1}$$

is satisfied, it is possible for the flow to become unstable to asymmetric perturbations.

Mager (1972) considered the quasi-cylindrical equation, showing that two branches of the solution existed. It was suggested that breakdown was a result of asymmetric instabilities, leading to a crossover between the two states.

Spall (1993) examined the linear stability of solutions to the quasi-cylindrical equations (4.1) with a modified model to allow for non-parallel terms in the flow equations. With the addition of these non-parallel terms viscous and inviscid instabilities were observed, although it was suggested that a fully non-parallel formulation is required to validate these results.

Tsitverblit (1993) performed a number of numerical calculations on the confined cylinder geometry. By the use of a continuation method, the process of bifurcation was ruled out as a cause of axisymmetric breakdown, but that the transition to an unsteady flow was the result of a Hopf bifurcation.

4.3.4 Critical State Transition

Following Hall (1972), the equations for axisymmetric, inviscid flow, in stream function form can be written as

$$u = -\frac{1}{r}\frac{\partial \psi}{\partial z} \tag{4.2}$$

$$w = \frac{1}{r}\frac{\partial \psi}{\partial r} \tag{4.3}$$

$$\mathcal{H} = p + \frac{1}{2}\rho(u^2 + v^2 + w^2) \tag{4.4}$$

$$\frac{\partial^2 \psi}{\partial r^2} - \frac{1}{r}\frac{\partial \psi}{\partial r} + \frac{\partial^2 \psi}{\partial z^2} = -\Gamma\frac{d\Gamma}{d\psi} + \frac{r^2}{\rho}\frac{d\mathcal{H}}{d\psi} \tag{4.5}$$

with the total circulation $\Gamma = rv$ and the total pressure $\mathcal{H}$ being functions of ψ and position only.

The assumption of inviscid flow seems reasonable, given the experimental observations indicating the relatively minor role of Reynolds number in the breakdown behavior. The assumption of axisymmetric flow is not as easily justified for cases where spiral breakdown is first observed. For flows where bubble type breakdown is the first type of breakdown to appear, such as the confined cylinder flow, the assumption seems more reasonable.

Following the notation of Benjamin (1962), the critical state theory can be summarized as follows. Consider a stationary axisymmetric perturbation of a quasi-cylindrical flow $\Psi(r, z)$ such that the stream function ψ can be written as

$$\psi(r, z) = \Psi(r, z) + \epsilon F(r, z) e^{\gamma z} \tag{4.6}$$

where $F(r, z)$ is a quasi-cylindrical function such that

$$\frac{\partial F}{\partial z} \ll \frac{F}{r} \tag{4.7}$$

$$\epsilon \ll 1 \tag{4.8}$$

Clearly, the following procedure can be generalized for a number of F's, giving a general perturbation solution for ψ.

Substituting the expression (4.6) into equation (4.5) and eliminating terms of $O(\epsilon^2)$ and smaller gives the following equation for the perturbation coefficient F

$$\frac{\partial^2 F}{\partial r^2} - \frac{1}{r}\frac{\partial F}{\partial r} + \left[\gamma^2 - \frac{1}{W}\frac{\partial^2 W}{\partial r^2} + \frac{1}{rW}\frac{\partial W}{\partial r} + \frac{1}{r^3 w^2}\frac{\partial K^2}{\partial r}\right] F = 0 \tag{4.9}$$

where $w = W$ and $\Gamma = K$ from the basic flow $\Psi(r, z)$. Boundary conditions require $F(r = 0) = F(r = R) = 0$.

This system is a Sturm-Liouville system for F, and it can therefore be shown that if the smallest eigenvalue γ_0^2 is negative then the basic flow is sub-critical, $\gamma_0^2 > 0$ implies

supercritical flow, and $\gamma_0 = 0$ is the critical case. The wavelength of this disturbance is $2\pi/(-\gamma_0^2)^{1/2}$. From equation (4.6), sub-critical flow can be interpreted as a flow that allows the transmission of information upstream, as the perturbation will be an oscillating one. Supercritical flows only allow the passing of information downstream.

Setting γ equal to zero in equation (4.9) gives a condition for critical flow. At a given axial position z, the criticality of the flow can be tested by applying the boundary conditions $F_c = 0$ and $\partial F_c/\partial r = constant$ at $r = 0$ and $r = R(z)$ respectively. The criticality condition then becomes

$$\frac{\partial^2 F_c}{\partial r^2} - \frac{1}{r}\frac{\partial F_c}{\partial r} + \left[-\frac{1}{W}\frac{\partial^2 W}{\partial r^2} + \frac{1}{rW}\frac{\partial W}{\partial r} + \frac{1}{r^3 W^2}\frac{K^2}{\partial r}\right] F_c = 0 \tag{4.10}$$

Squire (1960) considered the characteristics of a wave with infinite wavelength. The idea behind this model is that if waves of finite wavelength could exist, they will move upstream and cause vortex breakdown. Benjamin (1962) pointed out that the group velocity of infinite wavelength waves is downstream, and hence could not influence the flow upstream.

Benjamin extended the idea of critical state by using an analogy with hydraulic jumps. He suggested that vortex breakdown could be a jump between two solutions, one supercritical, the other sub-critical.

One problem with this model, as pointed out by the author, is the fact that the sub-critical flow has a greater momentum flow (or flow force), defined as $2\pi \int_0^R (p + \rho w^2) r\, dr$. It was postulated that the change in momentum flow could be justified by the existence of infinitesimal standing waves. It is argued that these standing waves could be what we refer to as vortex breakdown.

Benjamin's explanation, however, relies on the fact that these waves will be small, which is inconsistent with observed vortex breakdown. To maintain a large breakdown bubble, Benjamin suggested that a turbulent transition may be present. This seems inconsistent with the results in the confined cylinder experiment, where the transition is a laminar one.

Furthermore, the prediction of a jump, similar to a hydraulic jump, between conjugate states also seems inconsistent with observations in the confined swirling flow, where a continuous transition from breakdown to non-breakdown region is observed.

Bossel (1969) took the approximation further, requiring that upstream from the vortex breakdown, the flow be in a state of solid rotation. The equations thus simplify to

$$\frac{\partial^2 \psi}{\partial r^2} - \frac{1}{r}\frac{\partial \psi}{\partial r} + \frac{\partial^2 \psi}{\partial z^2} = a^2 \psi + \frac{b r^2}{\rho} \tag{4.11}$$

for constants a and b. A downfall of this model is the need to specify the outflow stream-function distributions $\psi(r)$. Furthermore, while simulations could be shown to form bubble

shaped regions, this was only possible by specifying a bubble type form for the outflow boundary.

Since the equation is clearly elliptic, it is hardly surprising that a bubble shaped outflow boundary condition would form some sort of bubble within the flow region. Because of the number approximations in the model it is not clear that enough useful information remains in the model to draw firm conclusions.

4.3.5 Trapped Wave Model

The wave model of vortex breakdown builds on the idea of the existence of supercritical and sub-critical states. This theory aims to demonstrate the ability of slightly sub-critical flows to maintain standing waves, that these waves will be trapped at a point, and that this mechanism is equivalent to the vortex breakdown phenomenon.

Leibovich (1970) considered perturbations of a base flow of the form $\psi_1 = \epsilon\phi(r)A(z,t)$, where ϵ is again a small constant. For motion confined to a tube, the perturbation equation for A satisfies the Korteweg-de Vries (KdV) equation

$$A_t + c_o A_z = \epsilon c_1 A A_z + k^2 c_2 A_{zzz} \tag{4.12}$$

for a small ϵ, a wavenumber k and constants c_i. These equations (Korteweg & de Vries, 1895) allow a wave solution of the form

$$A = a\text{sech}^2\left[\frac{1}{2}\left(\frac{c_1 a}{3c_2}\right)^{\frac{1}{2}}\left(X + \frac{1}{3}ac_1\epsilon t\right)\right] \tag{4.13}$$

for a constant a and X represents a scaled distance downstream.

By applying this solution to a flow with constant upstream velocity, and a Burger's vortex distribution of azimuthal velocity, it was demonstrated that standing waves can exist in slightly sub-critical flows. By solving for the dominant eigenvalue for a given upstream swirl angle, the corresponding eigenfunction was evaluated.

It was shown that the form of the solutions were in good qualitative agreement with observations of breakdown in pipes, which is known to have a comparable upstream velocity distribution.

The acknowledged weakness in this argument is the requirement that the waves be of 'small' amplitude, whereas the calculated waves exhibit differences of $O(1)$. It is also known that the solution of the KdV equations are seen to change drastically with the addition of diffusive effects, which are neglected in this study.

Benjamin (1967) also showed that the KdV approximation fails as the diameter of the

tube is increased to infinity. Leibovich proposed the alternative set of equations

$$A_t + c_0 A_z = \epsilon c_1 A Z_z + \frac{k^2 c_3}{2\log(1/k)} \frac{\partial^3}{\partial z^3} \int_{-\infty}^{\infty} \frac{A(\xi,t)\, d\xi}{((z-\xi)^2 + k^2)^{\frac{1}{2}}} \tag{4.14}$$

which in the limit of $k \to 0$, this is equivalent to the KdV equations.

Leibovich and Randall (1973) considered flow through a generalized tube, allowing for slow variations in tube diameter along the tube. Wavelengths were assumed to be much greater than the radius of the tube, and the variations in the tube diameter are assumed to occur on a much longer length scale than the wavelength. The modified set of equations, compared with equation (4.12), for sub-critical flows can be written as

$$A_t + c_o A_z = \epsilon \left[c_1 A A_z + c_2 A_{zzz}\right] + \delta c_3 h A_z + \alpha \delta c_4 A h_x \tag{4.15}$$

where α represents the variation in tube area with axial distance, δ represents the total variation of tube area which is assumed to be small. $Y(\alpha z) = 1 + \delta h(\alpha x)$ represents the tube area and ϵ again represents the amplitude of the waves.

By considering the limit of critical flow, as well as considering the effects of viscosity, the flow may be modeled by a modified set of Korteweg de Vries equations.

$$A_t = \epsilon \left[c_1 A A_z + c_2 A_{zzz}\right] + \delta^{\frac{1}{2}} c_1 (fA)_z + c_5 \tilde{\nu} A \tag{4.16}$$

where $\tilde{\nu}$ represents a viscosity term, $f f_x = \omega_1 h$ for a constant ω_1, and the three constants c_1, c_2 and c_5 are also to be determined.

Randall and Leibovich (1973) uses these equation to demonstrate that standing waves of finite magnitude may be trapped in a critical flow. By applying the experimental inlet profile of Sarpkaya (1971b), as well as an analytic approximation to the tube profile, it was demonstrated that the equations will allow the existence of finite amplitude standing waves for diverging tubes.

The mechanism behind the breakdown is thus suggested to be a balance between the linear amplification of a disturbance wave and diffusive effects. A soliton profile is again expected for these waves.

The reliance on small disturbance theory does, however, mean that any results for large breakdown regions must be viewed with caution. This in no way detracts from the ability of the model to suggest the mechanisms of the breakdown; merely that once breakdown has occurred, large breakdown bubbles will not be modeled.

Leibovich (1978) pointed out that the reliance of the trapped wave model on viscous diffusion could be seen as a shortcoming, when compared to experimental evidence that suggest vortex breakdown is an inviscid process.

Darmofal and Murman (1994) modified the model of Leibovich to concentrate on an analogy with shock wave formation. The analogy is based on the idea that as waves, initially in a supercritical flow, reach a critical point in the flow their amplitude will increase. In the linear case, this leads to infinite amplitude waves without velocity; the non-linear case giving a shock waves which propagates upstream to a steady position. Thus, it is suggested that if a vortex decreases from supercritical to sub-critical flow, wave trapping can occur, and vortex breakdown will result.

To verify the trapped vortex model, a series of calculations were performed on the axisymmetric Navier-Stokes equations in a swirling pipe configuration. The critical flow condition of Hall (equation (4.9)) is evaluated numerically, with eigenvalues calculated for the resultant flows. It is demonstrated that as vortex breakdown occurs, the minimum eigenvalue decreases to a negative value. This is consistent with the view that vortex breakdown will occur as the flow changes from supercritical to sub-critical flow.

Darmofal also analyses this model numerically by considering the perturbation of the flow from a near critical state. It is demonstrated that perturbation waves are initially swept downstream as the swirl ratio is increased, and then move back upstream to the final steady state position.

4.3.6 Critical Rossby Number

Spall et al. (1987) re-examined a number of existing results for vortex breakdown, in terms of a local Rossby number, defined as

$$Ro = \frac{W}{r^* \Omega} \tag{4.17}$$

where W is the characteristic inlet velocity, Ω is the inlet rotation rate, and r^* is the characteristic length scale. This scale is chosen as the radius at which the swirl velocity is a maximum. The Reynolds number is also defined in terms of r^* and W.

It is demonstrated that for $Re > 100$, a Rossby number criteria of $Ro < 0.65$ can be applied to wing-tip vortices. While this seems a reasonable fit to the available data, little insight is gained into the mechanisms behind such a breakdown. More importantly, this criteria does not seem to apply to leading-edge vortices, and hence seems less useful as a general criteria for vortex breakdown.

4.3.7 Vorticity Feedback

Brown and Lopez (1990) expanded on the numerical results of Lopez (1990) by suggesting vorticity feedback as a mechanism for vortex breakdown. This mechanism relates the angle

of the vorticity vector with the angle of the velocity vector. By assuming an inviscid flow in the central region of the flow, the equation of state was given by

$$\eta = \frac{\Gamma}{r}\frac{d\Gamma}{d\psi} - r\frac{d\mathcal{H}}{d\psi}. \tag{4.18}$$

By considering a curve C in the (r,z)-plane with radius r given by $r = \sigma(z)$ such that the stream function $\psi(r,z) = \psi_1$ is a constant. On the stream surface C equation (4.18) can be written as

$$\begin{aligned} \eta(z) &= \frac{A}{\sigma} - B\sigma \\ d\eta &= -\left(\frac{A}{\sigma^2} + B\right) d\sigma \\ A &= \Gamma(\psi_1)\Gamma'(\psi_1) \\ B &= \mathcal{H}'(\psi_1) \end{aligned}$$

where A and B are now constants on this stream surface.

By choosing a point upstream at $z = z_0$, and denoting the velocity, radius and vorticity there as (v_0, w_0), σ_0 and (η_0, ζ_0) respectively, these constants can be evaluated as

$$\begin{aligned} A &= \frac{\sigma_0 v_0}{w_0}\zeta_0, \\ B &= \frac{\eta_0}{\sigma_0}\left(\frac{v_0\zeta_0}{w_0\eta_0} - 1\right), \quad \eta_0 \neq 0, \\ B &= \frac{v_0\zeta_0}{\sigma_0 w_0}, \quad \eta_0 = 0. \end{aligned}$$

For $\eta_0 \neq 0$, the equation for η can be written as

$$\frac{\eta}{\eta_0} = \frac{\sigma_0}{\sigma}\left(\frac{\alpha_0}{\beta_0}\right) - \frac{\sigma}{\sigma_0}\left(\frac{\alpha_0}{\beta_0} - 1\right) \tag{4.19}$$

where $\alpha_0 = v_0/w_0$ and $\beta = \eta_0/\zeta_0$ are the tangents for the helix angle for velocity and vorticity respectively.

Brown & Lopez argue that a necessary condition for breakdown is the generation of negative azimuthal vorticity (η), and that from equation (4.19), if η_0 is positive, this will only occur if $\alpha_0 > \beta_0$, or equivalently $v_0/w_0 > \eta_0/\zeta_0$. They suggest a positive feedback mechanism, where a negative vorticity induces a divergence of stream surfaces, which again increases negative vorticity.

4.3.8 Shock Jump Analogy

Darmofal (1996) has proposed a simple model for vortex breakdown based on an analogy with one dimensional shocks in compressible flows. This model was found to show good agreement in predicting whether or not the flow will undergo breakdown.

The model begins by assuming a Rankine distribution

$$\begin{aligned} v(r,z,t) &= \frac{\Gamma_\infty}{2\pi\delta}\frac{r}{\delta}, \quad r \le \delta \\ v(r,z,t) &= \frac{\Gamma_\infty}{w\pi r}, \quad r > \delta \end{aligned}$$

for a constant far-field circulation Γ_∞. A far-field pressure of $p_\infty(z,t)$ is applied, and the radial velocity is assumed negligible, reducing the radial momentum equation to

$$\frac{\partial p}{\partial r} = \rho\frac{v^2}{r}. \tag{4.20}$$

The approximation is expected to be inappropriate once the breakdown region is large.

By considering conservation of mass across a control volume, the equation, in terms of the core area A can be written as

$$\frac{\partial U}{\partial t} + \frac{\partial F}{\partial z} = -S \tag{4.21}$$

where

$$\begin{aligned} U &= \begin{bmatrix} A \\ Aw \end{bmatrix} \\ F &= \begin{bmatrix} Aw \\ Aw^2 + \frac{\Gamma_\infty^2}{8\pi}\log A \end{bmatrix} \\ S &= \begin{bmatrix} 0 \\ -\frac{A}{\rho}\frac{\partial p_\infty}{\partial z} \end{bmatrix}. \end{aligned}$$

The homogeneous form of equation (4.21) can be written as

$$\frac{\partial U}{\partial t} + A_u\frac{\partial U}{\partial z} = 0 \tag{4.22}$$

for

$$A_u = \begin{bmatrix} 0 & 1 \\ c^2 - w^2 & 2w \end{bmatrix} \tag{4.23}$$

where the 'acoustic' speed c is defined by

$$c^2 = \frac{\Gamma_\infty^2}{8\pi A} = \frac{v_{max}^2}{2}. \tag{4.24}$$

A change of variable using $dV = R^{-1}dU$ gives

$$\frac{\partial V}{\partial t} + \Lambda\frac{\partial V}{\partial z} = 0 \tag{4.25}$$

where $\Lambda = R^{-1}AR = diag(\lambda_1, \lambda_2)$ with the characteristic speeds given by

$$\begin{aligned} \lambda_1 &= w + c \\ \lambda_2 &= w - c \end{aligned}$$

This leads again to the idea of supercritical and subcritical flows presented in section 4.3.4. When $|w| - c > 0$ the flow will be supercritical, whereas when $|w| - c < 0$ the flow will be subcritical.

The introduction of a non-dimensional parameter B defined as

$$B = \frac{w}{c} \tag{4.26}$$

suggests a criteria for breakdown, i.e. for $|B| < 1$ the flow is subcritical, and as suggested in section 4.3.4, breakdown will be possible. Relating this with Rossby number gives a criteria for breakdown as

$$\frac{v_{max}}{|w|} > \sqrt{2} \tag{4.27}$$

4.4 Conclusion

This chapter has given an overview of existing models for vortex breakdown, all having previously been applied to breakdown of swirling flow in a tube. The large number of previous works have been roughly grouped into six categories with each of the categories compared.

The aim of the next chapter is to look at applying one of the more successful swirling pipe models, the wave trapping model, to breakdown of flow in a confined swirling cylinder.

Chapter 5

A Confined Vortex Breakdown Model

5.1 Physical Model

The torsionally driven cavity apparatus of Figure 4.4 was first studied experimentally by Vogel (1968) and by Ronnenberg (1977), with a further detail study carried out by Escudier (1984). This apparatus, with fixed walls and a rotating bottom, has the advantage over previously studied flows that the flow can be specified with only two parameters, the Reynolds number, based on the velocity of the spinning base, and the aspect ratio of the cylinder. This compares well with pipe breakdown flow, which has been studied for a number of inflow profiles and pipe profiles.

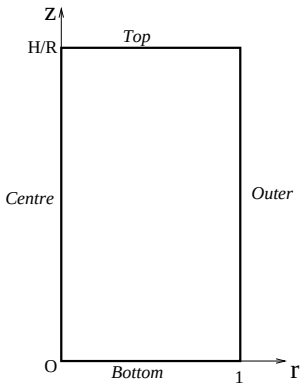

Figure 5.1: Swirling cylinder flow boundaries

Under the assumption of axisymmetry the confined swirling flow problem domain can be simplified to that shown in Figure 5.1). On this domain, the following boundary conditions are imposed

- On the boundary *bottom*:

$$u_r = 0, \qquad u_\theta = r, \qquad u_z = 0 \tag{5.1}$$

- On the boundaries *top* and *outer*:

$$u_r = u_\theta = u_z = 0 \tag{5.2}$$

- On the boundary *center*:

$$u_r = u_\theta = \frac{\partial u_z}{\partial r} = 0 \tag{5.3}$$

5.2 Steady Breakdown

To study the steady state axisymmetric swirling flow a finite element method is employed. Quadrilateral velocity elements are used, with the penalty formulation of section 2.4.1 used to eliminate the pressure p. The penalty parameter, λ, is set to 10^7, and to maintain accuracy double precision used in all calculations. Newton-Raphson iteration is performed on the resulting non-linear equations, with the solution considered converged when the maximum change in nodal velocity values between iterations is smaller than 10^{-7}. The problem is initially solved at low Reynolds numbers, with these solutions used as initial guesses for higher Reynolds number problems. The Reynolds number is stepped up in intervals of 100.

5.3 Finite Element Resolution

As discussed in Graham et al. (1995), it is extremely important when simulating the swirling cavity flow to resolve the boundary layer on the base of the apparatus. Their results show that the flow features in the interior of the flow can be significantly affected by lack of resolution.

The approach taken in this work to ensure adequate resolution is to examine the boundary layers directly, as shown in Figure 5.2. By viewing the velocity and vorticity fields it is possible to determine the approximate size of the boundary layers on the bottom and the side wall of the apparatus. Comparison with the velocity arrows placed on each nodal point shows that there are more than 10 nodal points through the boundary layer at all times. This is enough resolution to resolve these boundary layer with quadrilateral finite elements.

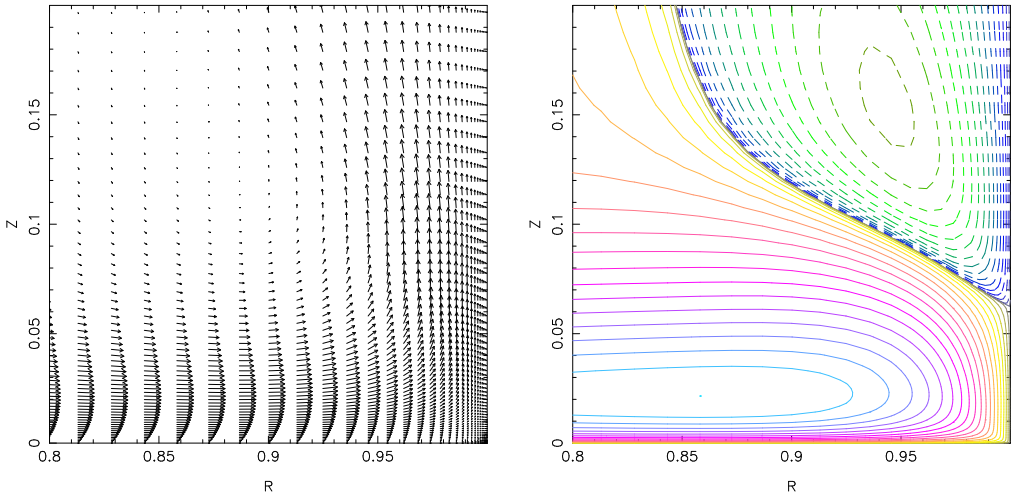

velocity vectors

radial velocity u_r

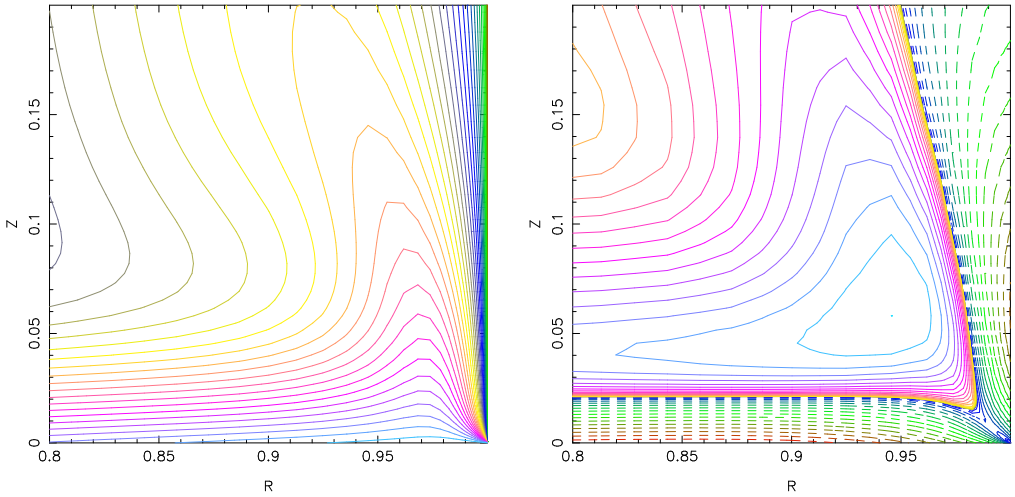

azimuthal velocity u_θ

vorticity $\nabla \times \mathbf{u}$

Figure 5.2: Close up of bottom right corner of swirling flow, $Re = 1995$, $H/R = 2.5$

Another point of interest in Figure 5.2 is that a significant boundary layer exists on the outer wall of the apparatus. While the work of Graham et al. (1995) concentrates the mesh on the bottom boundary layer, it is clear that resolution in the radial direction in the lower part of the flow will also influence the internal flow features.

5.4 Breakdown Features

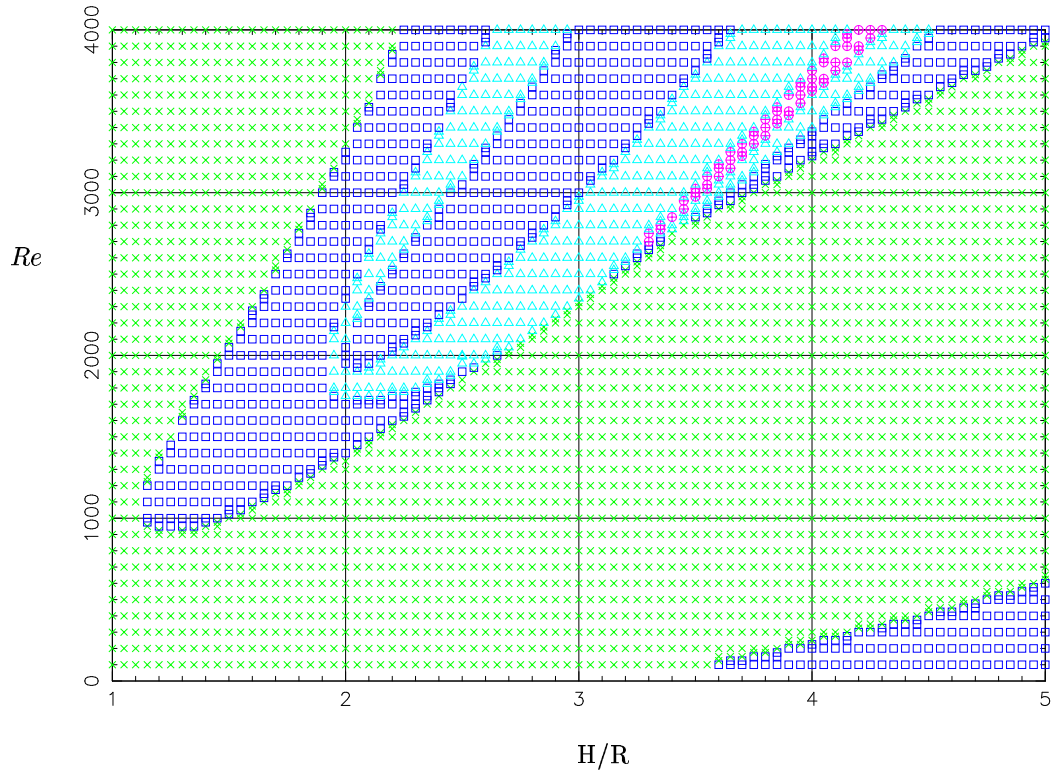

Figure 5.3: Existence of breakdown bubbles.
$\times$ 0 bubbles, $\square$ 1 bubble, $\triangle$ 2 bubbles, $\oplus$ 3 bubbles

Escudier (1984) presents an experimental study of vortex breakdown which included the so-called stability diagram, where the number of breakdown bubbles was presented as a function of the Reynolds number and the cylinder aspect ratio. Figure 5.3 shows the corresponding stability diagram produced using the current steady model. The agreement is very good, once allowance is made for the slightly different notation. In the current results, areas such as those around $H/R = 2.75$, $Re = 3000$ are indicated as a single bubble. In this

case, the two bubble have merged into one larger recirculation zone; an example of this flow configuration is given in Figure 5.4.

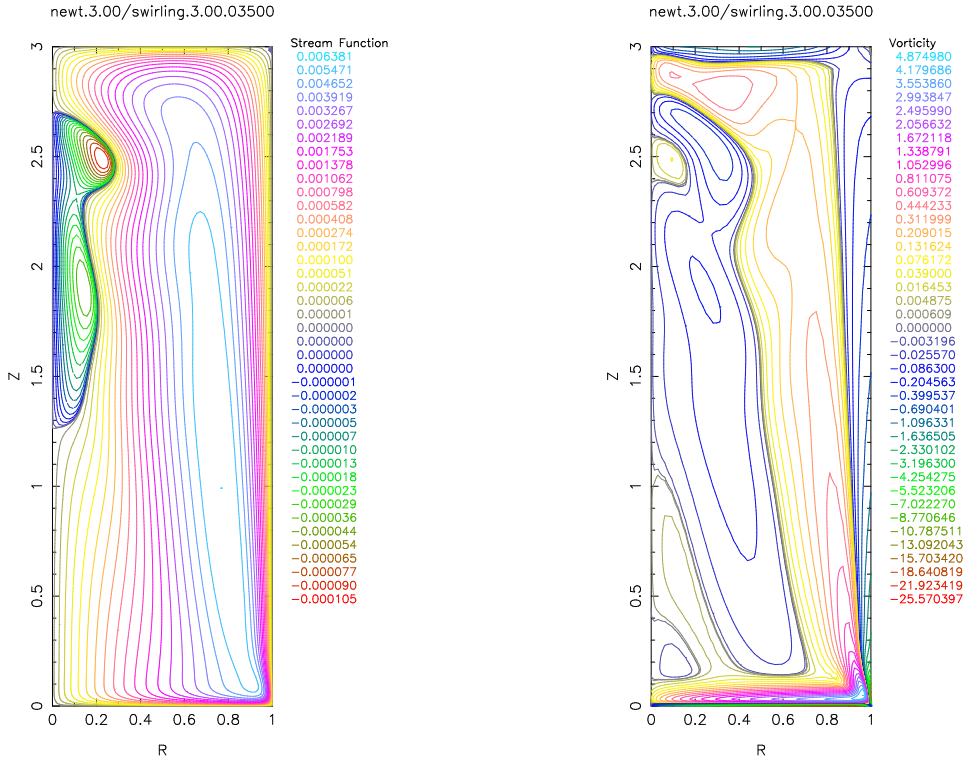

Figure 5.4: Single merged breakdown at $Re = 3500$, $H/R = 3.0$.
(a) Stream Function ψ (b) Vorticity ζ

In viewing the streamlines such as those in Figure 5.4, the method of choosing contour levels of Lopez (1990) is followed, where the contour values are cubicly stretched towards zero. This leads to clearer visualization of recirculation zone, where the flow velocities are typically much smaller.

Two typical examples of the onset of breakdown in the confined flow as the Reynolds number is increased are shown in Figures 5.4 and 5.4. These figures show the onset of vortex breakdown for two different aspect ratios, $H/R = 2.5$ and $H/R = 4.0$, as the Reynolds number is increased. Contour levels of the stream-function ψ are displayed with 20 positive and 20 negative values with the intervals again being cubicly stretched towards zero.

Both of these examples show the progress with Reynolds number of the confined flow as it moves from a uni-directional recirculation zone into a flow pattern with waves on the center

vortex core, and finally to a flow with at least one recirculation zone.

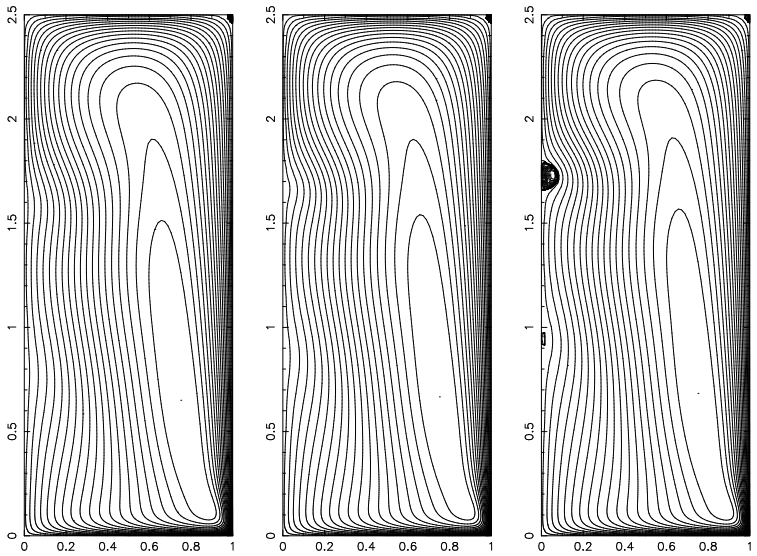

Figure 5.5: Stream function for breakdown in torsionally driven cavity $H/R = 2.5//$ (a) Re = 1740, (b) Re = 1840, (c) Re = 1900

5.5 One Dimensional Wave Model

The aim of the current section is to test the breakdown model of Darmofal and Murman (1994), which suggests that wave-trapping and focusing can be used as a mechanism to describe vortex breakdown. While this model was successfully applied to flow in a divergent pipe, the extension of this model to the confined cylinder flow is less clear. In particular, attempts by Jones et al. (1998) to directly visualize wave trapping in the confined cylinder proved to be less than conclusive.

To examine the wave trapping model, firstly consider a steady mean flow without breakdown with a velocity field $u = (U(r,z), V(r,z), W(r,z))$. The flow is assumed to be quasi-cylindrical, that is $\frac{\partial U}{\partial r} \ll \frac{\partial U}{\partial z}$. By considering an axial length scale L and a length scale for radial perturbations of λ, such that $\lambda/L \ll 1$, to first order the flow can be considered as a function of the stream-function perturbation

$$\hat{\psi} = F(r)\exp(\gamma z) \tag{5.4}$$

where γ is an axial wavenumber. The governing equation for the perturbation field, from

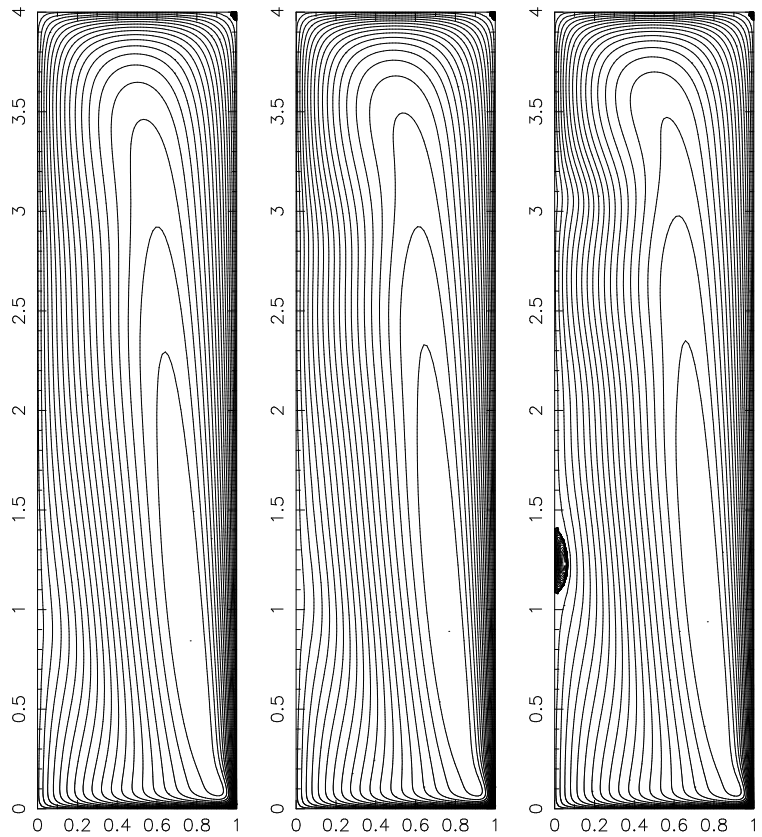

Figure 5.6: Stream function for breakdown in torsionally driven cavity, $H/R = 4.0$// (a) Re = 2900, (b) Re = 3100, (c) Re = 3300

Hall (1967), is then

$$r\frac{d}{dr}\left(\frac{1}{r}\frac{\partial F}{\partial r}\right)+\left[\gamma^2-\frac{r}{W}\frac{\partial}{\partial r}\left(\frac{1}{r}\frac{\partial W}{\partial r}\right)+\frac{1}{r^3W^2}\frac{\partial \Gamma^2}{\partial r}\right]F=0 \tag{5.5}$$

where $\Gamma = rV(r,z)$ is the mean flow circulation. This equation is an eigenvalue problem for γ_0 dependant only on r for each value of z.

Darmofal used this model for pipe problem to show that the eigenvalues γ_0^2 of the system become negative just before breakdown occurs, and argued that this represented a change in nature of the flow from a super-critical flow, with information traveling downstream only, to a sub-critical flow in which information (and in particular small perturbations) could move back up stream and be trapped. The point of this trapping is said to correspond with the breakdown point.

To extend this idea to the confined cylinder it is necessary to choose a region of the flow that is similar to a pipe, and hence meets the necessary requirements for the use of equation (5.5). The region $0 \le r \le \frac{1}{2}$ and $.1 \le z \le H - .1$ is used to define the base flow. At any given Reynolds number, a finite element approximation to equation (5.5) is solved using the LAPACK routine DGEEVX at each axial position z.

5.5.1 Wave Model Results

Figures 5.7 and 5.8 indicate the axial velocities and eigenvalues γ_0^2 of the flow for two different aspect ratios. It can be seen that the flow becomes sub-critical before the flow has broken down, but that the physical location of the breakdown points correspond well with the location of vortex breakdown bubbles, appearing for $-w(0,z) < 0$.

Figure 5.9 shows the minimum axial velocities and eigenvalues as the Reynolds number is increased. It is apparent that the flow becomes sub-critical at a Reynolds lower than that required for flow reversal to occur. This is consistent with the results of Darmofal in the pipe apparatus. Note that when $\gamma_0^2 = 0$, upstream perturbations of infinite wavelength can be trapped. The length of wave perturbation possible is given by Hall as $L = 2\pi/\sqrt{-\gamma_0^2}$. Adjusting the required minimum eigenvalue to allow for a shorter wavelength moves the two events, negative eigenvalues and reverse flow, closer together without removing the gap completely.

Another possible reason for this discrepancy between negative eigenvalues and reversal of flow is the effect of feedback on vortex breakdown on the global flow properties. In particular, the appearance of vortex breakdown bubbles has a direct effect on the upward motion near the outside of the cylinder. To examine this idea further, the next section outlines details of a time-dependant study of vortex breakdown.

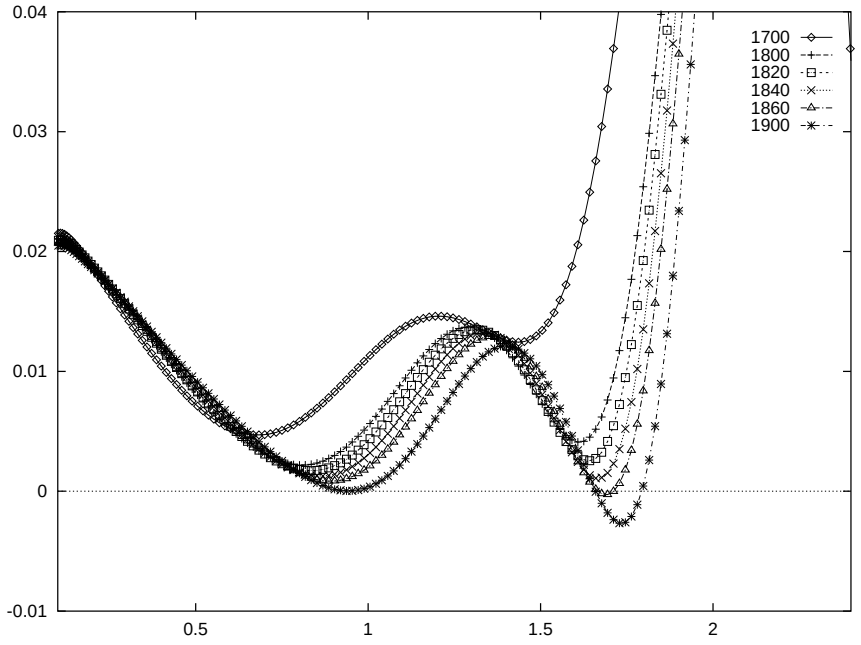

(a)

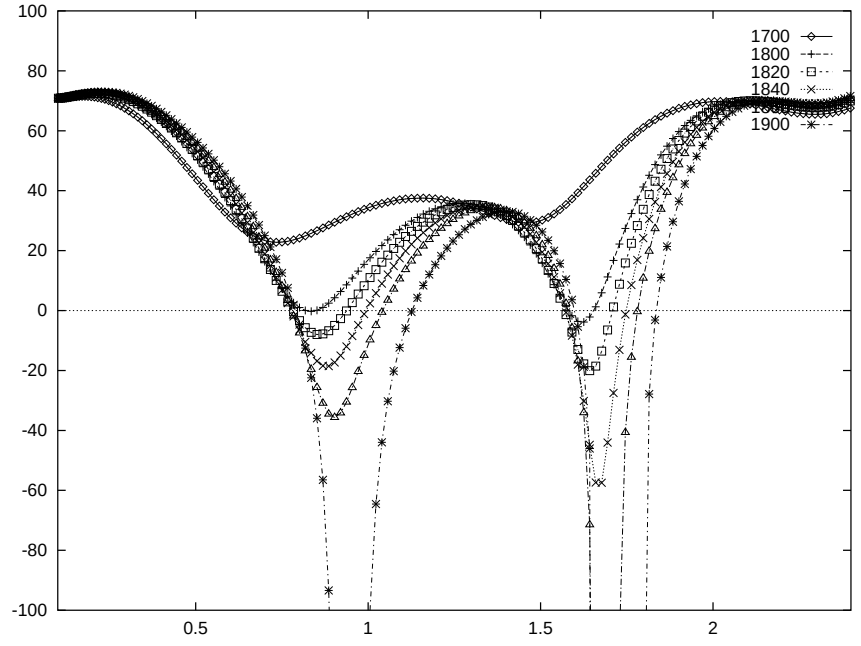

(b)

Figure 5.7: (a) Axial velocities $-w(0,z)$ and (b) Minimum eigenvalues $\gamma_0^2(z)$ for $H/R = 2.5$

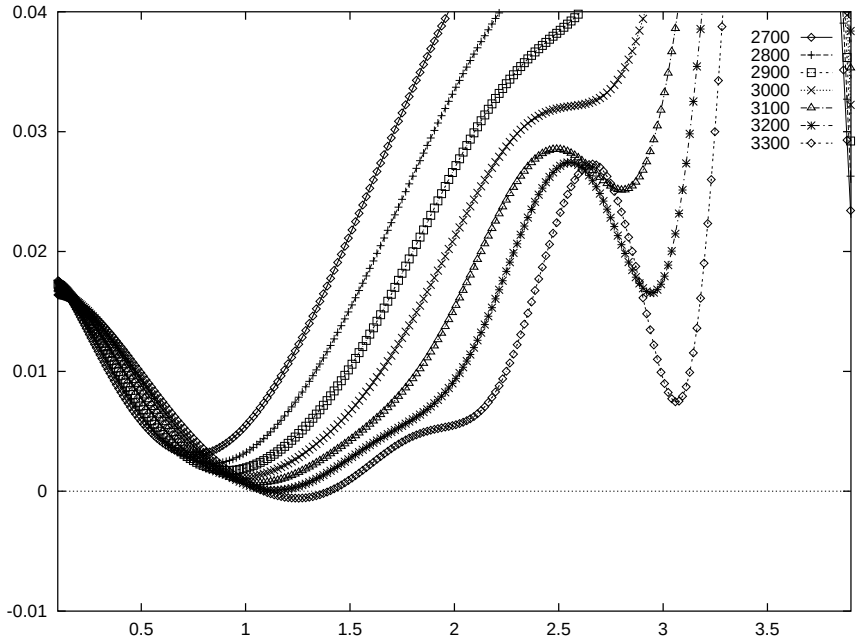

(a)

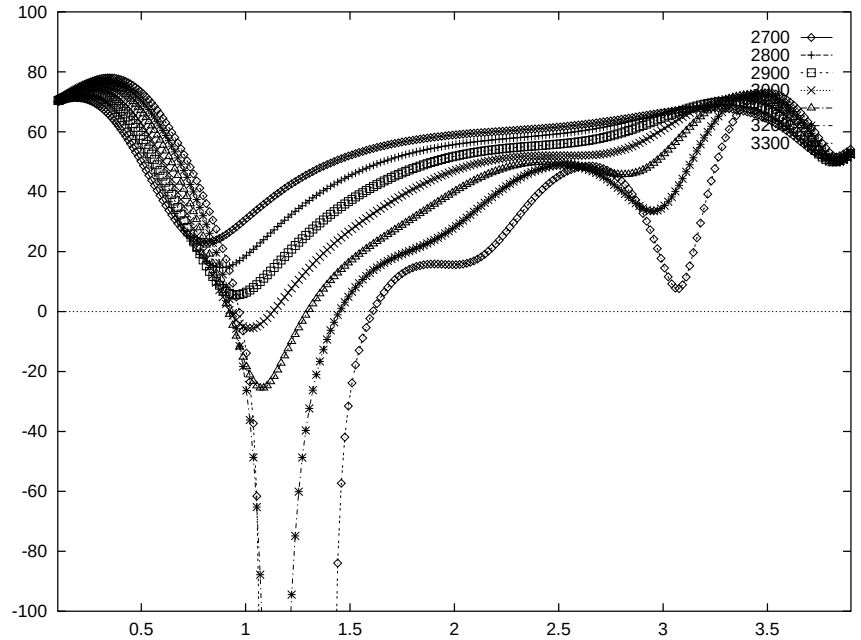

(b)

Figure 5.8: (a) Axial velocities $-w(0,z)$ and (b) Minimum eigenvalues $\gamma_0^2(z)$ for $H/R = 4.0$

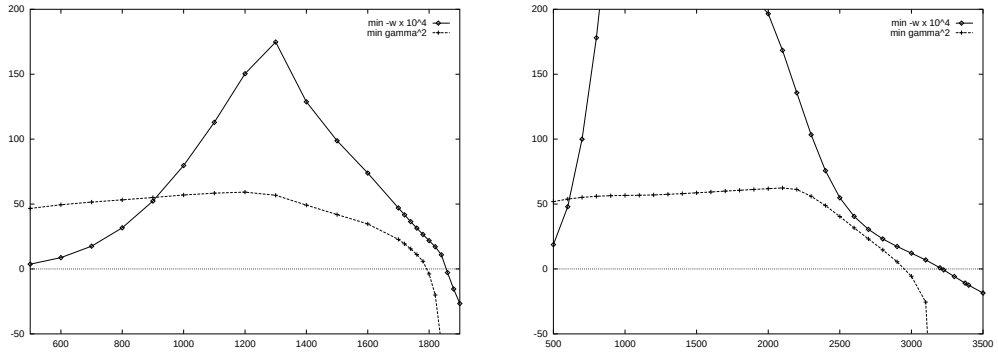

(a) (b)

Figure 5.9: Minimum velocity $-w(0,z)$ and eigenvalues γ_0^2 for (a) $H/R = 2.5$ (b) $H/R = 4.0$

5.6 Unsteady Breakdown

In the previous section it was shown that the wave model of vortex breakdown is reasonably consistent with breakdown results in the confined apparatus. It seems that the flow pattern is capable of supporting infinitesimal perturbations in the upstream direction. The aim of this section is to compare the behavior of the wave model in the time dependant confined flow in the context of this wave model.

5.6.1 Axisymmetric Spectral Element Method

In solving for the time-dependent swirling cavity problem, the spectral element method has been utilized in conjunction with the stiffly-stable multi-step splitting scheme outlined in section 2.4.2.

Unlike the finite element method, the use of the axisymmetric form of the equations, with it's corresponding $1/r$ terms, provides some difficulties in the spectral element method. Since the spectral element method uses integration points on the nodal points, the points on the axis $r = 0$ require special treatment. For these elements, Gauss-Radau-Legendre elements are employed. These element do not have an element on the left edge (at least in the direction employed here; it's possible to remove either edge) and the corresponding weight functions are based on the Jacobi polynomials $P^{(1,0)}$. This procedures seems to be similar to that mentioned in Tomboulides and Orszag (2000).

In practice there are only a few alterations to be made to the Cartesian equations to allow for axisymmetric flow. The extra terms of Section 2.4.1 are once again included, and the Jacobian of integration becomes $rdrdz$, rather than the more familiar $dxdydz$.

The only other significant modification that is necessary involves the divergence of the pressure equation (2.43). As the flow domain is effectively a bounded, the pressure can only determined to within an arbitrary constant (a fact that is verified by substituting $p^1 = p + C$ for a constant C into equation (2.1) with the appropriate boundary conditions). Because the method used is an inexact projection method, with an approximate Poisson equation being solved, it was found that during integration the sum of the divergence used on the right side of this equation would drift slightly from zero (usually less than 10^{-6} per time-step). This in turn leads to convergence difficulties in the iterative solver. To overcome this, a technique similar to that of Strikwerda (1984) is used, where the sum of the right-hand-side of equation (2.45) is set to zero.

5.6.2 Numerical Convergence

While spectral element methods offer high order accuracy for smooth problems, the swirling cavity problem has an inherent singularity in the specification of the boundary conditions: at the outer edge of the rotating lid there is a jump in velocity. In experiments this jump is, of course, not infinite. In practice, the gap width is order of 1% of the cylinder radius. Because of this large jump in gradient near the edge of the spinning lid, it is important to confirm that the numerical solutions are converging.

The approach used to confirm convergence is to study the swirling cavity problem at a Reynolds numbers of $Re = 100$ with an aspect ratio of $H/R = 1.5$. A start-up simulation is then performed up to a time of $t = 10$, at which point the r velocity in the center of the mesh, point $(0.5, 0.75)$, is the evaluated. Since this point will often not correspond to a nodal point, the natural spectral element interpolation (using Lagrangian polynomials) is used to evaluate the flow values. The 'exact' value of the velocity is determined from a very high resolution simulation with $n = 20$ and $p = 16$.

The mesh used to study convergence consists of $n \times nH/R$ elements where H/R is the aspect ratio of the rig, here 1.5, and n is resolution parameter. Each element is of order p. An example of the macro-mesh for $n = 6$ is shown in Figure 5.10. Both h and p type convergence are studied; that is, varying the number of element n and the element order p respectively.

Figure 5.11 shows the result of maintaining a constant element order and varying the number of elements in the mesh. The value of h used in the diagram is simply the inverse of the number of elements, which is also equal to the average side length of the elements. While the $p = 9$ solution showed slightly lower error values, the convergence rate is slightly worse (order of 4.98) than that of the $p = 7$ solution (with order 5.43).

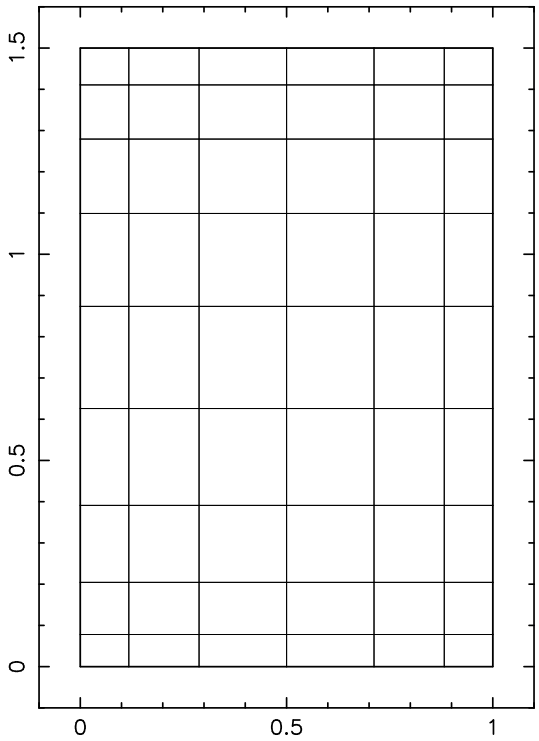

Figure 5.10: Macro-mesh for time-dependant swirling convergence study, $n = 6$, $H/R = 1.5$.

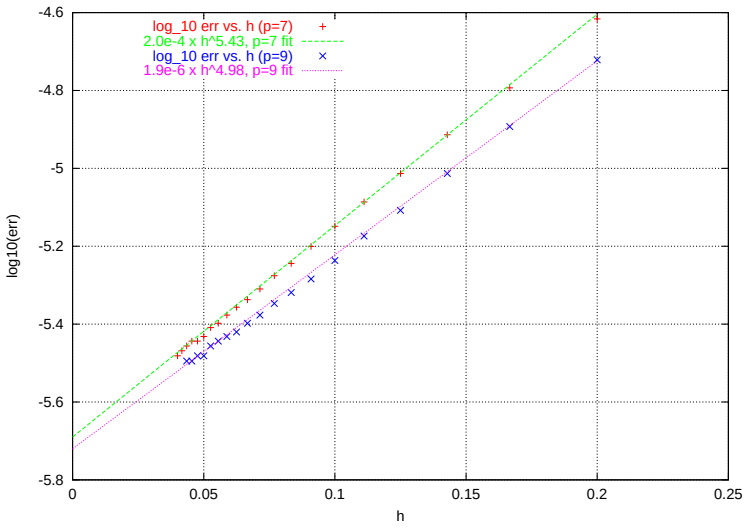

Figure 5.11: h convergence of swirling cavity spectral element solution

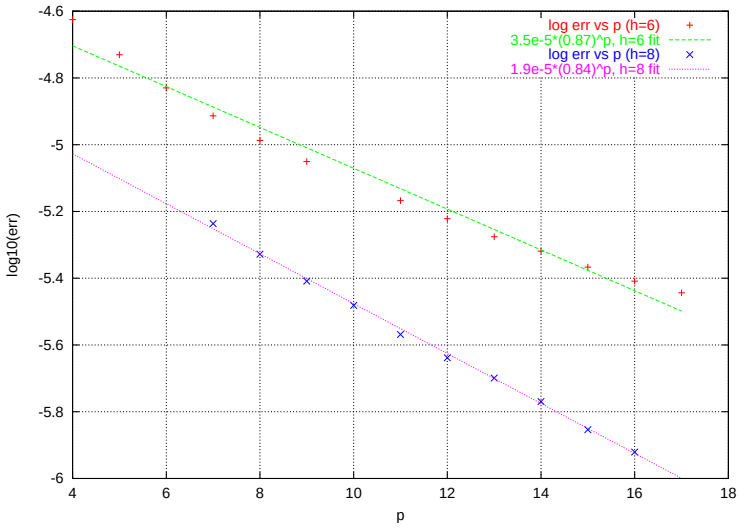

Figure 5.12: p convergence of swirling cavity spectral element solution

Figure 5.12 shows the results of keeping a fixed element size and varying the order of the element. As the order of the element is increased, the error in the solution is reduced exponentially, especially when looking at the $n = 8$ results. The $n = 6$ show some loss of exponential convergence for larger values of p. This can be attributed to the relatively large element size compared with the steepest gradients in the bottom right corner, and to the lack of smoothness in the boundary conditions.

While this technique shows that is possible to achieve good convergence on the swirling cavity apparatus using spectral elements, it is known that as the Reynolds number is increased the boundary layers will become thinner. To make sure these boundary layers are properly resolved, the higher Reynolds results are simulated on a modified form of the mesh of Figure 5.10. A three element wide layer of elements is placed along the bottom and outer boundaries with a width of $3/\sqrt{Re}$. Theses elements, which are unstretched, provide the necessary resolution in the boundary layer to maintain exponential convergence.

5.6.3 Transition to Breakdown

Figure 5.13 shows the onset of the confined vortex breakdown with an aspect ratio of $H/R = 2.5$ at a Reynolds number of 1900. As seen in Figure 5.3, this parameter set is just inside the region of breakdown, and in the previous section was seen to show negative minimum eigenvalues, and hence be capable of sustaining upstream standing waves.

The first observation from figure 5.13 is that the breakdown in the confined apparatus

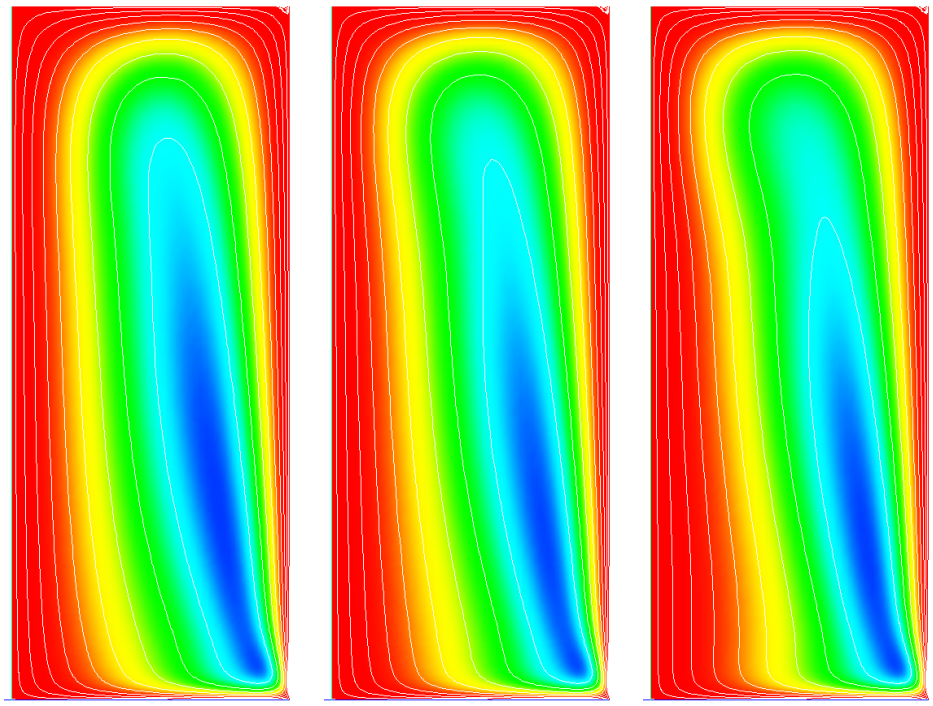

$t = 130$ $t = 140$ $t = 150$

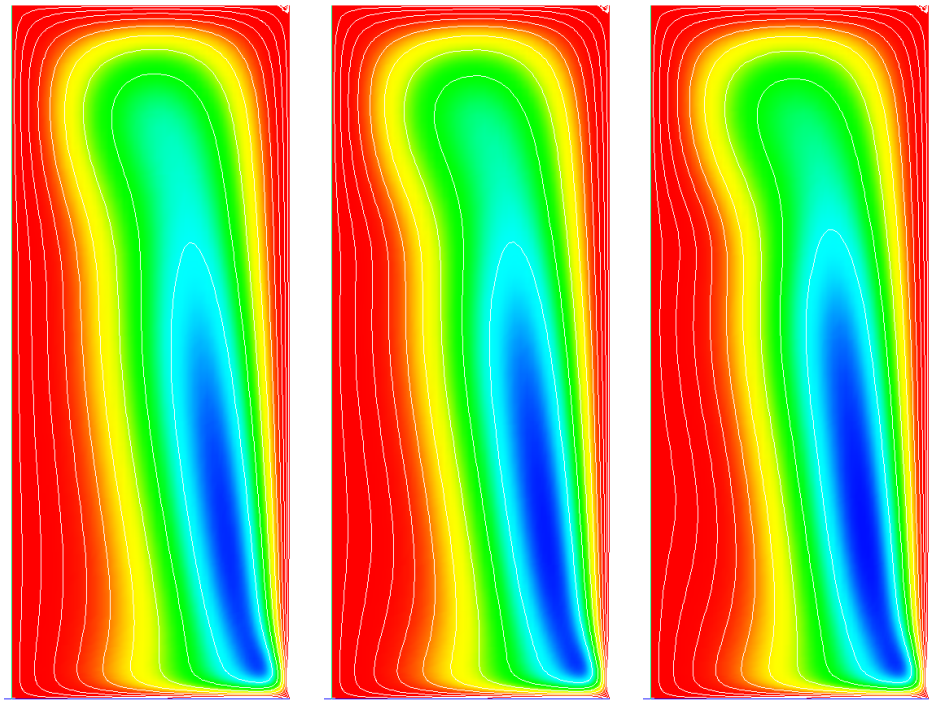

$t = 160$ $t = 170$ $t = 180$

Figure 5.13: Onset of Vortex Breakdown. $Re = 1900$, $H/R = 2.5$. $10^{-6} \leq \psi \leq 0.008$, cubicly stretched. Blue is positive.

occurs more slowly that the rapid onset of breakdown in the pipe apparatus. While breakdown in the pipe is usually described as a jump in states, the current change occurs more slowly. The second observation is that between $t = 130$, where the flow is yet to show signs of breakdown, and $t = 180$, where the flow is showing significant waviness, there is a reduction in size of the blue area near the outer wall, corresponding to the most positive stream-values. This indicates that the upward jet, and therefore the recirculating flow near the top of the cylinder apparatus, have slowed due to the start of the waviness in the flow. The reason for this is relatively straightforward; the increase in width of the central core region reduces the amount of room for fluid to flow back up the apparatus.

Figure 5.14 shows the onset of reverse flow, the so-called breakdown bubble. After the initial appearance of the breakdown bubble at $t = 185$, the bubble grows and moves upstream. This behavior is consistent with vortex breakdown in the pipe apparatus, and is also a features of Darmofal's wave propagation model for breakdown. However, beyond $t = 200$ the vortex breakdown bubble begins to reduce in size. A likely mechanism for this reduction in size is the effect of breakdown on the upward fluid motion, which is slowed due to the increase in core size. This pattern of appearing and disappearing breakdown bubbles is repeated for several cycles, and suggests a mechanism where the breakdown bubble size is eventually in balance with the pressure exerted by the upward moving fluid stream near the outer part of the cylinder.

While the wave model of vortex breakdown has a role to play in predicting vortex breakdown in the confined cylinder, it is only a necessary condition for the appearance of vortex breakdown in the steady state. Once the vortex breakdown bubble has formed, the flow must have sufficient strength to overcome the loss in circular motion due the existence of the breakdown bubble. This feedback cycle tends to dampen the appearance of the breakdown bubble in the cylinder apparatus, giving a more steady onset of breakdown compared with the dramatic transition seen in pipe and free flow breakdown.

This feedback mechanism gives a possible explanation for one key difference between breakdown in the pipe apparatus and confined apparatus. Wang and Rusak (1997) have suggested that vortex breakdown can be seen as a transition between two possible vortex states. This idea seems inconsistent with the results of the confined apparatus, where the breakdown onset occurs as a gradual transition. Tsitverblit (1993) showed that steady axisymmetric breakdown is a gradual process, and that bifurcation plays no role in the onset of confined vortex breakdown. By allowing for feedback between the upward motion and the downward, vortex core motion in the cylinder, these two process for vortex breakdown can be reconciled. By moving to a closed system, the swirling cavity, the jump in state apparent in previous breakdown models becomes a steady transition with Reynolds number of flow

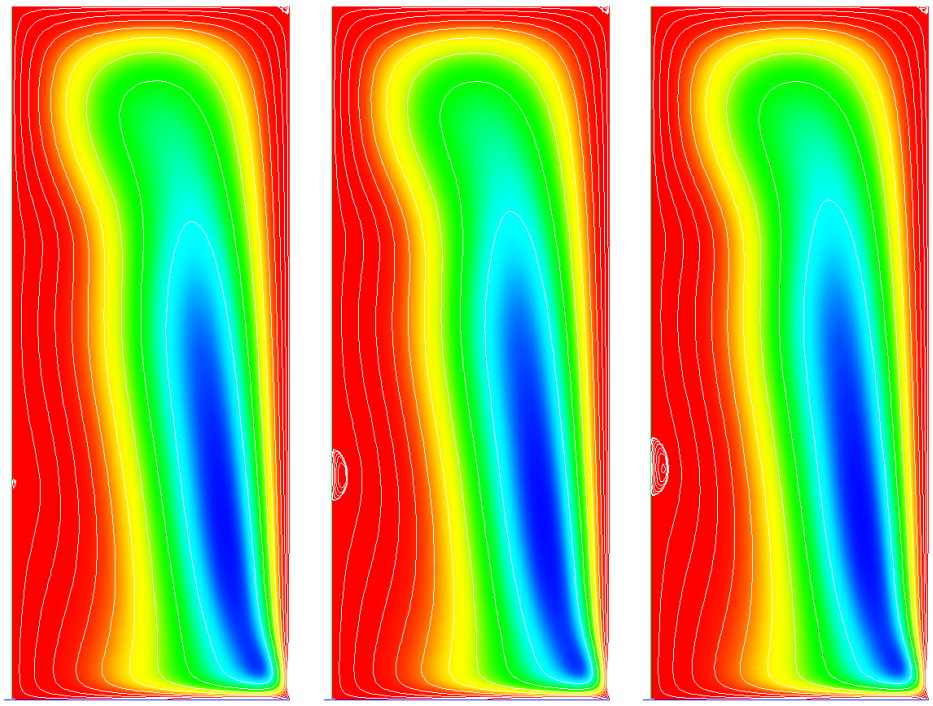

$t = 185$ $t = 190$ $t = 195$

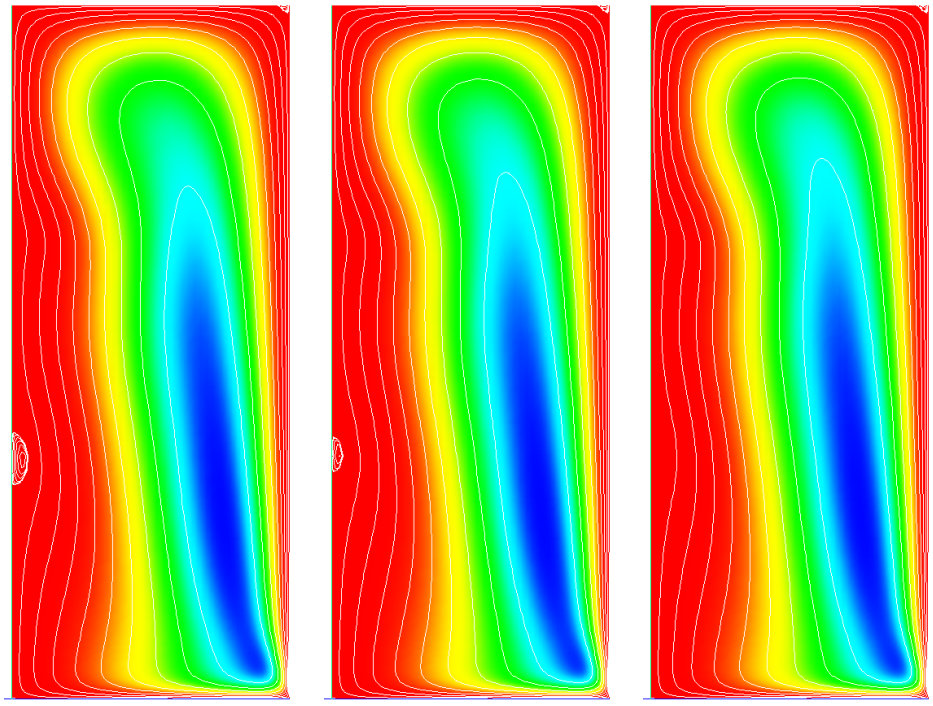

$t = 200$ $t = 205$ $t = 210$

Figure 5.14: Transient vortex breakdown bubble. $Re = 1900$, $H/R = 2.5$. $10^{-6} \leq \psi \leq 0.008$, cubicly stretched. Blue is positive.

features, at least when viewing the steady solution at infinite time.

The incorporation of feedback into the breakdown model may also explain the failure to find a simple wave growth by Jones et al. (1998). By considering only changes between steady state solutions, it is difficult to observe wave propagation as a breakdown mechanism, since the balance between upstream and downstream forces will already play a part at Reynolds numbers where vortex breakdown is not apparent.

5.7 Conclusion

The wave trapping models originally put suggested by Squire, and further enhanced by Hall, Leibovich and Darmofal has successfully been applied to a torsionally driven cavity. By considering a case where there is a discrepancy between the breakdown state suggested by the wave-propagation criteria and that seen in the actual flow, it was seen that feedback in the closed system has a substantial effect on the overall flow pattern, acting to reduce or remove the breakdown bubbles. After making allowances for the fundamentally different stability properties of closed systems, these results suggest that the wave trapping model provides a robust explanation for vortex breakdown.

In the next chapter a different physical problem is tackled. As a means of validating the current numerical model for time-dependant wake flows, a series of simulations are performed on two-dimensional cylinder wakes, as well as simulation of sphere flow at low Reynolds numbers.

Chapter 6

Two Dimensional Wake Flow

6.1 Background

This chapter outlines a series of simulations of two-dimensional flow past a cylinder and axisymmetric flow past a single sphere. As both of these flow configurations have been studied in great detail they are useful test problems to establish the validity of the current numerical model.

The study of flow past a cylinder, dating back more than 100 years, covers a wide range of numerical and experimental work over a complete range of Reynolds numbers. This body of work is reviewed in detail by Williamson (1996). The focus of the current study is to evaluate the time-dependant cylinder wake flow in the Reynolds number range of 100 to 300 under the assumption of two-dimensional flow. At a range of Reynolds numbers the wake is known to exhibit a single frequency shedding, and is hence suitable for validating that the code is correctly simulating shedding wake flows.

The second test problem considered in this chapter is flow around a single sphere at Reynolds numbers up to an including 200, where the flow is known to be axisymmetric. As well as providing a starting condition for the higher Reynolds number flows, these solutions are also compared against previous results to validate the numerical scheme and choice of numerical mesh.

6.2 Mesh

Figure 6.1 shows the mesh C1 used to simulate two-dimensional cylinder flow. The width of the simulation domain is known to have a significant effect on the frequency response, and

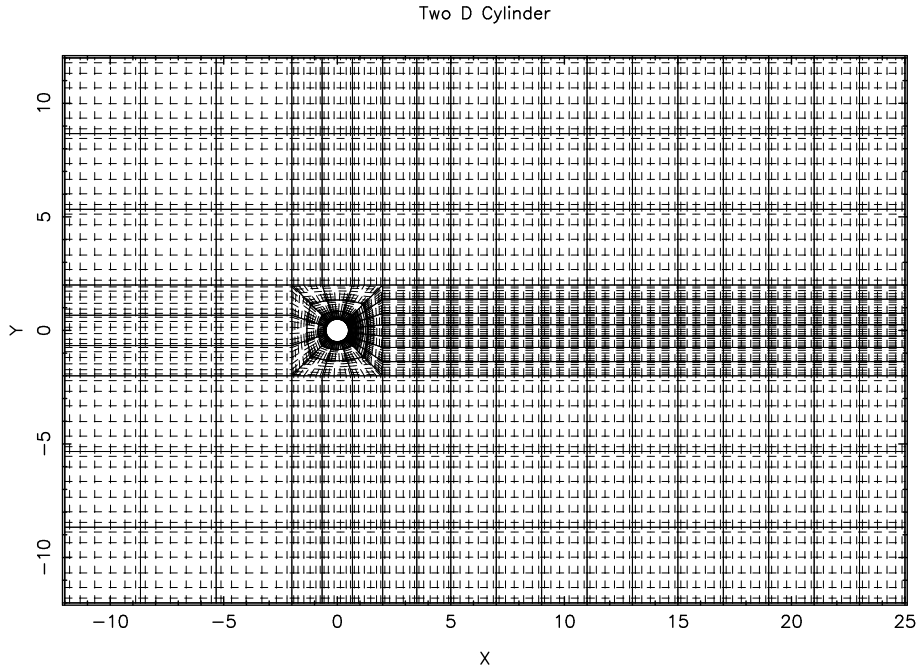

Figure 6.1: Spectral element mesh for two dimensional flow past a cylinder

the current mesh has a height of $24d$ and upstream distance of $12d$ where d is the diameter of the cylinder. The mesh contains 265 seventh order elements (each element consisting of an 8×8 grid of nodes).

To increase resolution around in the boundary layer around the cylinder, the elements near the surface are stretched towards the surface. Only the exterior points of the elements are stretched; the internal elements are located on the Gauss-Lobatto-Legendre points to maintain spectral accuracy.

To allow for a reduction in the number of matrix systems stored, the wake elements of the mesh are set to two constant lengths in the stream-wise direction rather than gradually increasing the element size downstream. For elements with the same spatial structure the element matrices of the flow equations have the same values, and this fact is used to reduce memory requirements in the code. After being built, each element matrix is compared to the existing matrices, firstly via a hash function and secondly via a more accurate test. If the element matrices are the same, one of the matrices is deleted and the common matrix is shared through a pointer. This leads to a significant amount of reduction in total storage for the simulation, a factor which becomes important for three-dimensional simulations.

6.3 Evaluating Strouhal number

The Strouhal number is a non-dimensionalised frequency, defined as

$$St = 2fR/U \tag{6.1}$$

where f is the dimensional frequency in the flow, R is the radius of the cylinder, and U is the inlet velocity.

To calculate the Strouhal frequency of the wake several points inside the flow are examined. A discrete Fourier transformation (Press et al. (1992)) is performed on N data points

$$F_n = \sum_{k=0}^{N} f(k) e^{-2\pi i n k/N} \tag{6.2}$$

where $f(k)$ is the data value at time t_k and n represents the discrete frequency. This is a one sided power spectrum, and is normalized by total power so that the area on the spectrums in the following graphs add to one.

To examine the Strouhal number of the flow, several points within the flow field are examined. The start up flow is not expected to be periodic, and examination of the point values is used to determine when the flow has become periodic. Values after this time are used to determine the flow spectrum.

6.4 Strouhal Number of Cylinder Flow

To verify the accuracy of the wake flow, a comparison of the wake frequencies at a number of Reynolds numbers is made. Before this comparison can be meaningfully made, it is important to verify that the wake is shedding in a periodic way.

To check the Strouhal number, flow past a cylinder is simulated on the mesh C1 of Figure 6.1. A timestep of $\Delta t = 0.005$ is used, and the flow field is initialized with a 1% random noise in the velocity field to encourage the onset of shedding.

Figure 6.2 shows the velocity and pressure profiles of the flow at $x = 10$, $y = 0$. Examination of the flow profile in Figure 6.2(a) shows that the onset of shedding flow beings at around $t = 30$, and that by $t = 75$ the flow has settled down to a periodic flow pattern. Part (b) of the same figure, show the flow values for $100 \leq t \leq 150$ shows that the structure of the flow is largely periodic. To measure the Strouhal number, the flow features for $100 \leq t \leq 300$ have been used.

The two strong peaks correspond to the Strouhal frequency and twice the Strouhal frequency. As expected, the frequency of the horizontal velocity and pressure in the wake is twice that corresponding to the Strouhal frequency.

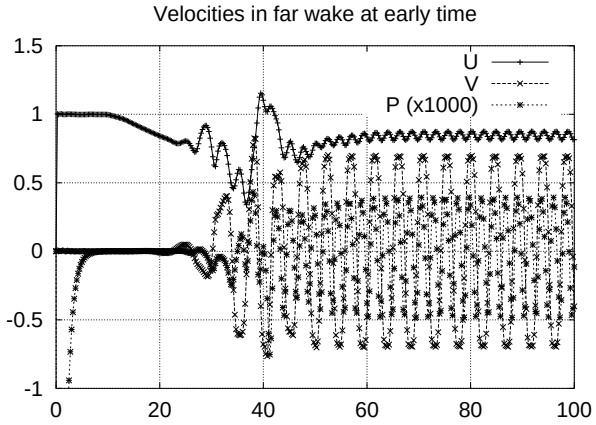

(a)

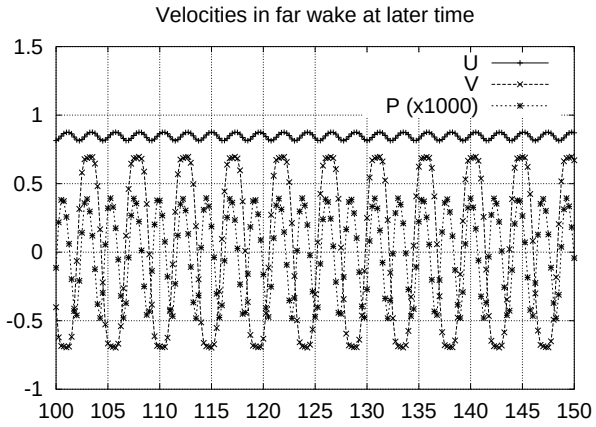

(b)

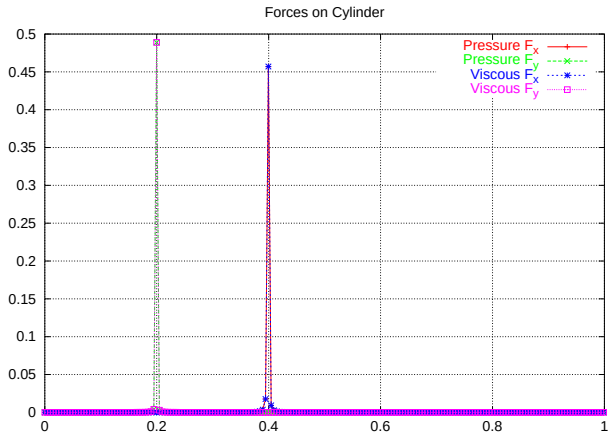

(c)

Figure 6.2: Velocities, Pressure and corresponding spectrum. $(100 < t < 200)$ in far wake, $Re = 200$

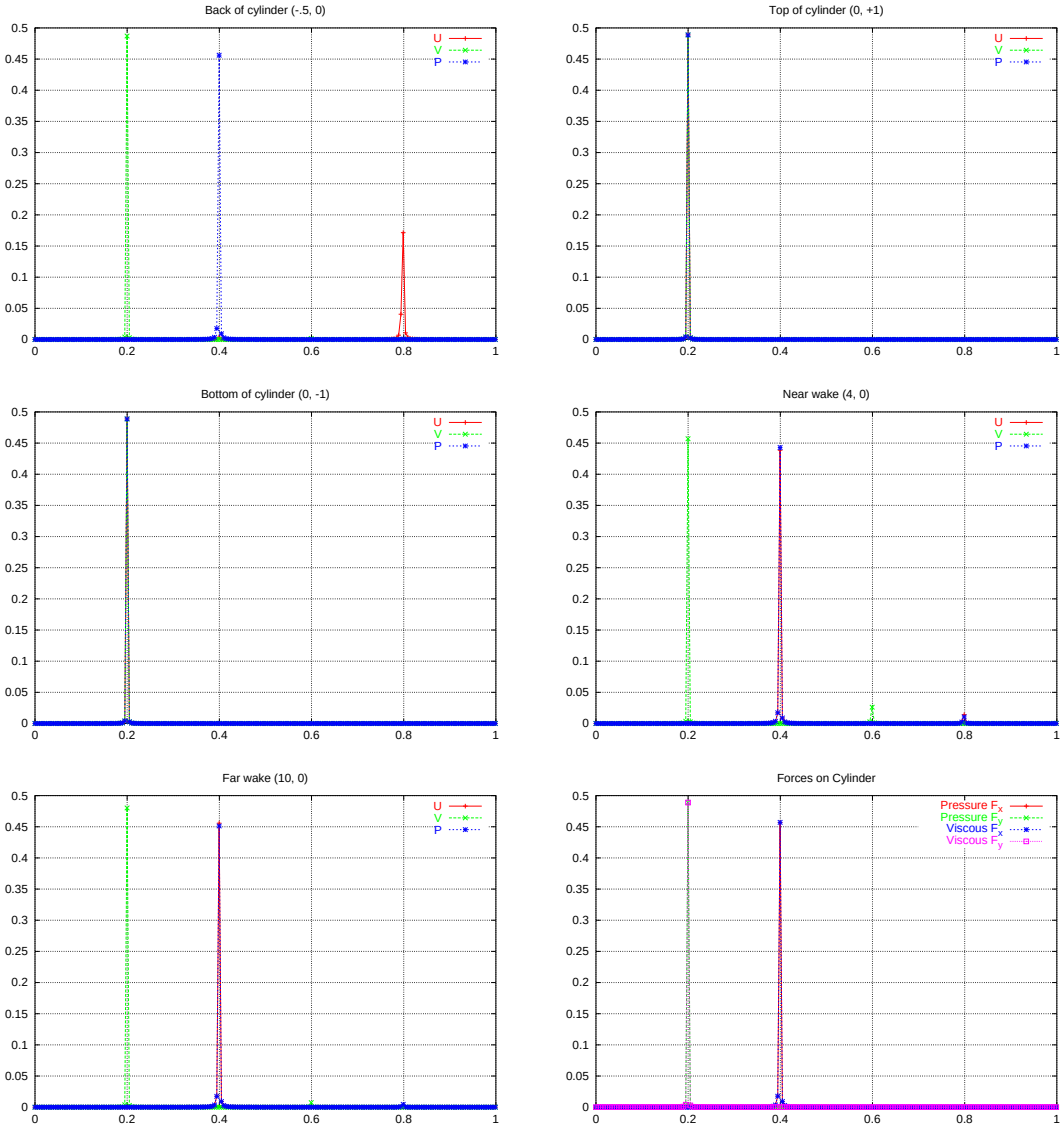

Figure 6.3: Spectrum for two dimensional shedding wake flow, $Re = 200$

In Figure 6.3 the spectrums of the flow quantities at several points in the flow are shown, as well as the spectrum of the force on the cylinder at $Re = 200$. These diagrams show the presence of one fundamental frequency at $St = 0.20$, with several quantities showing peaks at multiples of this amount, as expected. Clearly this fundamental frequency dominates, and the wake undergoes a simple, single frequency shedding as expected.

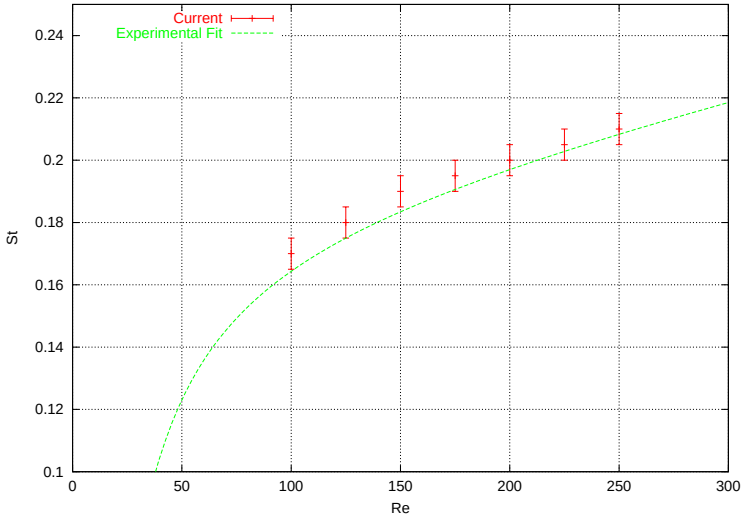

Reynolds Number	Calculated Strouhal (St)	Experimental Fit Williamson (1988)
100	0.170	0.164
125	0.180	0.175
150	0.190	0.184
175	0.195	0.191
200	0.200	0.197
225	0.205	0.203
250	0.210	0.208

Figure 6.4: Strouhal Number vs. Reynolds Number for two dimensional cylinder wake

Figure 6.4 shows the Strouhal number against Reynolds number compared to the universal Strouhal number curve of Williamson (1988);

$$St = \frac{A}{Re} + B + C\,Re \tag{6.3}$$

where the constants are $A = -3.3265$, $B = 0.1816$ and $C = 0.00016$. To calculate the frequencies, the vertical force on the cylinder is measured between $t = 100$ and $t = 300$, giving a resolution for the Fourier transformation of $\Delta t = \pm 0.05$. The trend of these Strouhal results show that the calculated Strouhal number is slightly high. The current flow domain is restricted in width to $24D$ and this is known to have an effect on the Strouhal number. In Thompson et al. (1996) the numerically calculated Strouhal number of similar spectral element mesh is compared to the Williamson's curve and found to give good agreement for a domain width of $50D$. However, for a domain width of $7D$ the Strouhal number was seen to be over-estimated by around 0.20. The current error of around 0.05 for a domain size of $24D$ seems to agree with this general trend. Also encouraging is that the error in Strouhal number decreases as the Reynolds number is increased, as would be expected if blockage is the cause.

6.5 Effect of Time-Step on Strouhal Number

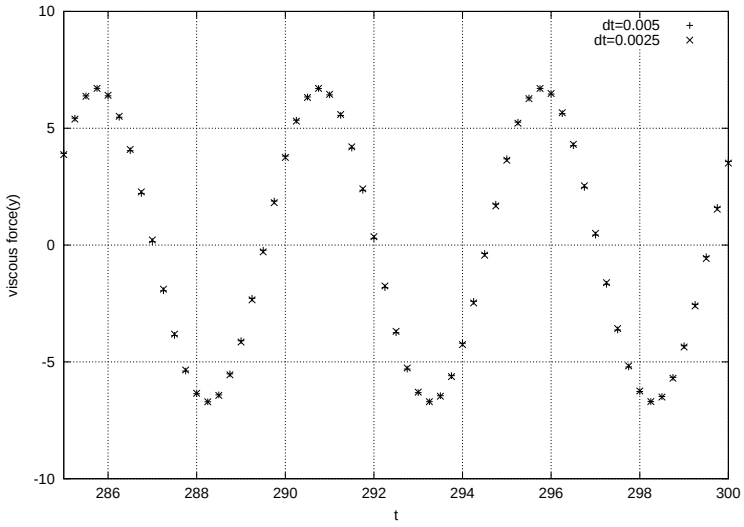

Figure 6.5: Effect on timestep on cylinder force

To test the effect of the time-step on the flow properties, a simulation of the two-dimensional cylinder flow at $Re = 200$ with a timestep of 0.005 is restarted at $t = 100$ with a reduced timestep of 0.0025. Both simulations are then evolved to $t = 300$, where the forces on the cylinder cylinder are compared. Figure 6.5 shows the vertical viscous forces on the cylinder near then end of this simulation. Clearly the two results are very close. Since any

error in the frequency of the flow are likely to accumulate over the evolution, this suggests that the effect of time-stepping has a negligible effect on the resolved wake frequency.

6.6 Two Dimensional Sphere Wakes

The aim of this section is to compare results for low Reynolds number, two-dimensional sphere flow with previous results. It is known from the literature that the sphere flow is steady and axisymmetric for $Re < 212$. Rather than using an axisymmetric code, fully three-dimensional simulations are performed using the mesh M1 of the next chapter. The main comparison between these results and those of previous works is made by comparing streamlines and wake length of the steady flow.

Streamline Calculation

Two main method are available to calculate the streamlines of a two-dimensional flow. The first approach is to solve a global stream-vorticity equation for the stream function ψ, as used in the previous chapters. Unfortunately, this technique does not scale easily to three-dimensional flows. This method is also more problematic for flow domains that are not simply connected, since cuts need to be made in the domain.

The second method, as used here, involves integrating tracer 'particles' through the flow to form streak-lines. For steady flow these streak-lines are equivalent to streamlines since they are always directed in the flow direction.

The technique used to evaluate the streak-lines is to seed the flow with a number of particles, which are then integrated through the flow domain using a fifth-sixth order Cash-Karp Runge-Kutta (Press et al. (1992)). To evaluate the velocity of each particle at position ($\mathbf{x}$) it is necessary to find the element containing the particle, as well as it's master element position ξ on that element. Using the bounding box of each element, it is possible to exclude most elements from this search. For each element that may possibly contain the particle, the element expansion

$$\mathbf{x} = \sum \mathbf{x}^{ijk} \psi(\xi)^i jk \tag{6.4}$$

is then inverted to find the master element co-ordinate ξ. To invert this relationship, Newton-Raphson iteration is used,

$$\xi = \xi^{last} + \frac{\hat{\mathbf{x}} - \sum \mathbf{x}^{ijk} \psi(\xi)}{\sum \mathbf{x}^{ijk} \frac{\partial \psi(\xi)}{\partial \xi}}. \tag{6.5}$$

If the point $\mathbf{x}$ is not in this element, the value of ξ is seen to quickly escape the master element.

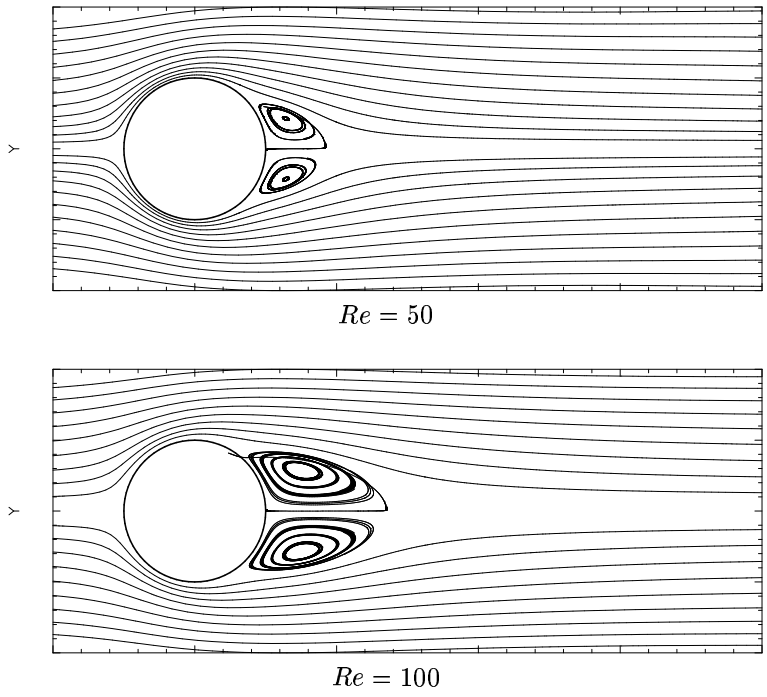

Figure 6.6: Streamlines of axisymmetric sphere flow.

6.6.1 Sphere Flow features

To view the streamlines of the sphere, a line of 31 seed particles are placed on a line between $(-0.65, -1, 0)$ and $(-0.6, 1, 0)$, and integrated both forwards and backwards along the flow lines. Placing the seed particles behind the wake of the sphere allows the wake to be visualized, although it means that speeds cannot be directly computed by viewing the distance between the lines, as is common when viewing contours of the stream-function.

Figure 6.6 shows the streamlines for the two-dimensional flow past a sphere at Reynolds numbers of 50, 100 and 150. The form of the streamlines compares well with those of Johnson and Patel (1999), although without knowing the exact initial positions of the streamlines used in the previous work it is difficult to perform a more direct comparison.

Table 6.6.1 shows the calculated wake length of the current work, compared with that of the previous works of Shirayama (1992) and Tomboulides and Orszag (2000). At a Reynolds number of 50 the wake length is slightly longer than previous results, although still within 5% of the previous results. For the Reynolds number 100 and 150 flows the wake length has a value between the two previous results. In all three of these cases the wake length shows acceptable agreement with the previously calculated results.

Reynolds number	Shirayama (1992)	Tomboulides et al. (2000)	Current
050	0.40569	0.40	0.418
100	0.8103	0.86	0.852
150	1.0803	1.2	1.19

Table 6.1: Wake length for single sphere.

Table 6.2 compares the pressure values for $Re = 50$ and $Re = 100$ with those of Kim and Moin (1984). Since the pressure is only specified at the outer domain, and the domain has been restricted to a square tube in the current work, the final column evaluates the difference between the front and rear pressure on the sphere, as this value is expected to be more independent of the flow domain. Comparing the values of pressure difference with those of Kim shows that the agreement of this figure is to within 0.6% at a Reynolds number of 50 and 1.1% at a Reynolds number of 100. These variations in magnitude are similar to those of Kim's results at differing resolutions, and suggest that the current code generates acceptable values for pressure on the sphere.

Source	Re	Mesh	P_{front}	P_{rear}	ΔP
Kim et al.	50	$N = 30$	0.606	-0.0982	0.7042
Kim et al.	50	$N = 40$	0.604	-0.0954	0.6994
Current	50	C1	0.611	-0.0848	0.6955
Kim et al.	100	$N = 30$	0.555	-0.0819	0.6369
Kim et al.	100	$N = 40$	0.554	-0.0789	0.6339
Current	100	C1	0.567	-0.0737	0.6407

Table 6.2: Axisymmetric sphere flow features.

Figure 6.7 shows flow quantities in the $x - y$ plane for the single sphere flow at $Re = 200$. The top figure, contouring stream-wise velocity, show a substantial area of flow retardation downstream of the sphere. The results is almost perfectly symmetric, other than a slight wobble near the outflow. This anomaly is the result of a drastic and sudden test of the robustness of the numerical technique. The simulation was accidently restarted with corrupted data, resulting in a large region of random pressure in the back part of the wake. While it pleasing to know that the noise was advected downstream without affecting the stability of the scheme, there are still signs of this 'perturbation' near the outflow.

Part (b) of the same figure shows the y velocities on the same plane. Because of the

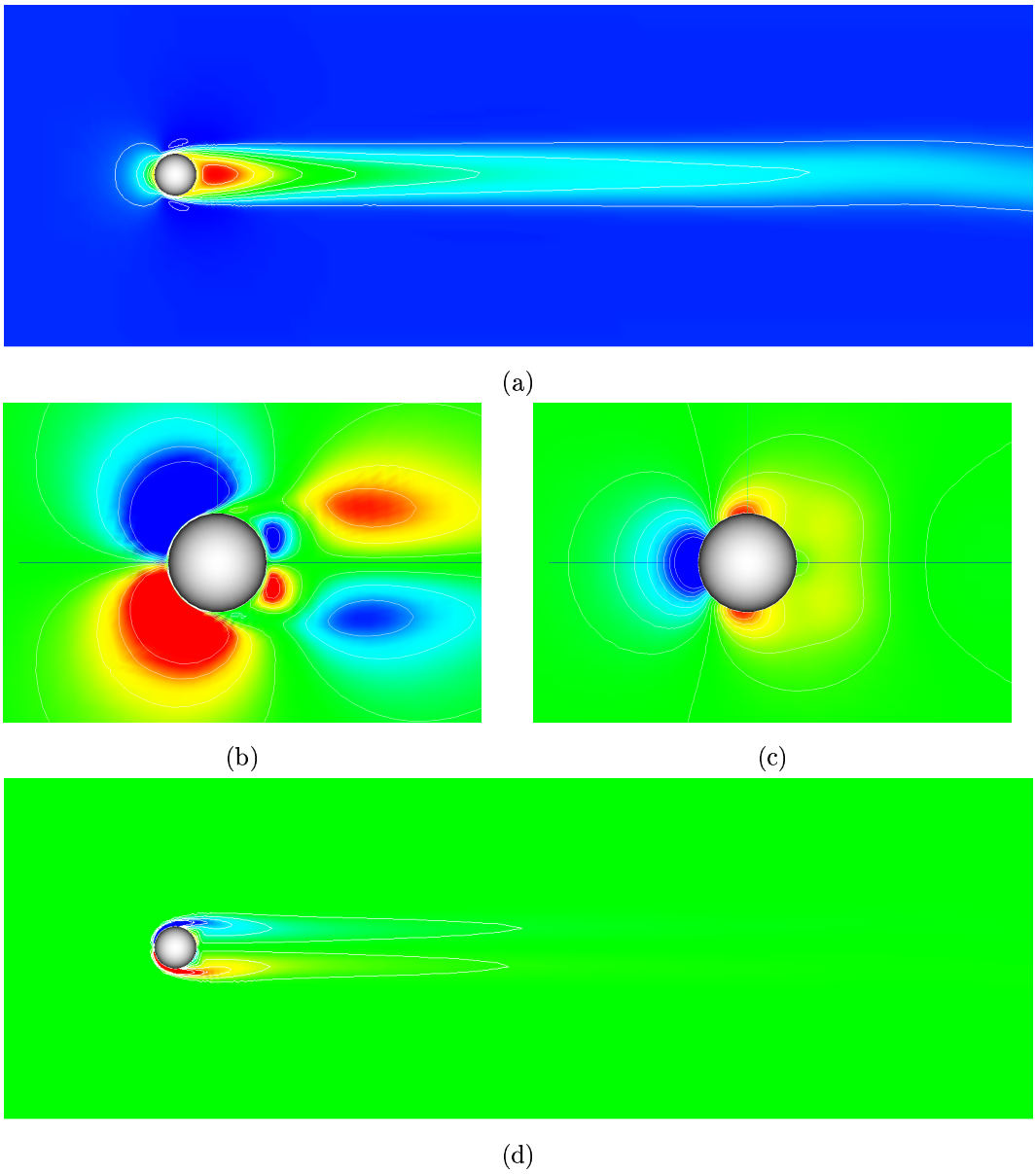

Figure 6.7: Sphere flow features in $x-y$ plane at $Re = 200$, $t = 36.5$.
(a) 10 contours for $-0.35 \leq u_x \leq 1.1$.
(b) 10 contours for $-0.5 \leq u_y \leq 0.5$.
(c) 17 contours for $-0.32 \leq p \leq 0.32$.
(d) 10 contours for $-5 \leq (\nabla \times \mathbf{u})_z \leq 5$.

axisymmetry of the flow, the z velocities are zero on this plane. Since no large variations in the cross-stream velocities exist downstream, the view shown is zoomed in on the sphere. The bounding box of the region is approximately $-2 \leq x \leq -2.5$ and $-1.5 \leq y \leq 1.5$, and again the blue axis extend to $x = -2$ to provide a scale.

Figure 6.7(c) shows the pressure around the sphere. The contour levels used are chosen to allow direct comparison with the pressure results of Johnston and Patel. The shape of the pressure region is well represented, with a loop of low pressure present in the wake. Some jagged contours are evident in these contour plots, and it is worth noting that the plotting, using the VTK library, only uses first order interpolation between nodes, whereas the underlying solution is solved using a much higher order approximation. In particular, many of the asymmetries in the contour lines seem to be from the use of an asymmetric contouring algorithm rather than any underlying asymmetry in the data.

Figure 6.7(d) shows the vorticity in the wake of the sphere at $Re = 200$. Again, a slight asymmetry is present in the results, due to the novel initial condition mentioned previously. Since the flow is axisymmetric, the x component of vorticity is zero, and the choice of coordinates gives the y component a value of zero on the $x - y$ plane.

6.7 Conclusion

This chapter has outlined a series of simulations performed to verify the accuracy of the current numerical implementation. Simulations of shedding cylinder flow were compared with known results to verify that the numerical scheme properly resolves the shedding wake. When allowance is made for blockage around the cylinder, the current results are in good agreement with previous numerical and experimental results. The effects of time step on the wake response were also tested, with use of smaller timestep producing consistent wake frequencies.

Simulations were also performed on flow around a sphere at moderate Reynolds numbers, where the flow was seen to be axisymmetric as expected. Comparisons on streamlines and wake lengths were in agreement with previous results, and closer examination of pressure and other flow variables suggest that the flow features of the axisymmetric wake are being correctly resolved by the current fully three-dimensional simulations.

In the next chapter the Reynolds number of the single sphere flow is increased to simluate sheddding flow around a aingle sphere. As well as providing validation of the current model, this single sphere flow will be used as an initial condition for the interacting sphere flow study.

Chapter 7

Single Sphere Flow

Flow past a single sphere is a good example of a generic compact bluff body flow. Single sphere flow can be very simply specified and yet offers a rich structure of solutions. The flow progresses from, at very low Reynolds numbers, a spherically symmetric flow, to a flow with an axisymmetric wake at increased Reynolds number. As the Reynolds number is increased further, the axisymmetry of the wake is broken, and the a steady three-dimensional flow with a single plane of symmetry develops. As the Reynolds number is further increased, the wake begins to shed, initially with a single frequency and with increasing Reynolds number the flow progresses to a fully turbulent wake.

The aim of this chapter is to simulate the transition of the wake as it moves from an axisymmetric wake to a shedding three-dimensional flow using a fully three-dimensional spectral element technique. These results are compared with existing work on sphere shedding flows. As well as providing a comparison with these works, the current results are used as to form an initial condition for simulation of flow past two spheres.

7.1 Problem Geometry

The model problem of flow past a single sphere is shown in Figure 7.1. The flow is governed by the dimensionless Reynolds number, defined as $Re = Ud/\nu$ for an inlet velocity of U, a sphere diameter of d and fluid kinematic viscosity of ν.

To fix the problem to a finite domain, an outer 'pipe' is added to the flow. In experiments a physical pipe is typically used to enclose the sphere and fluid. In the current work a square pipe is used to enclose the flow. As the goal of the next chapter is to simulate the interaction of multiple sphere wakes, the square pipe is used as an outer boundary condition. This outer

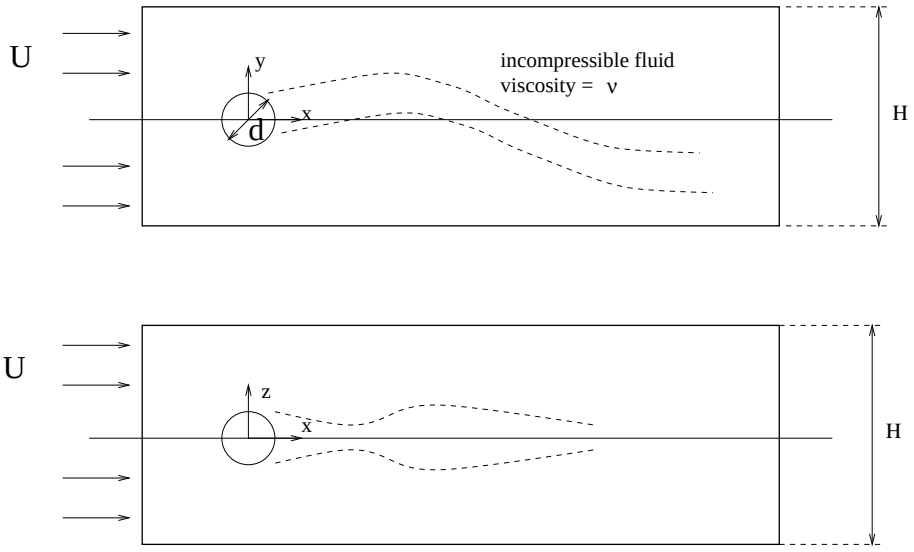

Figure 7.1: Single sphere problem

domain allows for a more convenient fitting together of two single sphere solutions. The width of the outer pipe, denoted here as H, is set to $8d$ in the following simulations. The sphere, being a compact body, is affected significantly less by blockage than the equivalent cylinder wake flow. A value of $H = 8d$ in a square pipe represents a blockage ratio of 1.2%. Using the potential theory argument put forward by Tomboulides and Orszag (2000), this represents a change in the potential flow velocity at the the pipe of less than 0.2%.

As the sphere is axisymmetric, the orientation of the vortex is not predefined. The vortex in Figure 7.1 is shown to indicate the direction used for diagnostics, with the $y = 0$ plane being used as the plane of symmetry. Rotating back onto a symmetry plane gives a convenient reference for quantities such as the planar velocities and vorticity.

7.2 Background

There is a significant body of work on both steady and shedding flow past spheres. The present work considers flow past a sphere over a range of Reynolds numbers as the flow moves from a steady axisymmetric flow toward a fully three-dimensional shedding wake flow. This transition falls in the Reynolds number range between $Re = 200$ and $Re = 300$. Above $Re = 300$ the flow moves towards a turbulent wake flow, and flows with a Reynolds number of greater than 300 are not considered in the current work.

7.2.1 Experimental Results

The initial reported experimental results on flow past a sphere were by Taneda (1956), who reported that a closed recirculation region first forms behind the sphere between $Re = 20$ and $Re = 25$, and that the flow remains axisymmetric up to $Re = 130$. Further experimental investigations by Magarvey and Bishop (1961) and Wu and Faeth (1993) confirm the behavior at the lower Reynolds number, but found that the flow remains axisymmetric until a Reynolds number of at least 210. The results of Nakamura (1976) suggest that the transition from axisymmetric flow occurs at approximately $Re = 200$.

Above a Reynolds number of approximately 210, a so-called double threaded wake is observed. The flow remains steady but no longer axisymmetric. Instead, streak-lines formed by injected dye are seen to form two threads from the back of the sphere that are offset from the centerline.

Provansal and Ormières (1998) performed a series of experiments to determine the critical Reynolds number of the change from a steady non-axisymmetric flow to a shedding flow. This transition was found to occur at $Re_c = 280$. Their investigation also provided a fit of the measured wake frequencies above this Reynolds number. In Ormières and Provansal (1999) the energies of the shedding wake are evaluated, and this is shown to be in good agreement with a Landau-Hopf bifurcation model of transition from steady to shedding flow. This model predicts that above the critical Reynolds number the energy of the wake will grow linearly with respect to the changing Reynolds number; a hypothesis confirmed by the results of Ormières and Provansal.

Another result from the work of Provansal & Ormières is that the direction of the double threaded wake is sensitive to slight changes in upstream geometry; a result seen previously by Sakamoto and Haniu (1995). This sensitivity to geometry is also a factor in numerical simulations. In their experiments four wires were used to hold the sphere in place within the apparatus and these guide wires were observed to 'freeze the spatial mode'.

7.2.2 Axisymmetric Numerical Results

Due to the computational demands of fully three-dimensional simulations, the flow simulations of Fornberg (1988) modeled flow past a sphere by assuming an axisymmetric flow. It was found that the wake length and separation angle vary approximately as $log(Re)$ for $Re > 75$. While steady results are given at higher Reynolds numbers, the restriction to axisymmetric flows means that the results for $Re > 200$ differ substantially from available experimental results.

Kim and Pearlstein (1990) used a steady axisymmetric base solution to perform a linear stability analysis. This work predicted a Hopf bifurcation at approximately $Re = 175$. This figure is significantly lower than that found in previous work (as well as the current results). It is likely that the axisymmetric linear stability analysis does not model the physical transition well, since the wake is know to change from axisymmetric to steady non-axisymmetric before beginning to shed.

Natarajan and Acrivos (2001) also used a axisymmetric base solution to find the transition Reynolds number for the sphere flow. They found that the first transition occurs at $Re = 210$, and is a change of stability from axisymmetric to double threaded. This mode is symmetric about one plane. They found, based on steady axisymmetric flow, a second transition at $Re = 277.5$, a number that compares well with current experimental and three-dimensional flow simulations.

7.2.3 Three Dimensional Numerical Results

Shirayama (1992) examined the transition from axisymmetric wake flow to planar symmetric wake. The study involved the use of a finite difference technique with a maximum grid size of $50 \times 100 \times 50$. This worked considered the sphere flow at a Reynolds number of $Re = 500$, and looked in detail at the startup flow.

Johnson and Patel (1999) compared numerical simulations with experimental results for flow past a sphere. Good agreement was shown between the numerical and experimental results, as well as existing results for the sphere transition flows.

The numerical simulations consisted of a finite difference discretisation with a maximum grid resolution of approximately $100 \times 40 \times 100$ in three dimensions. The vortex visualization method of Jeong and Hussain (1995) was used to examine the vortex behind the sphere at $Re = 250$ and $Re = 300$. Their numerical and experimental results clearly show a hairpin vortex structure in the wake at $Re = 300$.

Tomboulides and Orszag (2000) report a series of comprehensive simulations on flow past a sphere up to a Reynolds number of $Re = 1000$. The numerical technique employed in this work was a mixed spectral element/spectral method scheme. Spectral elements where used in the (r, z) planes, with a spectral method employed in the θ direction. The fractional step method with high order boundary conditions of Karniadakis et al. (1991) was used for temporal discretisation. The geometry used was a circular pipe with a radius of $9d$, giving a blockage of about 1%.

To resolve the flow, 246 spectral elements per plane were used with between sixth and tenth order polynomial approximation being used on each of the spectral elements. For flows

up to $Re = 300$, sixteen planes are used in the θ direction, with this number being doubled for higher Reynolds number flows. In all simulations a timestep of 0.005 was used.

Their work concluded that the flow undergoes a transition from axisymmetric to steady non-axisymmetric at $Re = 212$, and from this state to a single frequency shedding flow at $Re = 270$. By $Re = 500$ the wake exhibited an number of frequencies suggesting that the flow was becoming chaotic.

The aim of this chapter is to resolve the fully three-dimensional wake of flow past a sphere at Reynolds numbers up to 300 using a three-dimensional spectral element technique. These solutions are used as both a validation of the current model, as well as providing a useful initial condition for the more involved interacting sphere problem.

7.3 Mesh

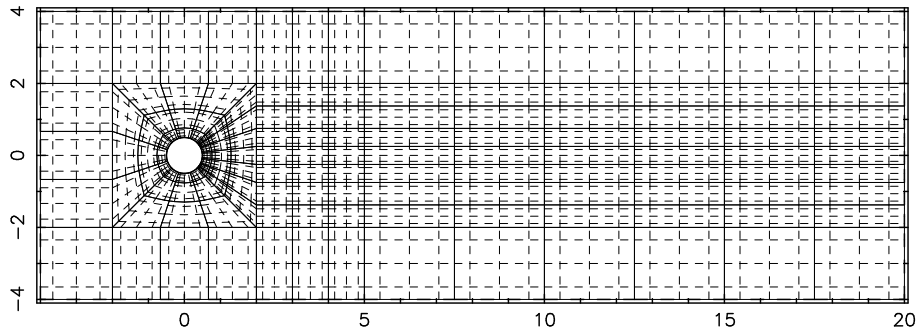

cross-section through $z = 0$

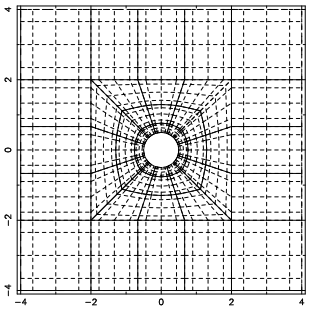

cross-section through $x = 0$

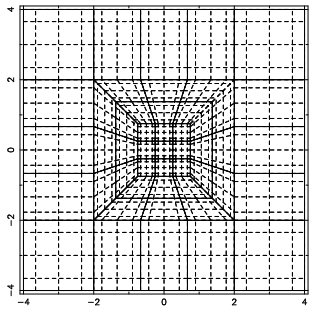

cross-section through $x = 2.75$

Figure 7.2: Single sphere mesh (M1) with order 4 elements

Figure 7.2 shows the layout of elements used for the initial mesh (M1), used to simulate

the single sphere flow. To increase the clarity of the plot, the figure shows the mesh M1 with forth order elements, although seventh order elements are used in the simulations. This mesh has an outer width and height of $8d$ and an upstream length of $4d$, with the wake flow being simulated for a distance of $20d$ downstream. The mesh contains a total of 748 seventh order spectral elements, giving approximately $267,000$ nodal points.

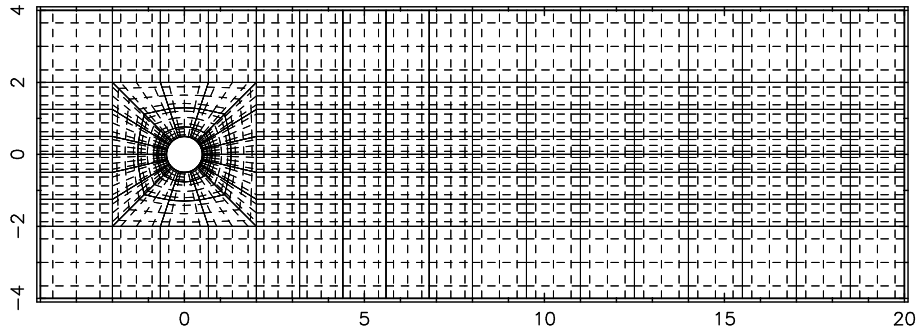

cross-section through $z = 0$

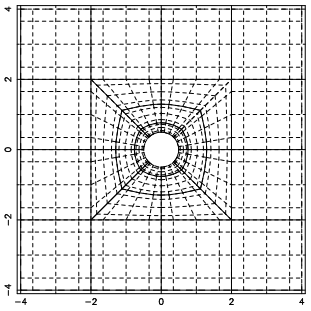

cross-section through $x = 0$

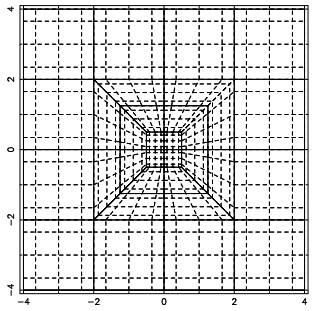

cross-section through $x = 8$

Figure 7.3: Single sphere mesh (M2) with order 4 elements

Some of the higher Reynolds number simulations using M1 showed signs of under-resolution in the vorticity field, and a slightly modified mesh is used to overcome this. Mesh M2, as shown in Figure 7.3 has a slightly modified element layout, as well as using eighth order elements. The mesh consists of 676 eighth order elements with about $360,000$ nodal points. Compared with results from the mesh M1, additional elements were added to the front region of the sphere M2, as well as the concentration of elements in the near wake (up to $x = 5$) being reduced to provide more resolution in the far wake. The far wake showed the most signs of under-resolution when using the mesh M1.

In both meshes, the size of the elements in the wake are kept constant over a range of

x values. This once again allows for the use of memory consolidation by producing many element matrices with the same values. By maintaining only a few different element geometries in the wake it is possible to reduce the total memory requirement of the simulation significantly.

One criteria used to evaluate if the mesh resolution is sufficient is to examine the resultant contours of derivative quantities. In particular, under-resolved spectral element results are known to exhibit jumps in derivative quantities such as the vorticity.

Using the method of Tomboulides and Orszag (2000), the boundary layer resolution of the meshes can be compared to the expect boundary layer thickness. With both meshes, the size of the inner element is $L = 0.21$. Table (7.1) shows the required boundary layer thickness at varying Reynolds numbers, and indicates that the boundary layer resolution of both meshes is expected to be sufficient at the Reynolds numbers under consideration.

Re	δ	L_{req} $p = 7$	L_{req} $p = 8$
100	0.113	0.57	0.80
300	0.065	0.32	0.46
500	0.050	0.25	0.35

Table 7.1: Boundary layer and element thickness. Tomboulides and Orszag (2000)

7.4 Simulation Details

The numerical technique used to simulate the single sphere flow is the spectral element method outlined in Chapter 2. The second order stiffly-stable time stepping scheme of Section 2.4.2 is used along with the corresponding second order pressure boundary conditions of the same section.

The inlet velocity is specified as $\mathbf{u} = (1, 0, 0)$ upstream. This specified velocity is also enforced on the outer pipe. This configuration is equivalent to having the sphere move through a stationary pipe. To reduce the total computation time, the simulation is carried out at increasing Reynolds numbers, with lower Reynolds number simulations used as an initial condition for higher Reynolds number flow.

It is known from experiments and previous numerical work that for Reynolds numbers greater than approximately $Re = 210$, the sphere wake loses axisymmetry, but that the flow maintains a plane of symmetry. This plane of symmetry is somewhat arbitrary; Ormières and

Provansal observed that the orientation could be changed by small changes in the upstream velocity. Since the mesh used in the current work is not axisymmetric, it is expected that this will have some influence on the vortex orientation. To allow for consistent plotting of results, the approach taken here is to evaluate the direction of the forces on the sphere. These are seen to fall on a plane, and this plane is assigned the y axis. This results in the $z = 0$ plane forming an axis of symmetry.

The simulate the flow, the Reynolds number is stepped up by 50, with the lower Reynolds number result being used as an initial condition. At each timestep the steps of the projection method are solved using a GMRES iterative solver with Jacobi preconditioning. The pressure equation (2.45) is solved to a relative tolerance of 10^{-6} with the diffusion equation (2.48) being solved to a tolerance of 10^{-7}. Double precision has been used for all calculations.

The simulations were performed on between 32 and 64 processors of the avalon cluster. The pressure equation solver is the most time consuming part of the simulation with the iteration count taking between 300 and 600 iterations. Clearly an improved preconditioner for the pressure equation is required, and this is an area worthy of further investigation.

7.5 Axi-symmetric flow; $Re = 200$

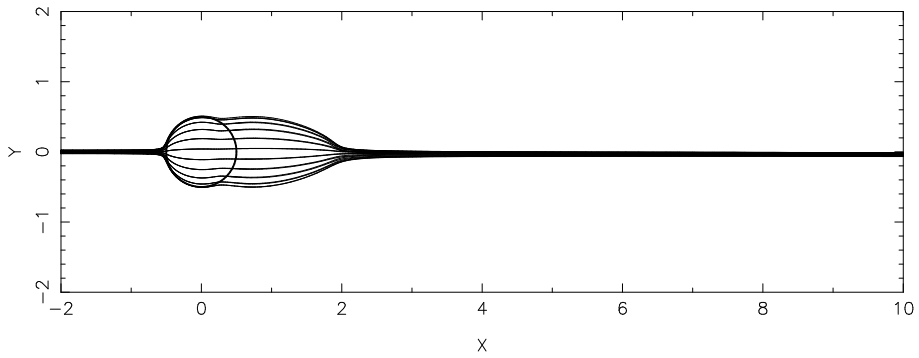

Figure 7.4: Streamlines around sphere at $Re = 200$ $x - y$ plane

After stepping up to a Reynolds number of 200 and allowing the flow to settle down to a steady state, the flow forms a steady, axisymmetric flow with a recirculation are behind the sphere. To visualize the flow around the sphere a streamline trace is shown in Figure 7.4. The streamline trace is generated by seeding the flow with 21 marker particles in a ring of radius 0.025 on the $y-z$ plane at $x = -2$. The particles are then tracked through the velocity field using the particle tracking procedure outlined in Section 6.6.

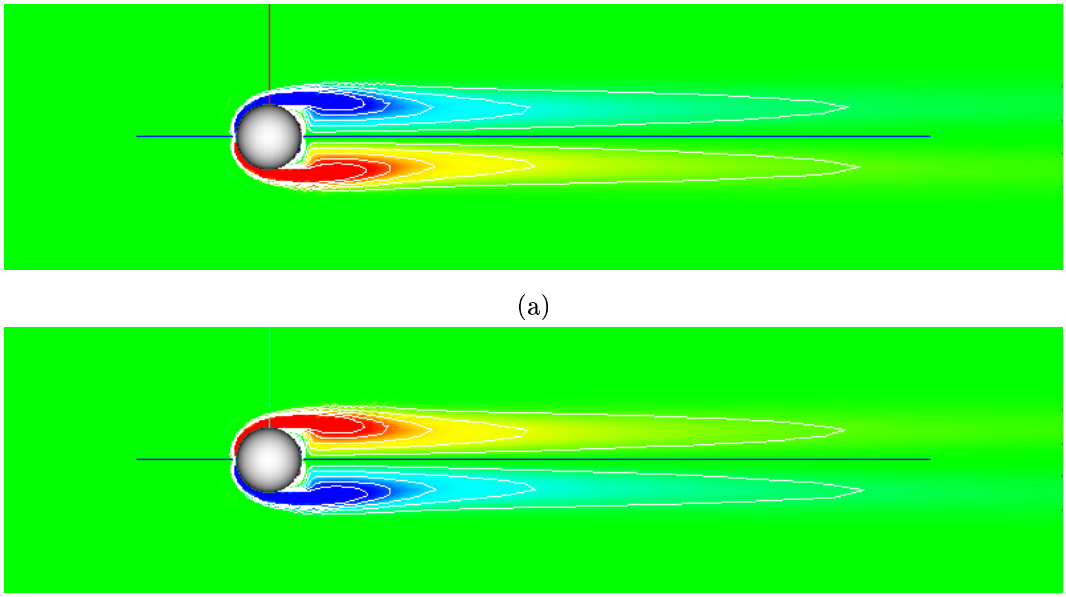

(a)

(b)

Figure 7.5: Vorticity of a single sphere flow at $Re = 200$.
(a) ω_y in $x - z$ plane, (b) ω_z in $x - y$ plane

The y and z components of vorticity are shown in Figure 7.5. Due to the axisymmetric of the flow the x component of vorticity is zero at this Reynolds number. As expected in axisymmetric flow, the vorticity fields are largely axisymmetric. The slight asymmetry in the fields is the result of the use of a corrupted restart file mentioned in the previous chapter.

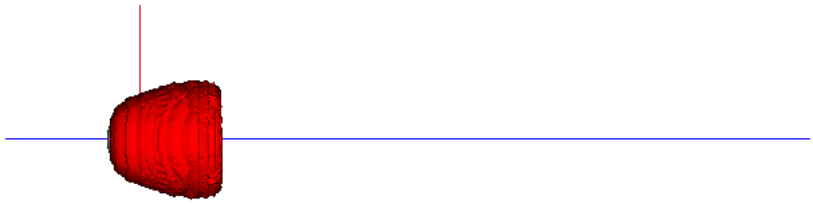

Figure 7.6: Vortex around a single sphere at $Re = 200$. Top view, $x - z$ plane.

Figure 7.6 shows the result of applying the method of Jeong and Hussain (1995) for vortex visualization. The three-dimensional iso-surface is visualized using the VTK graphics library (Schroeder et al. (1998)), and the axes are coloured as green, blue and red for the x, y and z

axis respectively. The positive x axis extends to $x = 10$, all the other axis have a length of 2.

The vortex measure defines the vortex region as those containing negative eigenvalues of the tensor $\mathbf{S}^2 + \mathbf{\Omega}^2$, where $\mathbf{S}$ and $\mathbf{\Omega}$ are the strain and rotation tensors respectively. This measure is based on evaluating derivative quantities with these derivatives being evaluated using the underlying spectral element approximation. Because it is a derivative quantity the vortex measure tends to not be a smooth as the primitive quantities, $\mathbf{u}$ and p, and this is evident in Figure 7.6. This lack of smoothness is not helped by the relatively low order contouring technique being used.

Figure 7.6 shows that at $Re = 200$ the closed recirculation zone gives a small area which can be considered a vortex, and that the rest of the wake is free of anything that could be considered a vortical structure.

7.6 Non-symmetric steady flow; $Re = 250$

To solve for an increased Reynolds number of $Re = 250$, the final solution of the $Re = 200$ is used as an initial condition. This solution is integrated forward in time until a steady state is once again reached. Over the course of this integration the wake changes in character from an axisymmetric flow to a steady flow with planar symmetry.

To give a well defined frame of reference for the wake, the results are rotated back onto the plane of symmetry. To find this plane of symmetry the force on the sphere is found by integrating the viscous and pressure terms over the surface of the sphere, using

$$\mathbf{F} = \int_{sphere} \nu \nabla^2 \mathbf{u} \cdot \mathbf{n} \, ds + \int_{sphere} -\nabla p \cdot \mathbf{n} \, ds \tag{7.1}$$

$$= F_\nu + F_p \tag{7.2}$$

As seen in Figure 7.7, the angle of the force in the steady flow is 39.7°. This figure is used to rotate the solution back for diagnostics. Results presented have been rotated so that the y axis is on the symmetry plane.

By taking the average of the forces on the sphere between $t = 80$ and $t = 100$, the drag coefficient can be calculated. The drag coefficient is defined as

$$C_D = \frac{F_x}{\frac{1}{2}\rho \mathbf{u}_\infty^2 \pi D^2/4} \tag{7.3}$$

which gives, in terms of the non-dimensionalised force f_x and using the current non-dimensional scalings, $C_D = 8f_x/\pi$, and by a similar argument the lift force is $C_L = 8f_y/\pi$. For the $Re = 250$ flow, the drag is $C_D = 0.7076$. Evaluating the $y - z$ plane forces on the sphere gives a lift coefficient of $C_L = 0.06266$, which seems consistent with graphical results pre-

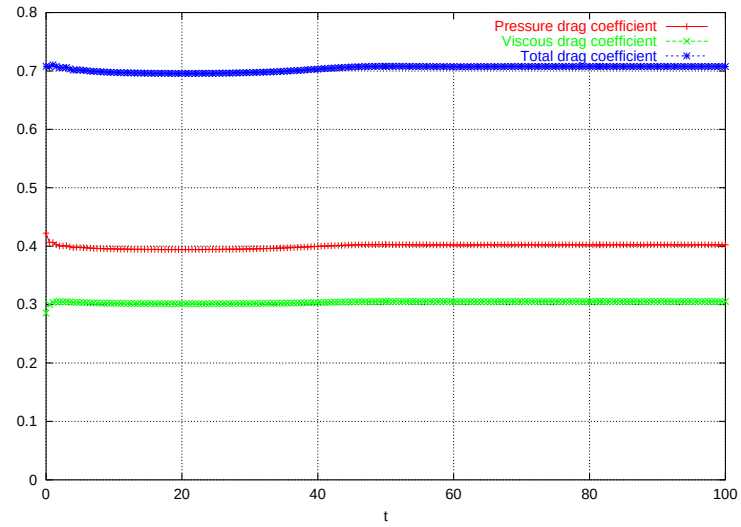

(a) Drag coefficient in axial (x) direction

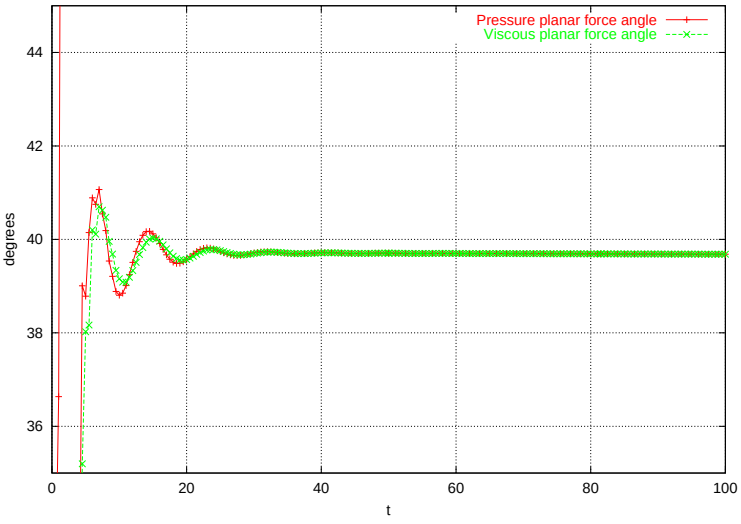

(b) Angle of maximum force in $y - z$ plane

Figure 7.7: Forces on a single sphere at $Re = 250$

sented by Johnson and Patel; analysis of their graph of lateral force coefficient gives a value for C_L in the range 0.061 ± 0.001.

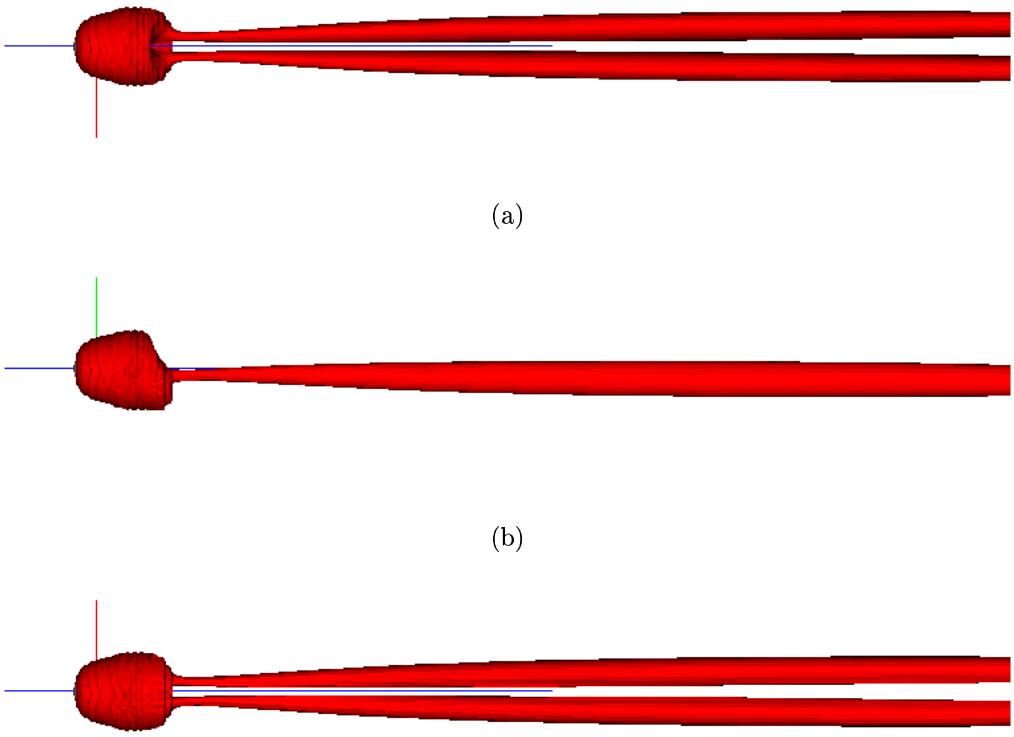

(a)

(b)

(c)

Figure 7.8: Vortex behind a single sphere at $Re = 250$. (a) top view ($x - z$ plane) (b) right view ($x - y$ plane) (c) bottom view

Figure 7.8 shows plots of the vortex core region, as defined by Jeong and Hussain (1995). The results presented here compare well with that of Johnson and Patel (1999) at the corresponding Reynolds number. The results correspond to a time of $t = 100$, where the flow is steady, as seen in Figure 7.7. The angled view of the vortex region in Figure 7.9 clearly shows the 'double threaded' wake of previous results.

Figure 7.10 shows instantaneous streamlines at $t = 100$ for the $Re = 250$ flow, seeded in the same way as the previous section. Since this flow is steady, this is also equivalent to the streaklines or particle paths of the fluid. The particles are seeded in the same manner as

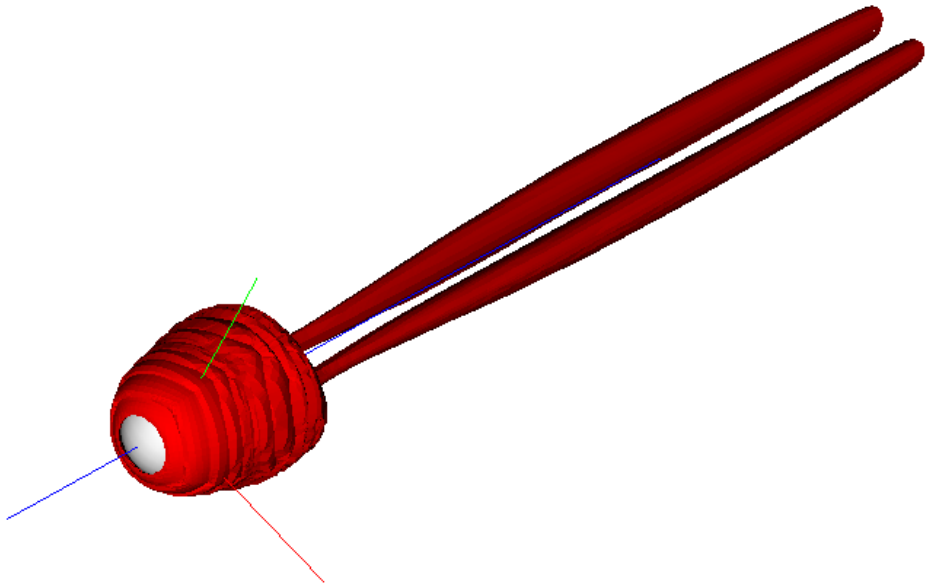

Figure 7.9: Perspective view of vortex behind a single sphere at $Re = 250$

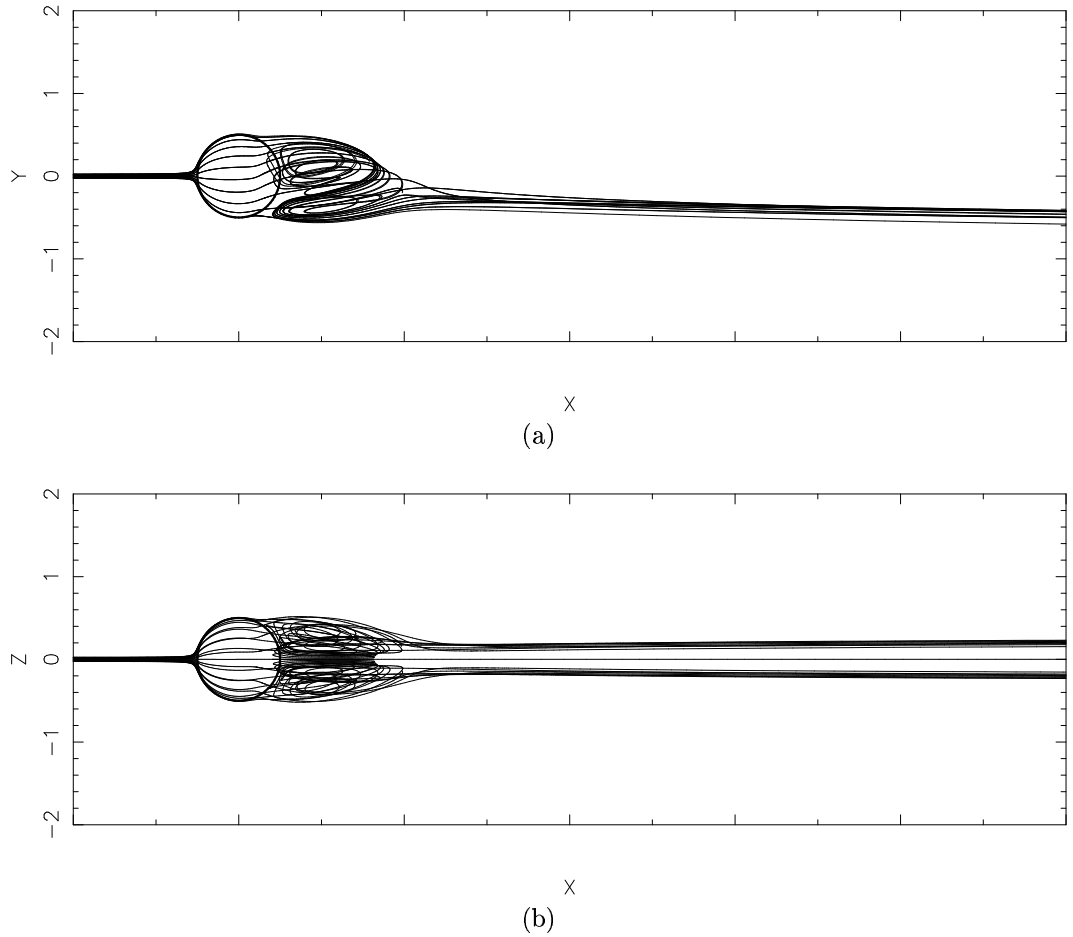

Figure 7.10: Streamlines around a single sphere at $Re = 250$. (a) $x - y$ plane (b) $x - z$ plane

the previous section. The double-threaded wake seen by Ormières and Provansal (1999) and early work is clearly evident in the streamlines of figure 7.10(b).

The vortex structure behind the sphere is in good agreement with Johnson and Patel (1999), where a larger recirculation zone at the 'top' of the sphere feeds into a smaller recirculation zone at the bottom which then leaks out into the main flow. This causes the wake of the sphere to be off-center of the $y = 0$ plane. The top view indicates that the fluid leaves the rear recirculation at a location below the $z = 0$ plane, and that this takes place at points symmetric about the $y = 0$ axis. This leads to the double wake formation observed in experiments. [note: in Johnson and Patel's work, their largest vortex appears at the bottom of the sphere, due to a different choice of co-ordinate systems. Since this choice is arbitrary, the results are equivalent.]

Figure 7.11 shows vorticity cross-sections of the steady non-symmetric flow. In (a), the vorticity contours are between $\omega_x = -0.5$ and $\omega_x = +0.5$ at intervals of 0.1. Figures (b) and (c) have a range of $-2.5 \leq \omega_y, \omega_z \leq 2.5$ with an interval of 0.5. In all cases blue represents positive values and red represents the most negative. The current vorticity results compare well with those of Johnson and Patel. The contours of ω_z show some mesh related noise upstream of the sphere; a refined mesh has been used at $Re = 300$.

7.7 Shedding flow; $Re = 300$

As the Reynolds number is increased from 250 to 300, the flow changes from a non-axisymmetric steady flow to a shedding flow with one dominant frequency.

To speed up the onset of shedding, the initial condition used for the $Re = 300$ flow is the $Re = 250$ solution with a 1% random noise applied to the velocity field. Figure 7.13 shows flow quantities over the time period $t = 5$ to $t = 100$ at two points in the flow.

By evaluating the average of the forces on the sphere over the time period $40 \leq t \leq 157$, the average lift and drag are determined. The average lift coefficient of $C_L = 0.0687$ is within the accuracy of the figure given by Johnson and Patel. The average drag coefficient of $C_D = 0.662$ falls between the values given by Johnson and Patel, with $C_D = 0.656$, and the result of Tomboulides and Orzag of $C_D = 0.6714$.

The principal frequency of the wake (which is the Strouhal number of equation (6.1)) for $t > 40$ is 0.136 ± 0.0085. Selection of this time range is based on examination of Figure 7.14, since for $t > 40$ the flow seems to have reached periodicity. This Strouhal frequency gives a wake period of 7.35. The error estimate for the Strouhal number is a results of the Fourier transformation, and is determined by the length of the integration time, as outline in the previous chapter. The Roshko number, $Ro = St \times Re$, of the current result for $Re = 300$

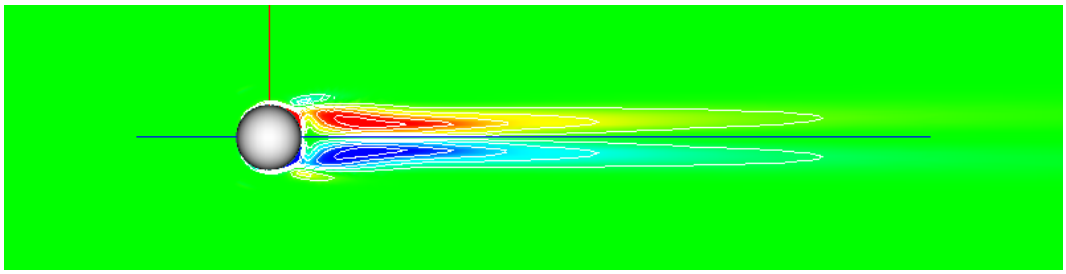

(a)

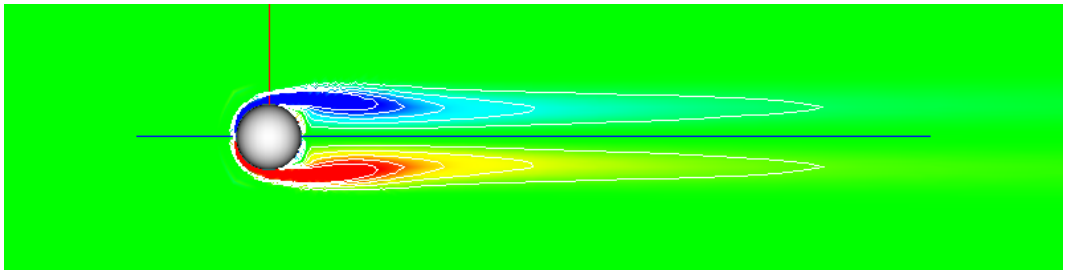

(b)

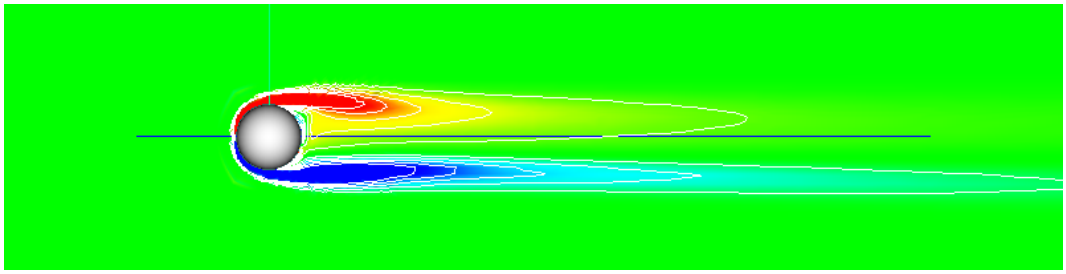

(c)

Figure 7.11: Vorticity cross-sections for single sphere flow at $Re = 250$. (a) ω_x in $x-z$ plane, (b) ω_y in $x-z$ plane, (c) ω_z in $x-y$ plane

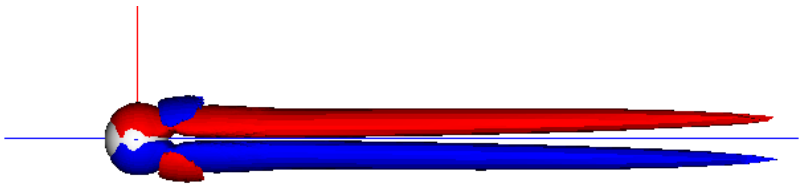

(a)

(b)

Figure 7.12: Axial vorticity volumes for single sphere flow at $Re = 250$. (a) ω_x, view of $x-y$ plane, (b) ω_x, view of $x-z$ plane

gives $Ro = 40.8 \pm 2.6$. This results is slightly larger than the value predicted by Ormières and Provansal (1999) where the curve fit gives a value of $Re = 36.7$.

In Figure 7.14(c), the angle of the maximum force is plotted. For later integration times, the angle of the force is very close to constant. The jump in the angle of the force that is apparent near $t = 35$ corresponds to the change in character of the wake from essentially steady and axisymmetric to a time dependant shedding wake. In plotting field results, and angle of 41.5° is used to move the y axis back to the axis of symmetry.

7.7.1 Flow Quantities

While the Strouhal number and general flow features using the mesh M1 correspond well with previous work, some noise was present in the iso-surfaces of vorticity and vortex measure. To improve the quality of these results, the higher order mesh, Mesh M2, was used to simulate the $Re = 300$ flow. To avoid having to restart the flow, the solution from the M1 mesh is interpolated onto the M2 mesh using the natural spectral element (GLL) interpolating functions. While producing slightly more acceptable derivative quantities (vortex measure and vorticity) in the far wake and upstream of the sphere, the main flow features, including the Strouhal number, drag coefficient, and lift coefficient are effectively unchanged. The

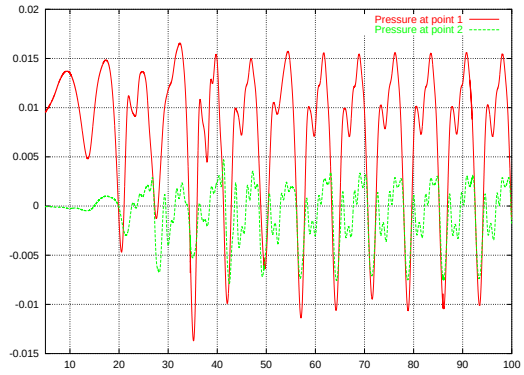

(a)

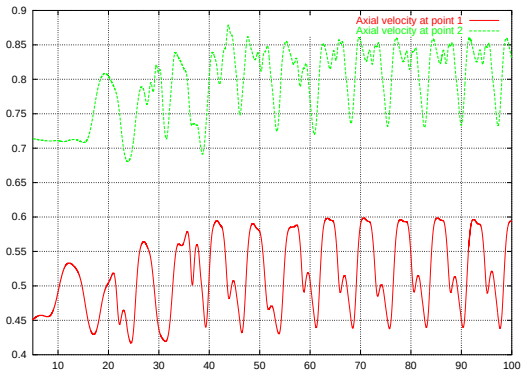

(b)

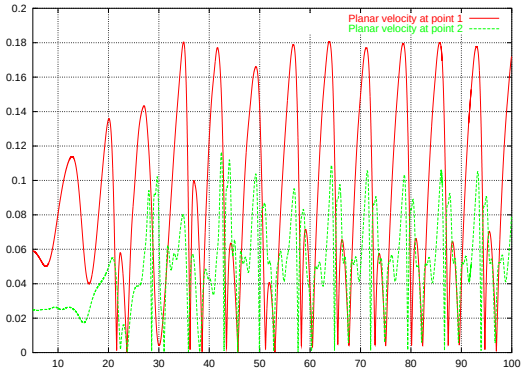

(c)

Figure 7.13: Point values in wake of single sphere flow at $Re = 300$. Point 1 = $(4, -0.052, -0.052)$, Point 2 = $(10, -0.052, -0.052)$. (a) Pressure values. (b) Axial velocity values. (c) Magnitude of planar velocities

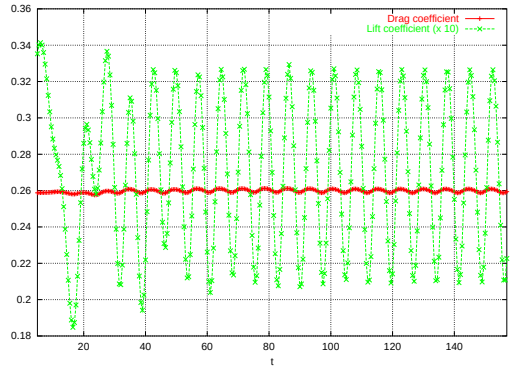

(a) Forces in x direction

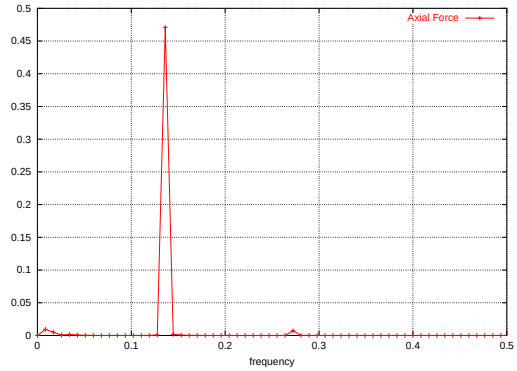

(b) Spectrum of force in x direction for $40 \leq t \leq 147$

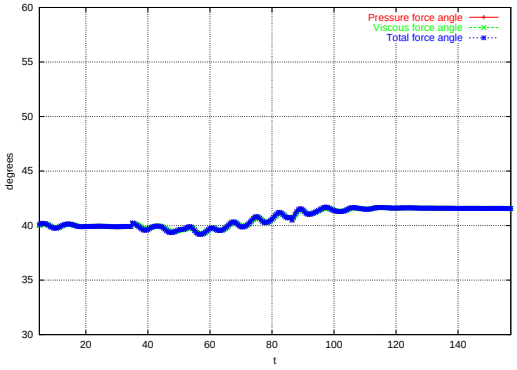

(c) Angle of maximum force in $y - z$ plane

Figure 7.14: Forces on single sphere at $Re = 300$

simulation time is reset, so results for the M2 mesh refer to the time t from interpolating the M1 result onto the new mesh.

Figure 7.15 shows the axial velocity over approximately one periodic cycle of the flow. The difference in t of 7.5 between the first and last frame is slightly longer than calculated period of 7.35, but the matching between the first and final frame is reasonably close. The light blue tube in Figure 7.15 shows the area of wake retardation in the flow, and shows the hairpin structure present in the wake. As the wake is carried in the flow, the wake diffuses, leading to the apparent 'breaking off' of the wake. The actual location of this phenomenon is dependant on the choice of contour level, and in practice the speeding up of the wake is gradual.

7.7.2 Flow Vortex and Vorticity

Figures 7.16, 7.17 and 7.17 show calculations of Jeong and Hussain's vortex measure from the top, side and from a perspective view. When compared with Figure 7.8 they show clearly the change in structure from the double wake to a shedding hairpin wake. There is some noise present in the shedding vortex results; a resolution effect which is exaggerated by the use of derivatives in the vortex measure. Contouring through zero also increases the noise present in the vortex contours.

Figures 7.19 and 7.20 show the stream-wise (ω_x) vorticity. As the vorticity convects down stream, the bottom vortex folds in on itself.

Figure 7.21 shows the ω_z vorticity. The asymmetry in this vorticity, with the positive vorticity on the bottom being stronger, causes the stream-wise vorticity to continue to fold up as is convects downstream.

7.7.3 Instantaneous Streamlines

To obtain a picture of the flow, instantaneous streamlines are calculated by integrating seed particles through the flow at given times. The seed particles are coloured by their initial position, with circles of 8 particles placed at $x = -2$ on the axis, and at the four points $x = -2, y = \pm 0.25, z = \pm 0.25$. The results of this tracing technique do not generate streak-lines, as would be seen if dye were injected into the flow and integrated with the fluid velocity over time, rather they produce lines in the direction of the instantaneous flow field.

Figures 7.22 And 7.23 show the instantaneous streamlines from the side and top respectively over one cycle of the shedding. Notice that the hairpin vortices seen in Figure 7.18, and also suggested by Figure 7.15, are not apparent in the instantaneous streamlines. The z component of vorticity in Figure 7.21, which measures vortex rolling motion in the direction

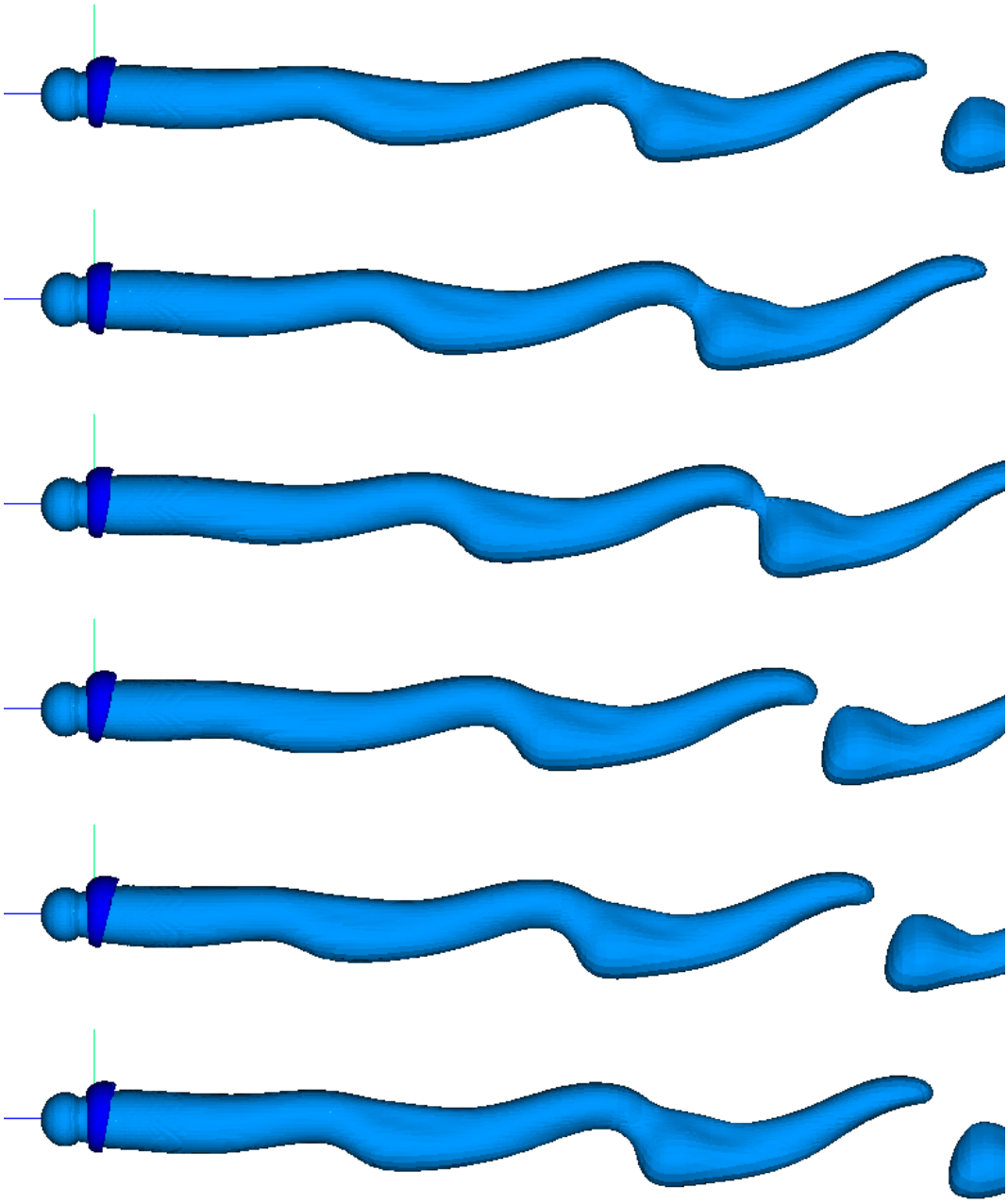

Figure 7.15: Axial velocity, u_x, in wake of sphere, $Re = 300$. Side view. Mesh M2. Times are, from top to bottom, $t = 12.5$, 14, 15.5, 17, 18.5 and 20. Darkest blue contour is $u_x = 1.1$, light blue contour is $u_x = 0.9$.

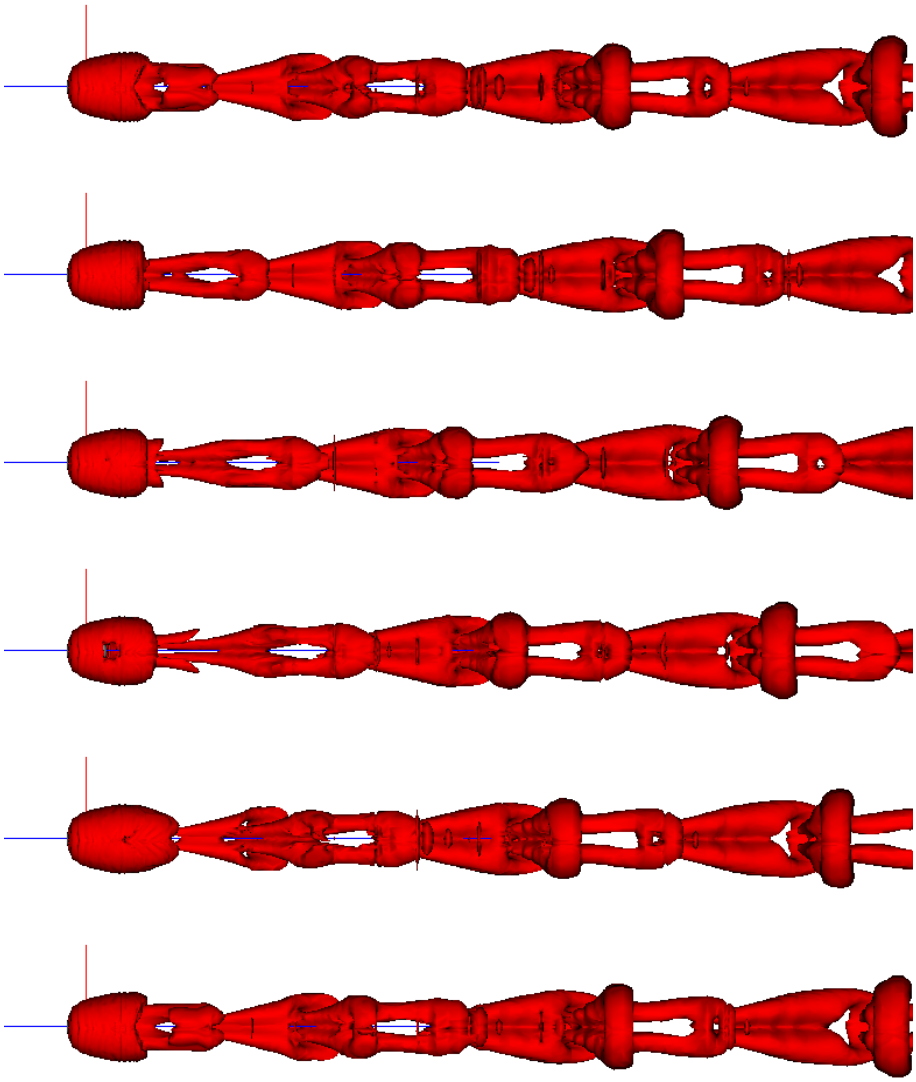

Figure 7.16: Vortex wake of sphere, $Re = 300$. Top view. Mesh M2. Times are, from top to bottom, $t = 12.5$, 14, 15.5, 17, 18.5 and 20.

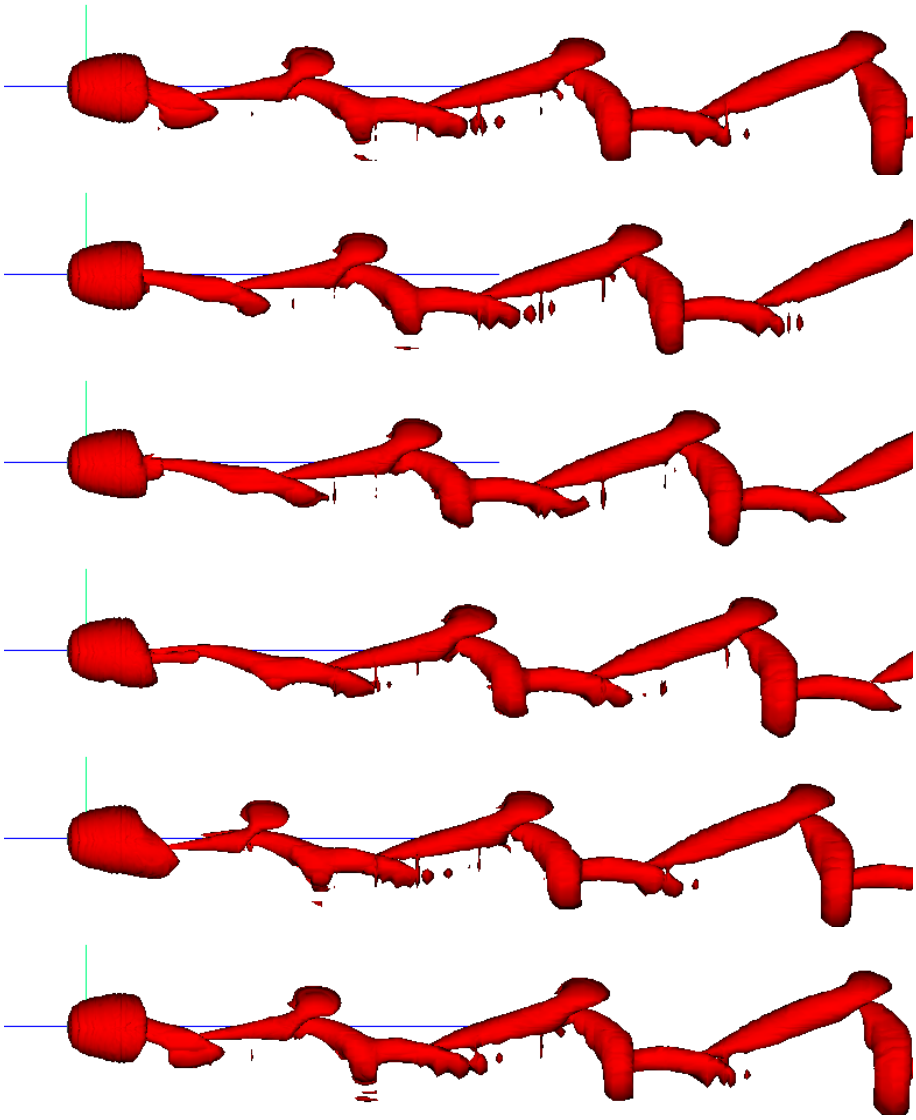

Figure 7.17: Vortex wake of sphere, $Re = 300$. Side view. Mesh M2. Times are, from top to bottom, $t = 12.5$, 14, 15.5, 17, 18.5 and 20.

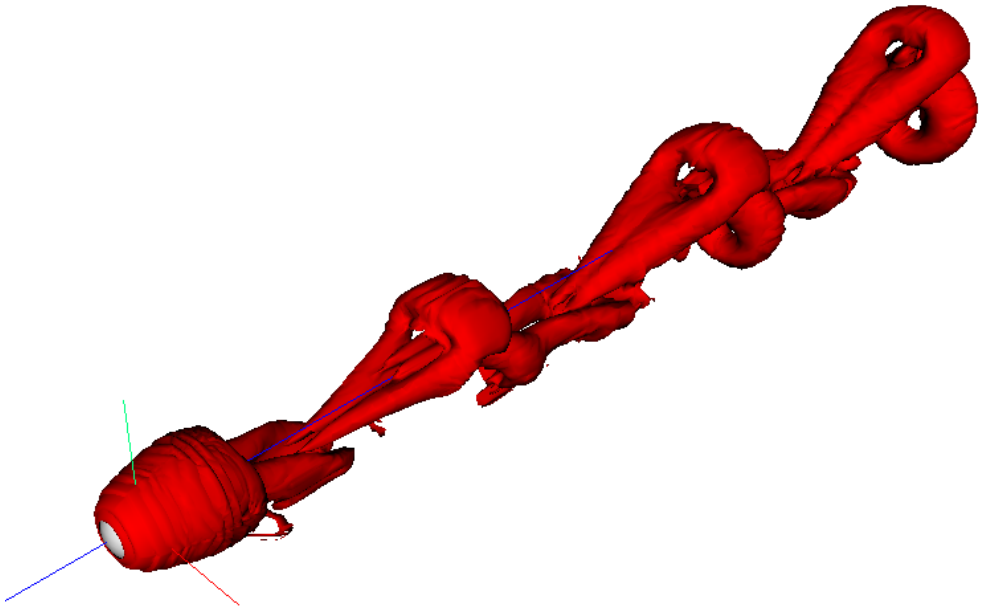

Figure 7.18: Perspective view of vortex behind Sphere at $Re = 300$

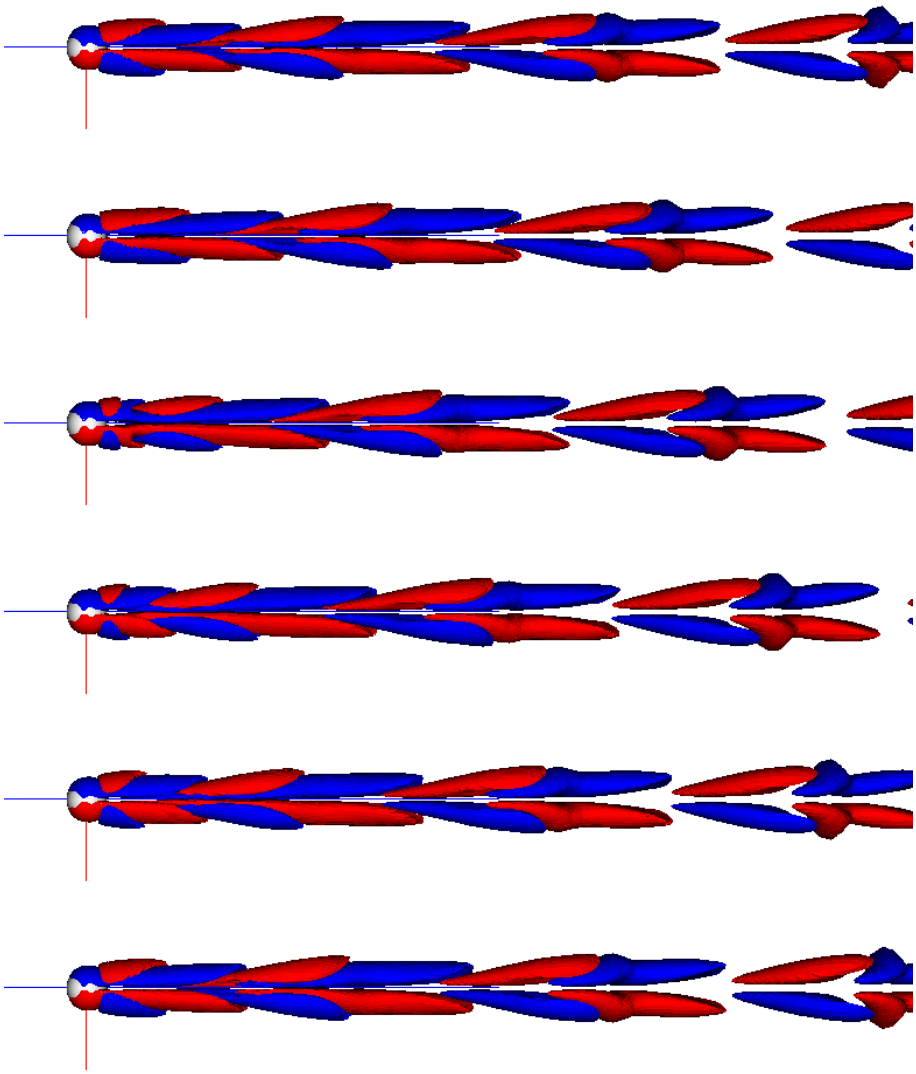

Figure 7.19: Axial vorticity in wake of sphere, $Re = 300$. Top view. Mesh M2. Blue contour is $(\nabla \times \mathbf{u})_x = 0.1$, Red contour is $(\nabla \times \mathbf{u})_x = -0.1$, Times are, from top to bottom, $t = 12.5$, 14, 15.5, 17, 18.5 and 20.

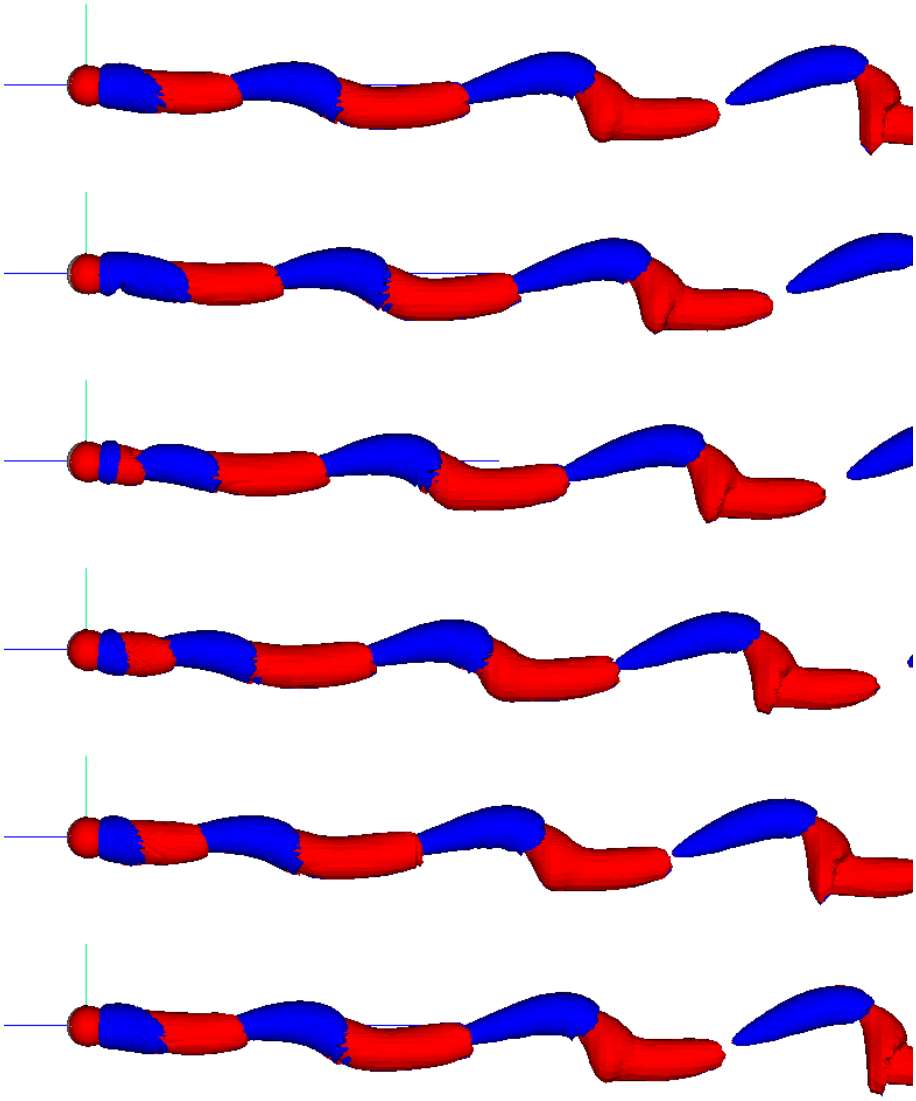

Figure 7.20: Axial vorticity in wake of sphere, $Re = 300$. Side view. Mesh M2. Blue contour is $(\nabla \times \mathbf{u})_x = 0.1$, Red contour is $(\nabla \times \mathbf{u})_x = -0.1$, Times are, from top to bottom, $t = 12.5$, 14, 15.5, 17, 18.5 and 20.

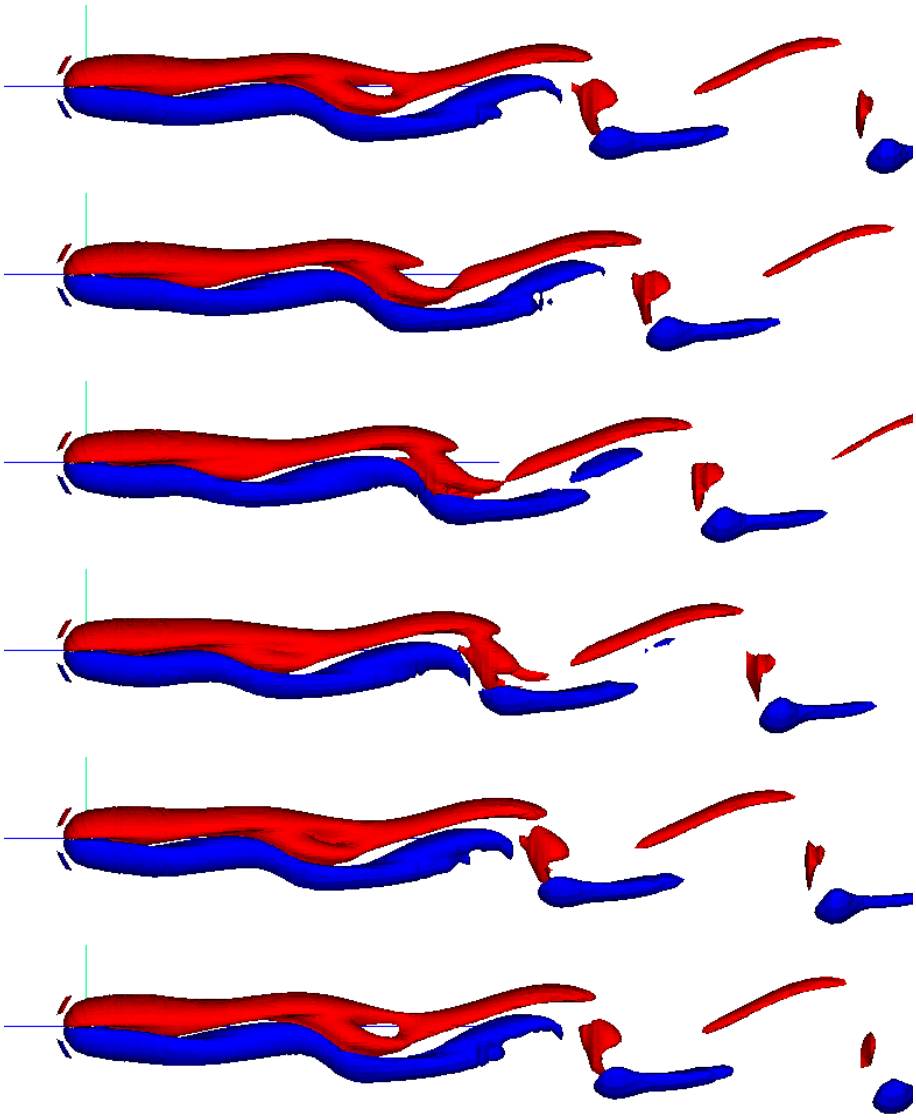

Figure 7.21: ω_z vorticity in wake of sphere, $Re = 300$. Side view. Mesh M2. Times are, from top to bottom, $t = 12.5$, 14, 15.5, 17, 18.5 and 20.

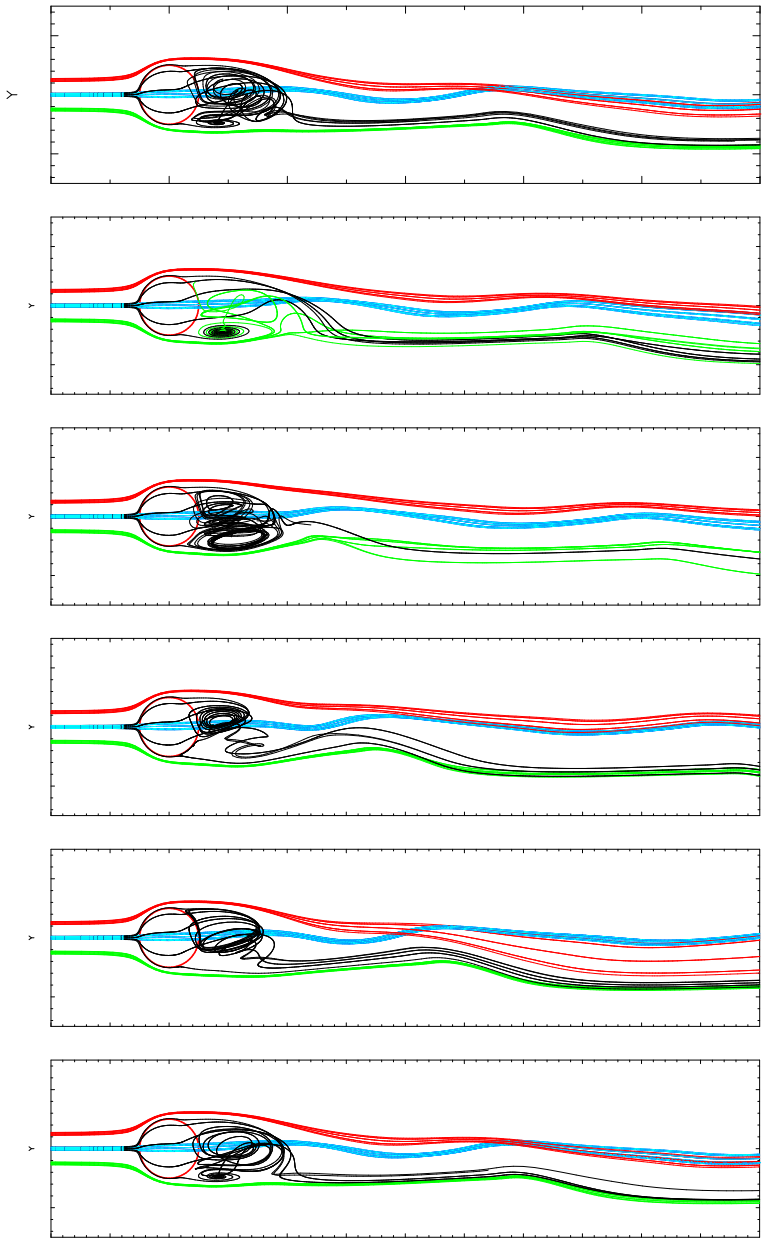

Figure 7.22: Streamlines in wake of sphere, $Re = 300$ side view. Mesh M2. Times are, from top to bottom, $t = 12.5$, 14, 15.5, 17, 18.5 and 20.

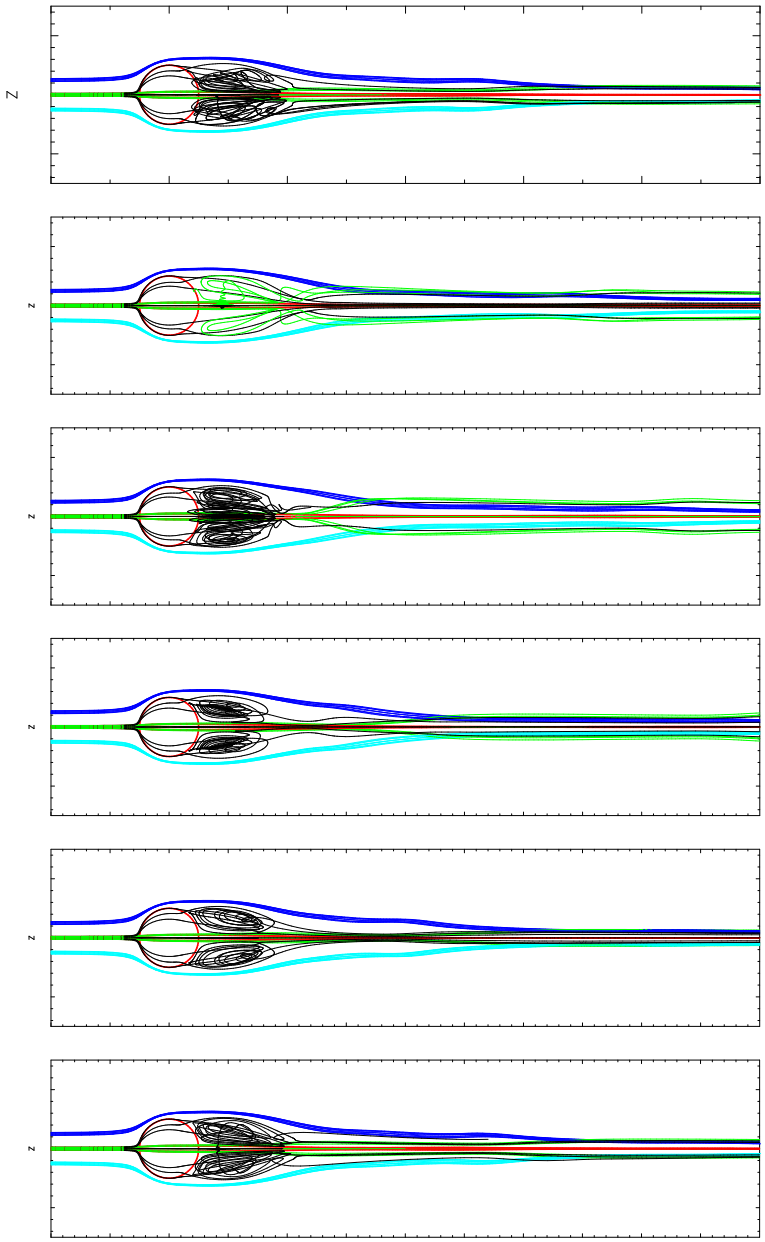

Figure 7.23: Streamlines in wake of sphere, $Re = 300$. Top view. Mesh M2. Times are, from top to bottom, $t = 12.5$, 14, 15.5, 17, 18.5 and 20.

of the flow, shows that more that about five diameter lengths downstream of the sphere a significant amount of the negative (on top) vorticity has defused. This indicates that the top part of the vortex structure is formed largely at the sphere and convects downstream with the flow. On the other hand, the lower vorticity, rotating in a counter-clockwise sense, is still relatively large downstream, and accounts for the increasing kink in the streamlines downstream of the object.

7.8 Conclusion

The current chapter outlines a series of simulations of flow past a single sphere as it transitions from an axisymmetric wake flow to a shedding wake flow. The fully three-dimensional spectral element code does a good job of resolving the wake, and provides good agreement with previous experimental and numerical work. In particular, the shedding wake flow at $Re = 300$ shows good agreement, showing a wake shedding at a single frequency and shedding in a symmetrical pattern around one plane only.

The aim of the next chapter is to use the single sphere simulation as an initial condition to study the interaction of the wakes behind two spheres.

Chapter 8

Double Sphere Flow

Interaction of the wake flow behind two spheres can be seen as a prototype for interaction of more general compact bluff-body flows, as well as an intermediate step to understanding the interaction of many body systems. The interaction of particles in fluid area of relevance to many areas of industrial and geo-physical fluid dynamics. Studies of air pollution, combustion and chemical mixing processes all depend on interaction of particles. Physical processes such as sedimentation also depend on the interaction of solid particles within fluids.

While the multiple sphere configurations offers many possible areas of investigation, the resources required to study all sphere combinations is prohibitive. The flow currently consideration consists of two spheres separated by a distance S placed perpendicular to the flow direction. The Reynolds number considered is $Re = 300$, a value which has been seen cause a relative simple shedding mode in flow around a single sphere.

Figure 8.1 gives a schematic of the flow domain to be studied, with an indication of the general direction of the flow wake. The free parameters of this problem are the dimensionless Reynolds number, again defined as $Re = Ud/\nu$, and the dimensionless sphere separation S/d. The domain height H (in the y direction) is kept constant at $H = 8d$. The domain width is increased in the z direction as the separation is increased, keeping the spheres a constant distance from the outer walls. The total domain width in the z direction is therefore $(H+S)d$.

8.1 Background

8.1.1 Numerical work

Previous numerical work in sphere interaction has been limited to lower Reynolds number flows, where the wake has been seen to be steady. (Thau) et al. (1983) studied the hydrody-

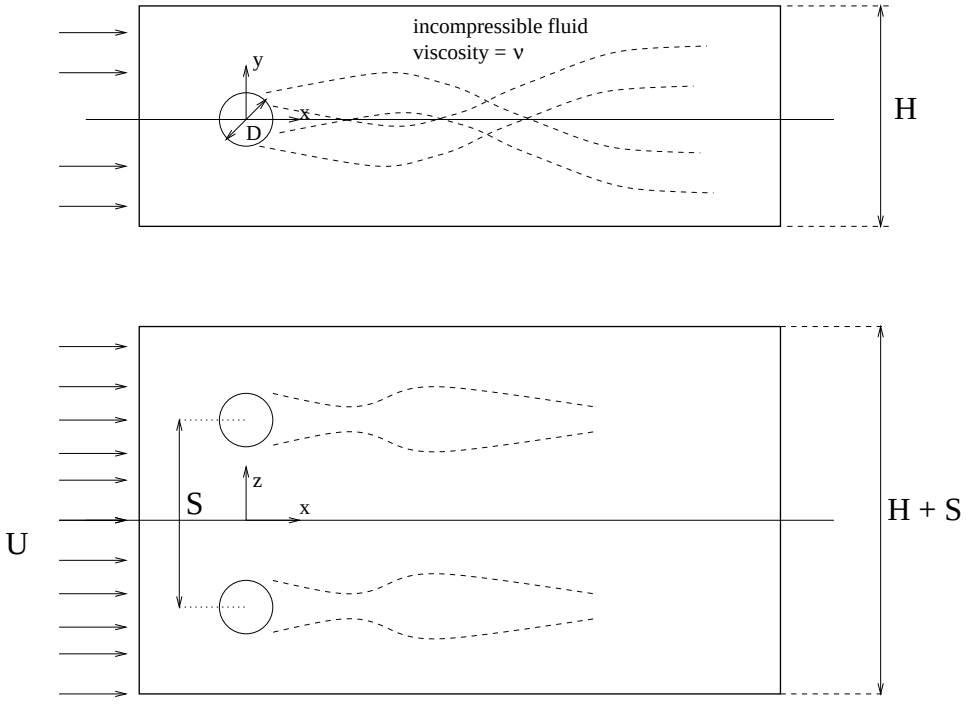

Figure 8.1: Two sphere problem

S/d	order	number of elements	number of nodes (approx)
1.5	7	1240	442,000
2.5	7	1764	626,000
3.5	7	1764	626,000

namics and heat transfer of assemblages of solid sphere in a steady flow at $Re = 100$. This flow was examined by using the periodicity of the problem geometry. It was found that the interaction of the spheres acted to reduce the stream-wise drag on the spheres.

In (Thau) et al. (1984) the hydrodynamics and heat transfer of pairs of solid spheres paired downstream in steady flow at $Re = 40$ are examined. Again, the multiple spheres in this orientation was seen to cause a reduction in drag compared with the single sphere case.

The fully three-dimensional simulations of Kim et al. (1993) studied the interaction of two solid or liquid spheres at $Re = 50, 100, 150$. Some of the key findings of this work include the observation that the recirculation near the axis of symmetry are reduced, and then finally stopped as two spheres are moved closer together. For intermediate values of separations, the $S/d < 4$ cases that are currently being considered, the spheres repulse each other as the pressure between the two spheres in increased. It was also observed that the separation required to give zero repulsive force reduces with increasing Reynolds number.

The central eddies of the sphere flow are seen to detach from the sphere and entrain fluid from the outer eddies. At $S/d = 1.5$, the inner circulation zones are not present although a (non-recirculating) reverse flow region is present. Due to the use of a symmetry boundary condition, the simulations of Kim et al. are not capable of simulating the shedding wakes considered in the current work, although for the Reynolds numbers used in their work the symmetry condition is appropriate.

The aim of the current work is extend these previous results into the range of Reynolds numbers which is known to shed in the case of single sphere flow.

8.2 Computational Mesh

The meshes used to simulate interacting spheres are an extension of those used for the single sphere flow. For sphere with a separation of S/d, the flow domain has a height of $8d$, and a width of $8d+S$. The flow domain extends $4d$ upstream, and a flow domain of $20d$ downstream is simulated. The outer area of the flow is modeled with zero normal velocity gradients and zero pressure. The outflow boundary condition enforces zero stress.

The meshes sizes used are shown in Table 8.2. The structure of the mesh is similar to that

used in the previous section, with the two mesh structures being joined along the centerline $z = 0$. As the separation of the spheres is increased, extra elements are added between the spheres to allow for the increased domain size.

8.3 Simulation Details

In the following simulations the Reynolds number has been fixed at $Re = 300$, which corresponds to the simple shedding flow in the one sphere flow of the previous chapter. The flow is then examined at a several sphere separations, S. The flows considered here are $S/d = 1.5, 2.5$ and 3.5. Another flow of interest is flow around touching spheres, corresponding to $S/d = 1$. Unfortunately, the current method of mesh generation, involving manual specification of blocks in the domain, does not deal well with the geometrical singularity of such a flow.

Solving the spectral element method in three dimensions is a formidable numerical task, even with the use of parallel computing. The desire to simulate the sphere flow at a number of separations compounds this problem. To partially overcome this limitation the initial condition for the two sphere flow is interpolated from the single sphere flow at a Reynolds number of 300. This flow is shedding with a somewhat arbitrary orientation to the axis. As well as introducing a velocity jump at the symmetry line, this initial condition introduces an asymmetry in the y direction into the flow. In spite of these problems, it does offer significant saving in computation time.

The other technique used to reduce the total execution time was to allow the flow to 'settle down' using a mesh of reduced order, in this case order 5 versions of the meshes indicated in Table 8.2. While this reduction in resolution is far from ideal, it does significantly reduce the total execution time of the simulations. These low order solutions are then used to restart the simulations at a higher resolutions.

All other details of the simulation are essentially unaltered from the techniques of the previous chapter. Since the placing of the spheres side-by-side gives orientation to the flow, there is no longer a need to rotate results onto a plane of symmetry.

8.4 Forces on Spheres

In this section the forces on the two spheres as they are accelerated from their interpolated initial condition are investigated. The results are based on the fifth order simulations, and hence are likely to be less accurate than desirable. However, it is encouraging to see that once the flows are restarted at a higher resolution, the wake shedding pattern in maintained.

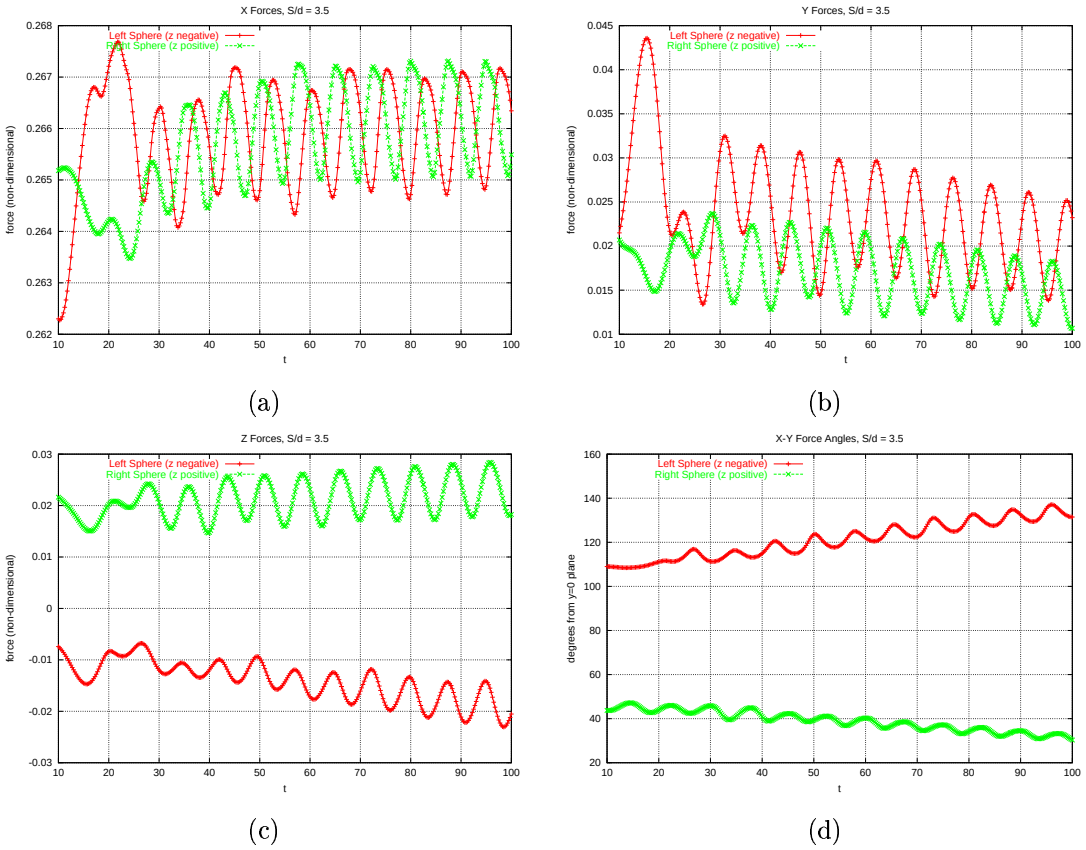

Figure 8.2: Forces on two spheres, $S/d = 3.5$.
(a) axial forces, x direction. (b) sideways forces, y direction. (c) up/down forces, z direction.
(d) angle of force in $y - z$ plane.

Figure 8.2 shows forces on the two spheres over time as the wake develops. As well as the drag force and lift forces, the angle of the 'lift' force from the $z = 0$ plane is also plotted. These results indicated that, even after evolving up to $t = 100$, the direction of the flow force has yet reach a constant. The wake direction seems to be slowly progressing towards the plane, although it's final orientation is far from certain. From this it can be gathered that at a separation of $3.5d$, the two sphere wakes act largely independently. While the presence of the adjoining sphere may be causing some change in the orientation of the wake, it is at most only similar in magnitude to the forces exerted by the square geometry of the outer walls.

It is worth noting that, as with the single sphere flow, the total lift force is significantly smaller than the drag force on the sphere, in this case of order 100 times smaller. The alignment of the wakes is different on each sphere, although this is perhaps not surprising since the initial condition was not symmetric. Of more interest is the offset in time of force graphs, with the right sphere (when viewed from the front, that is, $z > 0$) reaching a peak in force approximately a third of a cycle before the left sphere. The flow has a period of 7.6, corresponding to a Strouhal frequency of 0.13. This period is longer than that seen in the single sphere flow.

In Figure 8.3 the forces on the two spheres at a separation of $S = 2.5d$ are shown. At this separation the flow has settled down into a basically planar flow pattern by $t = 100$. The forces in the y direction are an order of magnitude smaller than those in the z direction, with the drag force (the x direction) being an order of magnitude larger again. The forces on each sphere are different, although the difference is less than 1%, and is quite likely due to resolution effects. Again the forces on the spheres are slightly out of phase, although the occurrence of maximum force is closer than at the greater separation.

With a separation of $S = 2.5$, the period of the flow is approximately 7.0, corresponding to a Strouhal frequency of 0.14. This frequency is larger than that observed in the single sphere flow. It is known that as the Reynolds number increases in the single sphere flow, the Strouhal frequency increases. A likely explanation for the increase in this case is that the two spheres begin to act more like a single larger object, increasing the effective Reynolds number of the flow by increasing the length scale.

For the forces on spheres with a separation of $1.5d$, Figure 8.4 gives a different picture. Again, the forces in the z direction are significantly smaller, and it is seen that the flow moves to a nearly planar flow much more quickly than the previous flow. Again, the forces on the spheres are out of phase, but in this case the two spheres experience maximum force half a cycle apart. While the period of the flow is longer, around 8.9, this cycle consists of two peaks per cycle. Unlike previous cases, the spheres experience equal drag forces, although offset by one half cycle. The repulsive force between the spheres follows a similar pattern.

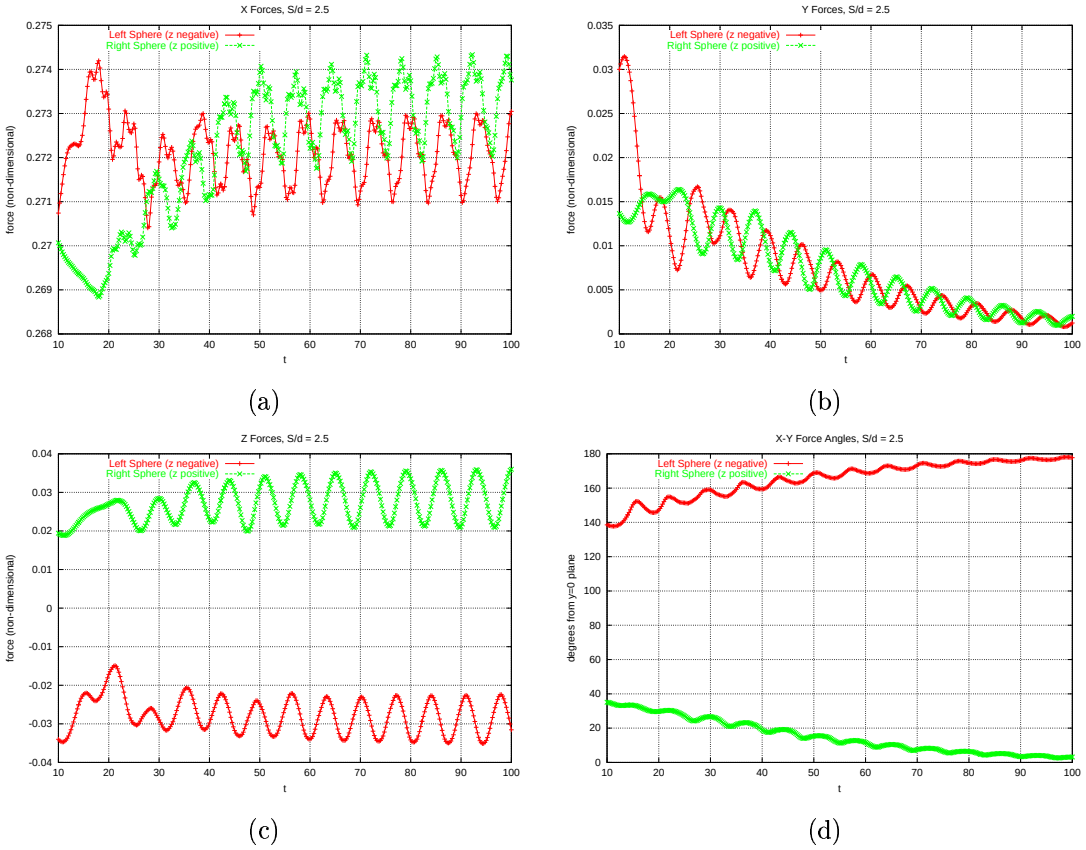

Figure 8.3: Forces on two spheres, $S/d = 2.5$.
(a) axial forces, x direction. (b) sideways forces, y direction. (c) up/down forces, z direction. (d) angle of force in $y - z$ plane.

S/d	C_d	C_L
1.5	0.75	0.099
2.5	0.69	0.073
3.5	0.67	0.071
∞	0.66	0.069

Table 8.1: Drag and lift coefficients of two sphere flows. Separations of ∞ represents single sphere flow from previous chapter.

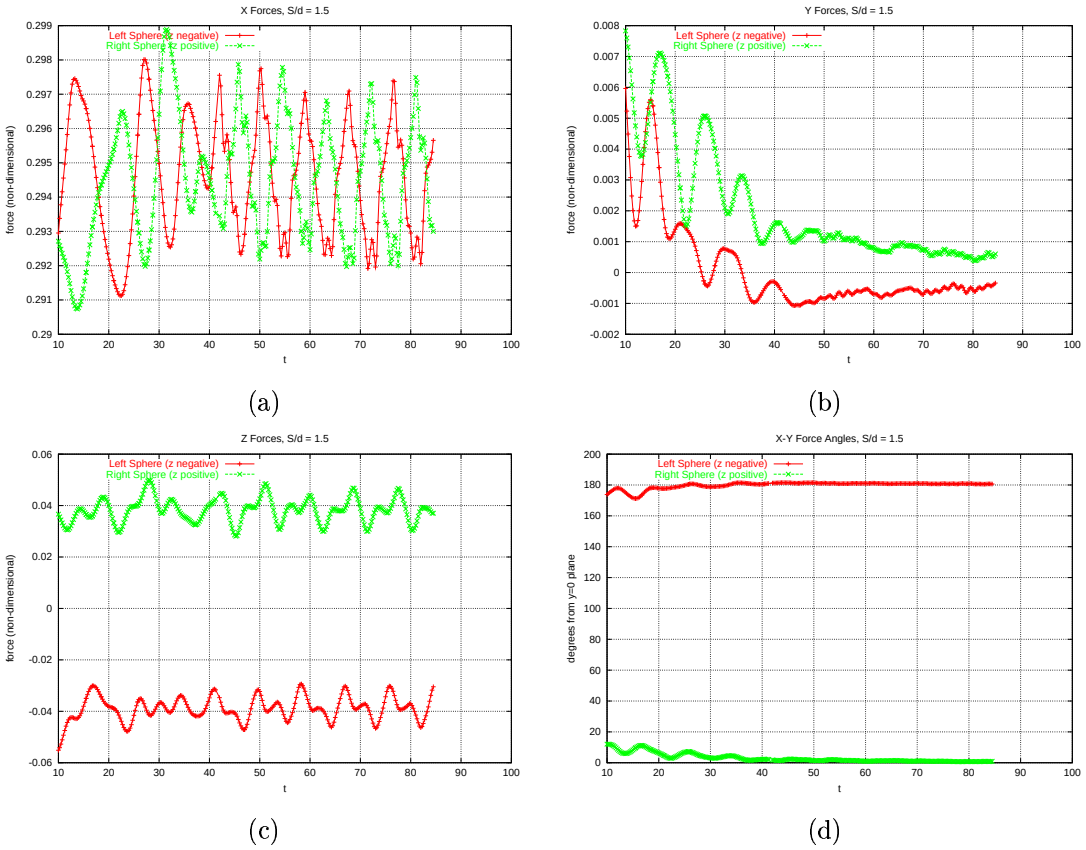

Figure 8.4: Forces on two spheres, $S/d = 1.5$.

(a) axial forces, x direction. (b) sideways forces, y direction. (c) up/down forces, z direction. (d) angle of force in $y - z$ plane.

Table 8.1 gives an overview of the average drag and lift experienced by the sphere at different separations. At infinite separations it seems reasonable to assume the single sphere solution, and the coefficients of the previous chapter are given for comparison in this case. The lift coefficients given would perhaps better be called repulsion coefficients, since for $S < 2.5$ the forces in the $y - z$ plane act along the $y = 0$ line to force the spheres apart. The pattern from this data seems to be that both drag on 'lift' are increased as the spheres are brought together. As these are lift co-efficents, the numbers are normalized by area, so that the total force on the two spheres is more than double that of the single sphere flow.

8.5 Flow Quantities

In this section the downstream velocity of the flow is examined directly. While looking at the u_x velocity directly is not especially intuitive, it does allow visualization of regions of retarded flow within the wake.

Figure 8.5 shows the top view of evolution of the wake of the $S = 3.5d$ flow over approximately one cycle. As in the single sphere case, sharp kinks develop in the wake as it convects downstream. As suggested by the force on the spheres, the wakes are not aligned along a plane, and the wakes of each sphere are offset by around a third of a time cycle. Again the apparent breaking-off of the wake is merely an artifact of the contouring, diffusion causes the retardation zone to shrink as it moves downstream.

Figure 8.6 shows the evolution of the wake retardation area when the two spheres are separated by $2.5d$. At this separation it is clear that the wake retardation regions are joining as they move downstream. The sharp downward part of the single sphere wakes line up to form a single structure, and this determines the offset in phase between the two wakes.

With a separation of $1.5d$, Figure 8.7 indicates a rather different flow field for this two sphere flow. The region of flow acceleration around the sphere (in dark blue) is joined into one large loop around the two spheres. In a relatively short distance downstream, the two retarded flow regions merge. As the flow progresses downstream, an asymmetric wedge-shaped region is formed, joined alternately at the top and bottom of this region to the next wake downstream. The region joining the cross-stream structures is moved up and down in the y direction, perpendicular to the spheres, as the flow progresses downstream. Figure 8.8 shows the same region as viewed from the right side, on the positive z axis. This view shows that although the net forces on the in the y direction are small, as the wake moves down stream, the size of the wake grows significantly in this direction. The wedge shaped region of retardation from the previous image join these regions.

In Figure 8.9, a cross-section of the downstream velocity over one cycle through the $y = 0$

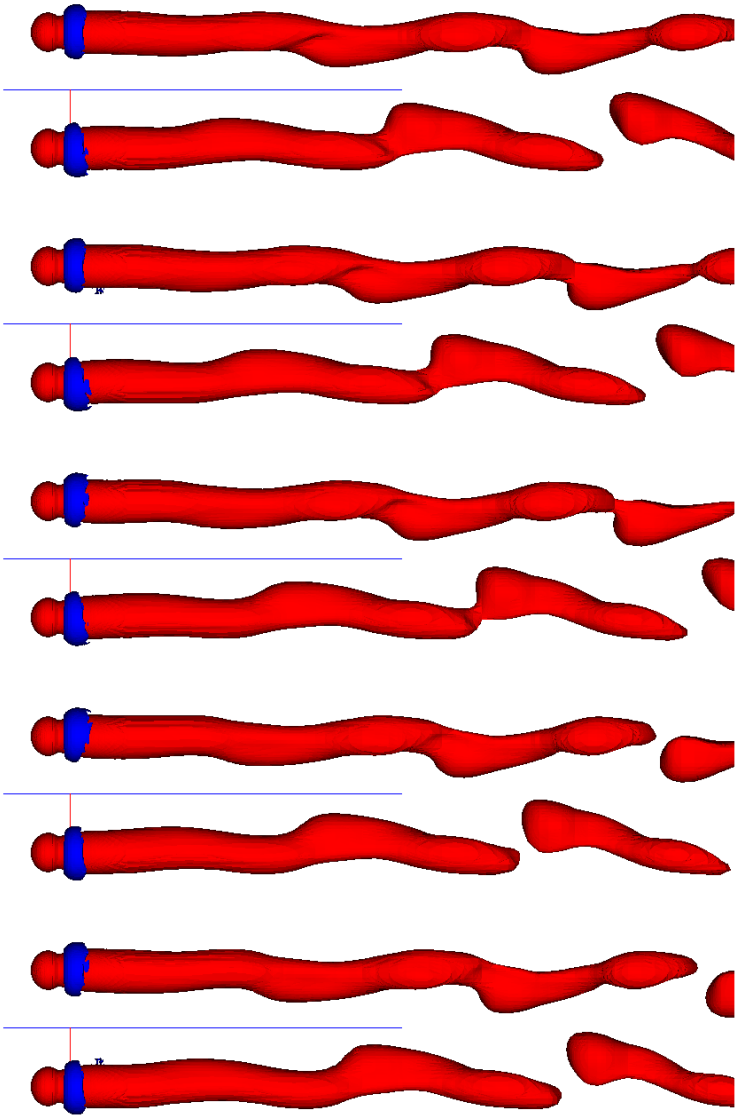

Figure 8.5: Stream-wise velocity, u_x, in wake of sphere, $Re = 300$. $S/d = 3.5$. Top view. Times are, from top to bottom, $t = 102.5$, 104, 105.5, 107, 108.5. Dark blue contour is $u_x = 1.1$, red contour is $u_x = 0.9$.

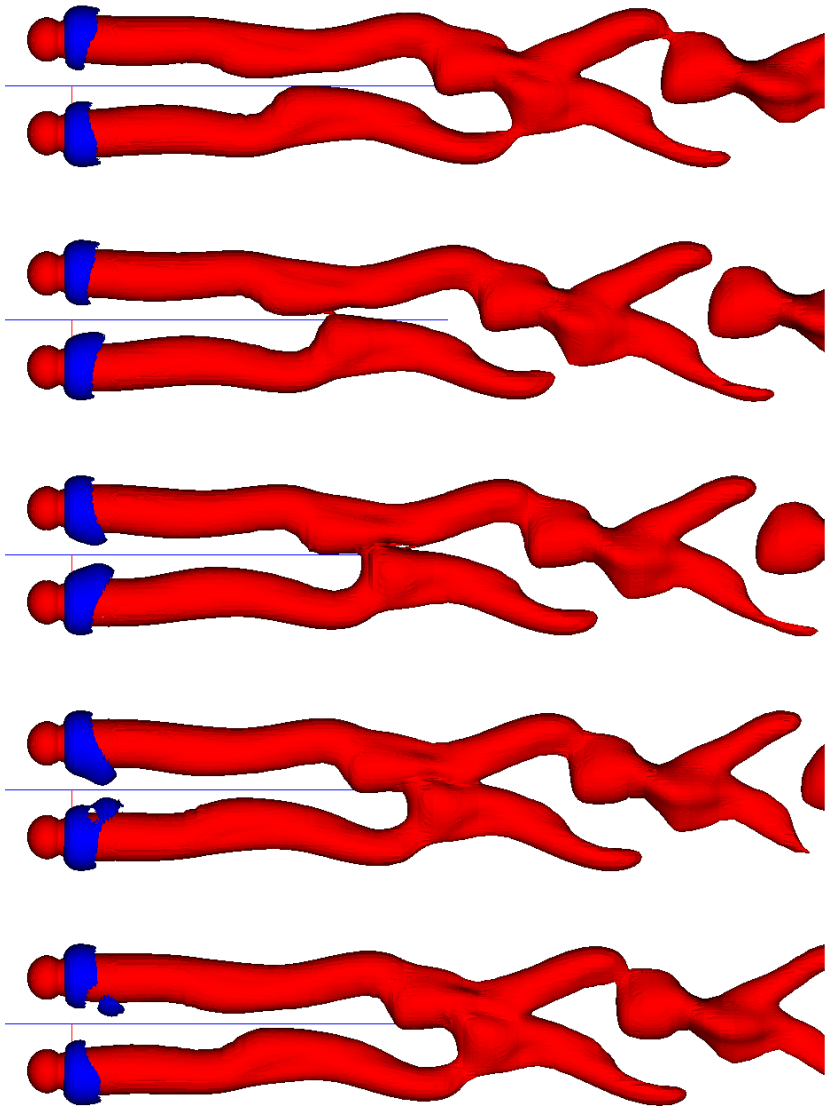

Figure 8.6: Stream-wise velocity, u_x, in wake of sphere, $Re = 300$. $S/d = 2.5$. Top view. Times are, from top to bottom, $t = 102$, 103.4, 104.8, 106.2, 107.6. Dark blue contour is $u_x = 1.1$, red contour is $u_x = 0.9$.

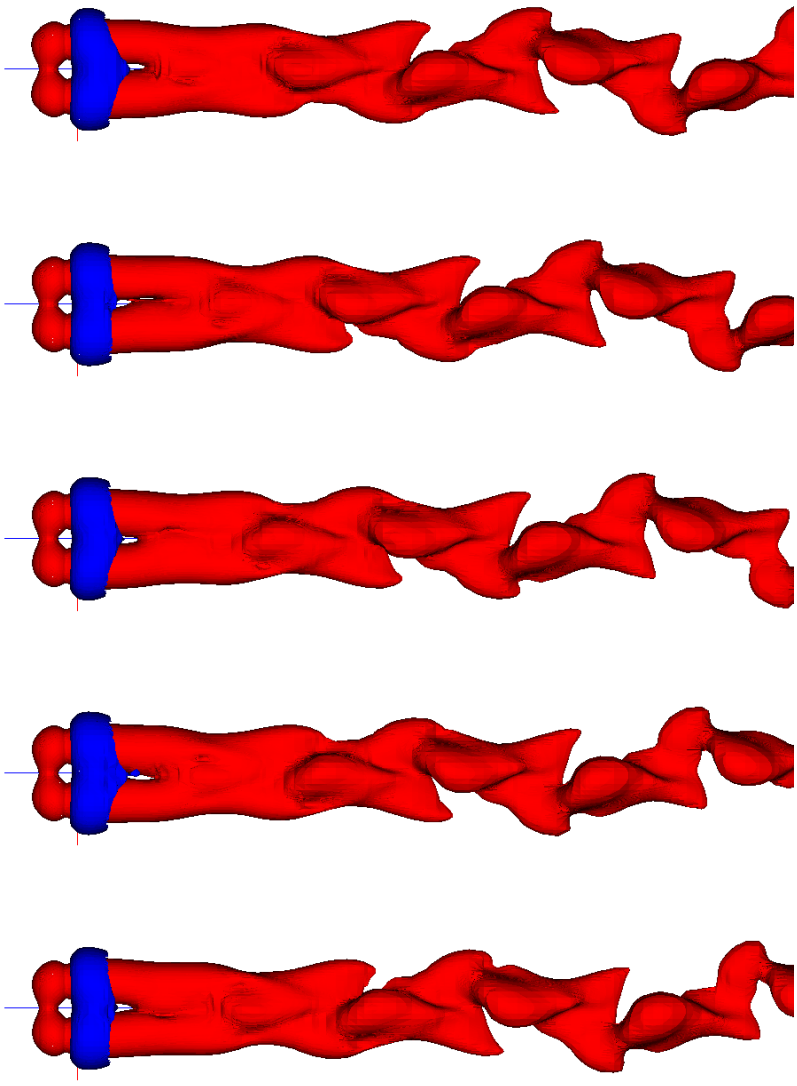

Figure 8.7: Stream-wise velocity, u_x, in wake of sphere, $Re = 300$. $S/d = 1.5$. Top view. Times are, from top to bottom, $t = 86, 87.75, 89.5, 91.25, 93$. Dark blue contour is $u_x = 1.1$, red contour is $u_x = 0.9$.

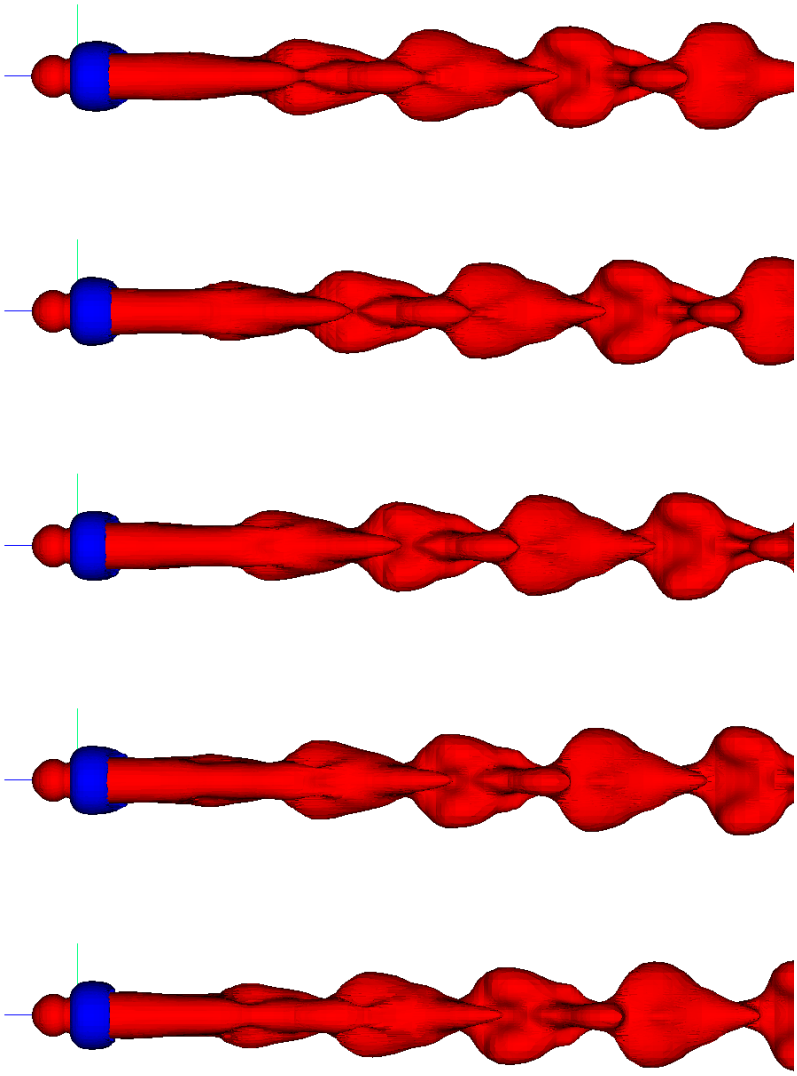

Figure 8.8: Stream-wise velocity, u_x, in wake of sphere, $Re = 300$. $S/d = 1.5$. Side View. Times are, from top to bottom, $t = 86, 87.75, 89.5, 91.25, 93$. Dark blue contour is $u_x = 1.1$, red contour is $u_x = 0.9$.

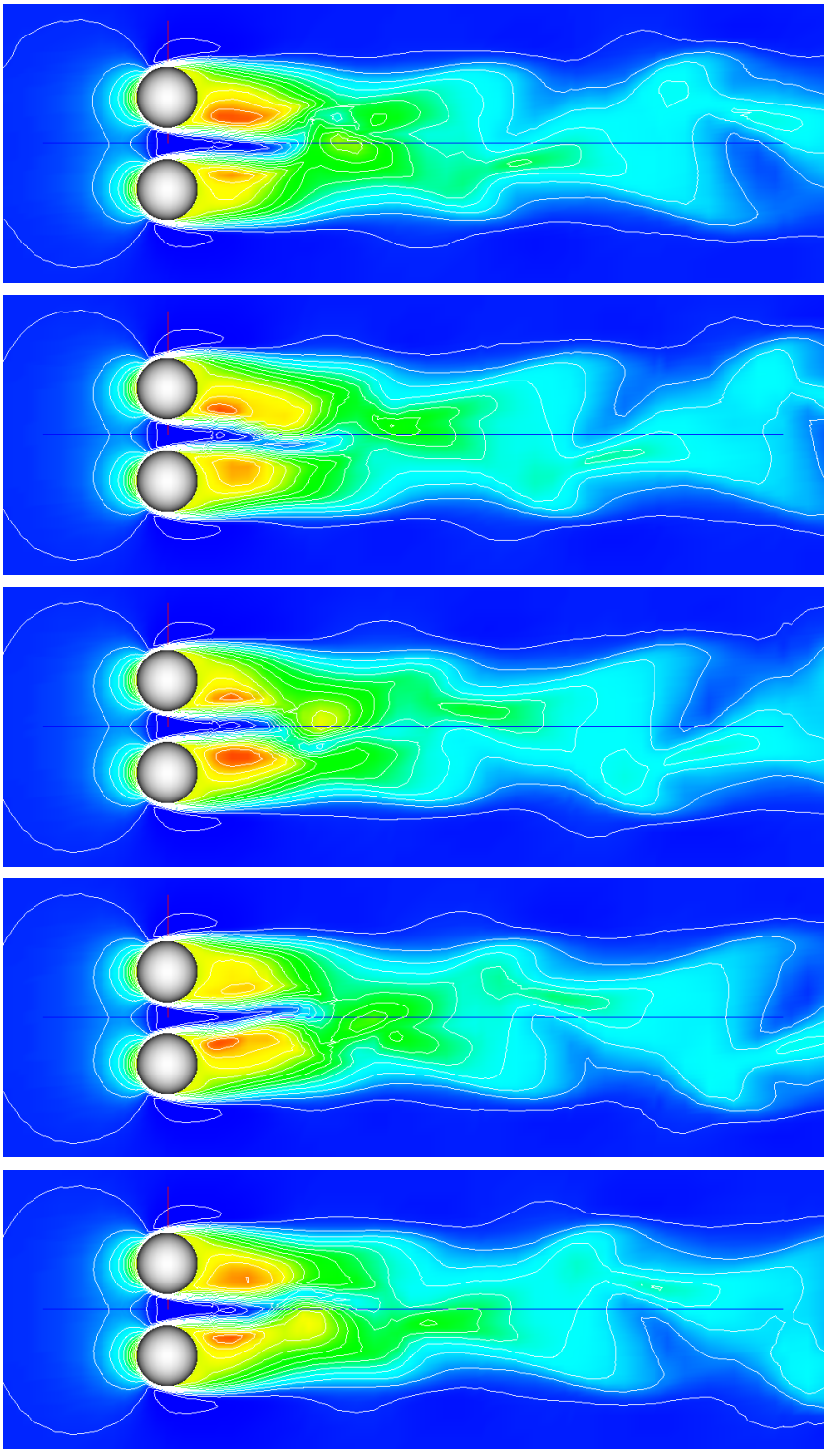

Figure 8.9: Stream-wise velocity cross-sections. $x-z$ plane. u_x in wake of sphere. $Re = 300$. $S/d = 1.5$. Times are, from top to bottom, $t = 86$, 87.75, 89.5, 91.25, 93. 17 contours, $-0.5 \leq u_x \leq 1.1$, blue contours positive.

plane is given. The dark red region, representing the region of greatest flow retardation, is moved significantly towards the centerline compared with the single sphere flow, where this area is centered on the rear of the sphere. The region of dark blue, representing relatively fast downstream motion, between the two spheres indicates that the blockage between the two spheres is still far from complete in spite of the relatively small gap size of half a diameter. In the wake, the previously seen asymmetric wedge region is again visible.

8.6 Flow Vortex and Vorticity

In the current section several derivative quantities are examined for the interacting sphere problem. As the order of the mesh used in this section is seventh, rather than eighth order mesh used in the previous chapter, the contours are less smooth. However, these derivative quantities compare well in structure with those seen in the previous chapter, suggesting useful information is still present in these flow fields.

At a separation of $3.5d$, the vorticity $(\nabla \times \mathbf{u})_x$ of Figure 8.11 shows two wakes which are largely unaffected by each other. Each vortex pattern is similar in structure to the vorticity of the single sphere case, shown in Figure 7.19 of the previous chapter. Each of these vortex patterns is rotated from the axis, although as mentioned previously, at this separation the wakes are rotating slowly over time.

In contrast, Figure 8.11 shows that at a separation of $2.5d$, the vorticity in the wake begins to interact as the wakes move downstream. This interaction is also asymmetric, with the larger vorticity loop (the larger hairpin from the single sphere flow) being draw up into the top wake, while larger loop of the left sphere (shown on top) is largely unaffected.

For flow with a separation of 1.5 diameters, a significantly more complicated picture emerges from the vorticity, as seen in Figures 8.12 and 8.13. The two distinct wakes apparent at larger separation are no longer evident. Rather, a combined wake of somewhat more complicated structure emerges.

Each structure in the downstream wake consists of three large components. These structures occur in pairs, with one being orientated towards the left and and the other to the right. To aid in description, the structure with the bulk it's vorticity towards to top of the page in Figure 8.12 will be called an 'left' vortex. The orientation is, of course, arbitrary since they structures come in pairs.

The first notable component of this larger 'left' structure is a vortex pair in the center. In the side view of Figure 8.13, it is clear that this pair of vortices extends out away from the vortex core, and grows as the wake moves downstream. This vortex pair corresponds to the diamond-shaped vertical retardation zone observed in the downstream flow velocity.

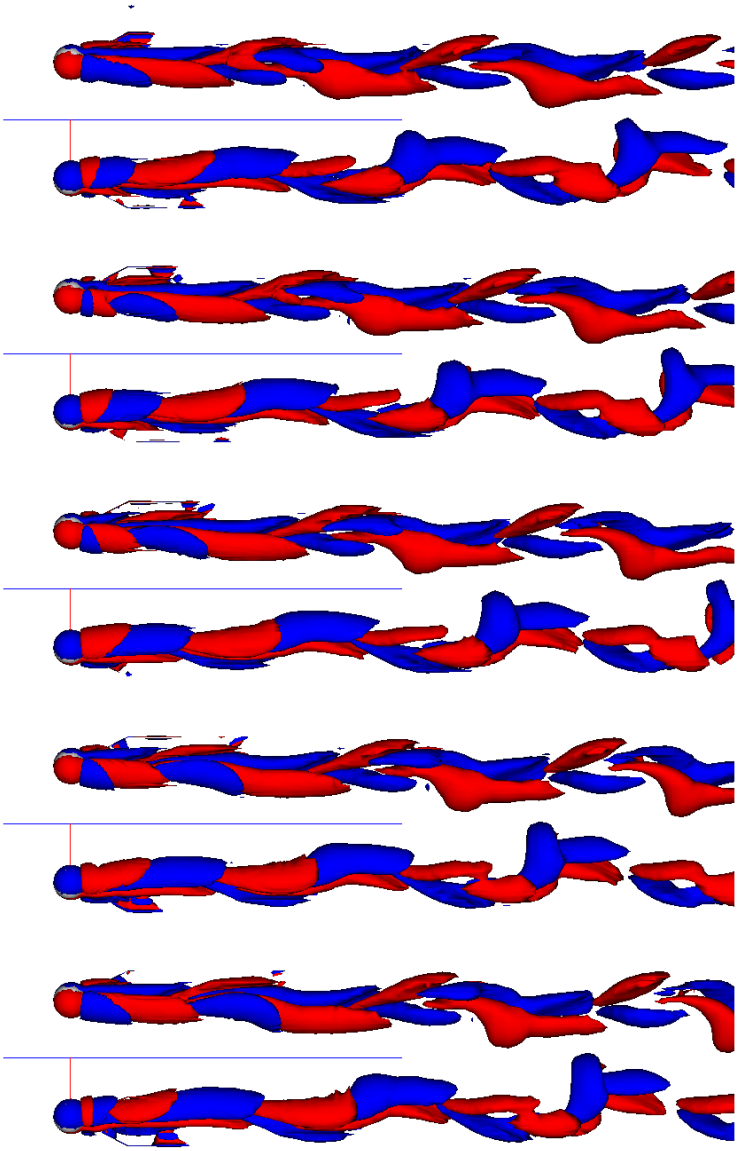

Figure 8.10: Axial vorticity, $(\nabla \times \mathbf{u})_x$, in wake of sphere, $Re = 300$. $S/d = 3.5$. Top view. Blue contour is $(\nabla \times \mathbf{u})_x = 0.1$, Red contour is $(\nabla \times \mathbf{u})_x = -0.1$, Times are, from top to bottom, $t = 102.5$, 104, 105.5, 107, 108.5.

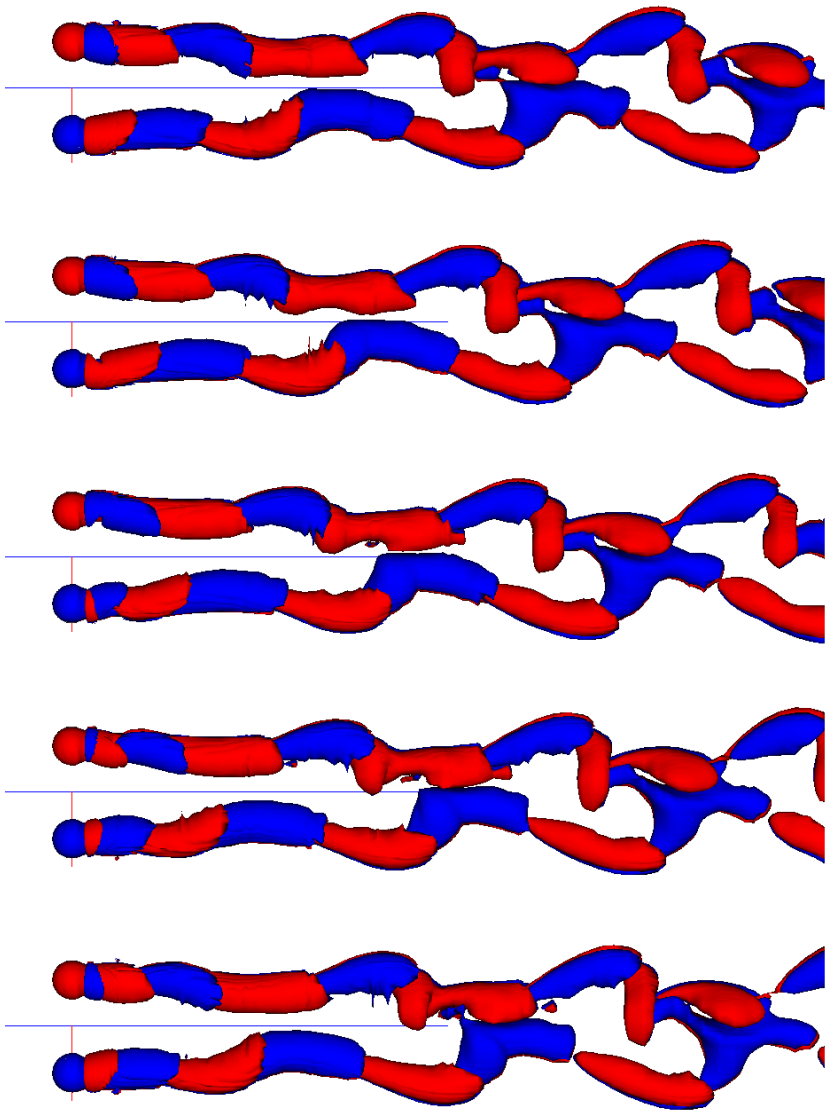

Figure 8.11: Axial vorticity, $(\nabla \times \mathbf{u})_x$, in wake of sphere, $Re = 300$. $S/d = 2.5$. Top view. Blue contour is $(\nabla \times \mathbf{u})_x = 0.1$, Red contour is $(\nabla \times \mathbf{u})_x = -0.1$, Times are, from top to bottom, $t = 102$, 103.4, 104.8, 106.2, 107.6.

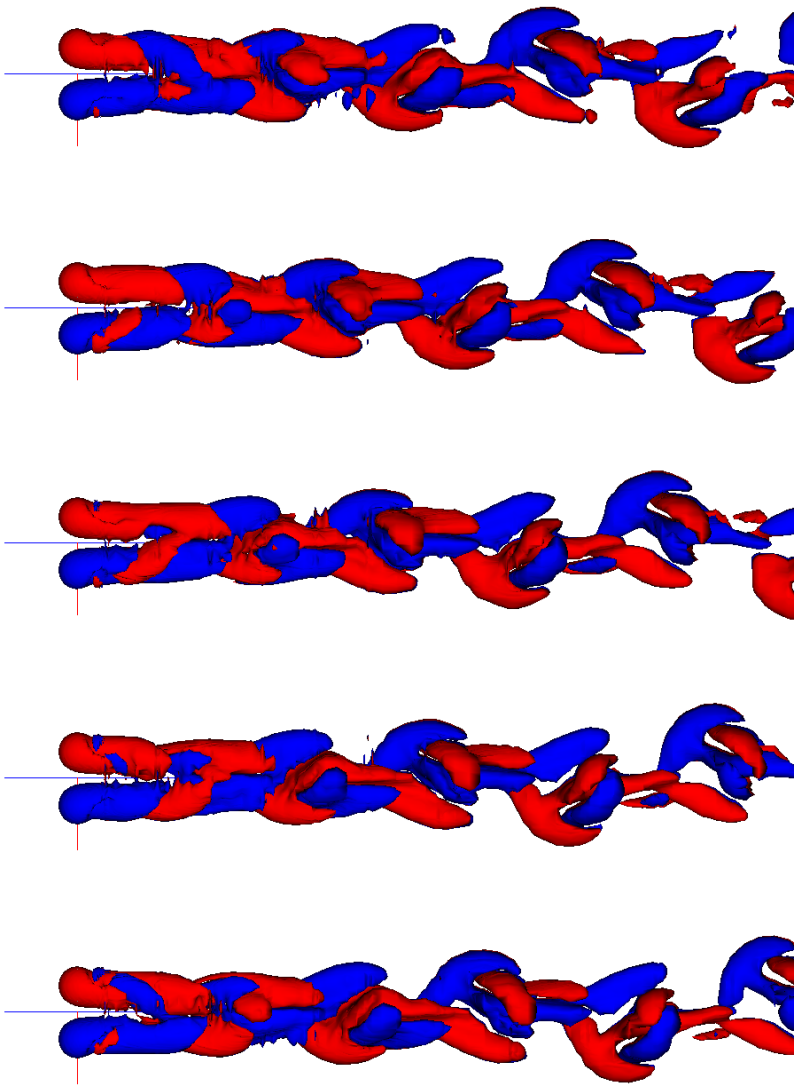

Figure 8.12: Axial vorticity, $(\nabla \times \mathbf{u})_x$, in wake of sphere, $Re = 300$. $S/d = 1.5$. Top view. Blue contour is $(\nabla \times \mathbf{u})_x = 0.1$, Red contour is $(\nabla \times \mathbf{u})_x = -0.1$, Times are, from top to bottom, $t = 86, 87.75, 89.5, 91.25, 93$

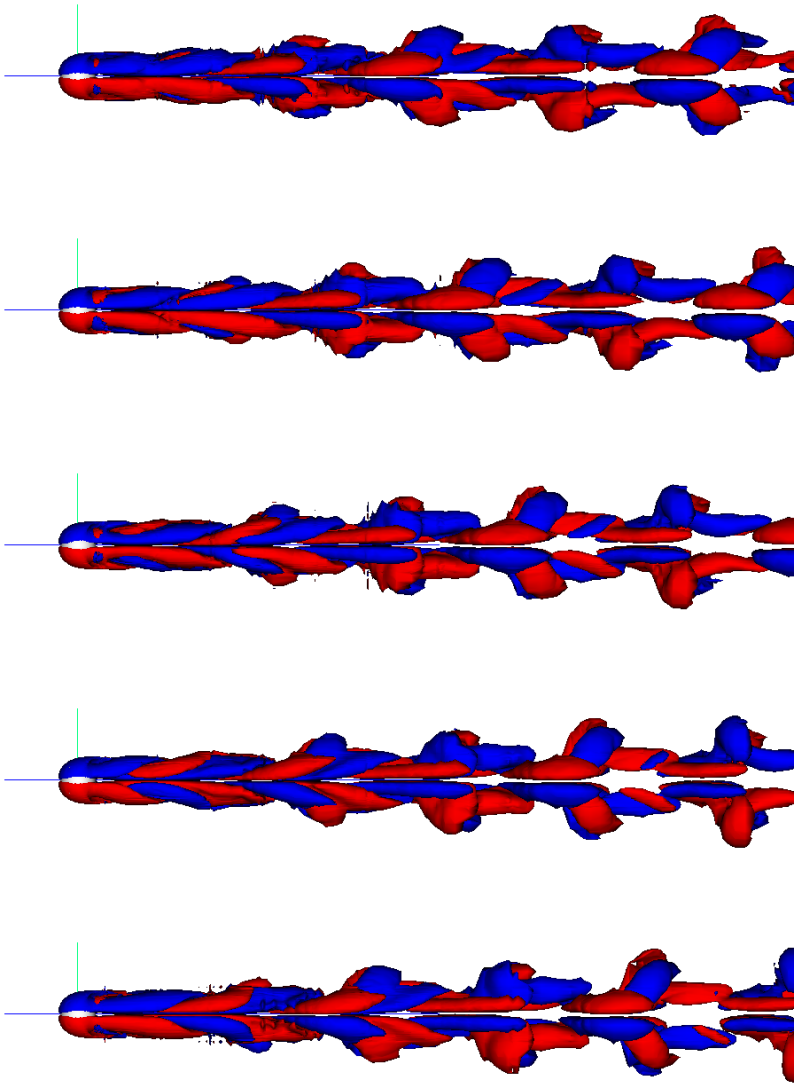

Figure 8.13: Axial vorticity, $(\nabla \times \mathbf{u})_x$, in wake of sphere, $Re = 300$. $S/d = 1.5$. Side view from positive z axis. Blue contour is $(\nabla \times \mathbf{u})_x = 0.1$, Red contour is $(\nabla \times \mathbf{u})_x = -0.1$, Times are, from top to bottom, $t = 86$, 87.75, 89.5, 91.25, 93

This vortex pair is also turning with respect to the wake as it moves downstream, so that by outflow it seems to be near to perpendicular with the flow. Also of note is that the vortex pair is not aligned along the x plane when viewed from above, but rather has a direction towards the left of the flow. As expected from symmetry, the ω_z vorticity is zero on the $y = 0$ plane, and clearly this symmetry is very well developed by this stage in the simulation.

The second visible component of this larger structure, when viewing the 'left' structure from the top, is a C-shaped vortex region surrounding the previously mentioned vortex core. An arch of positive (blue) vorticity moves to the left of the wake (which is the top of Figure 8.12), while negative vorticity moves to the right. Since the wake is symmetric along the $x - z$ plane, a view from the bottom gives the opposite values. These structures are responsible for the asymmetric wedge-shaped retardation region observed in the downstream velocity.

The final component of each larger wake structure is a relatively small vortex pair joining the previously two components together. This vortex pair, which has opposite sign to the first component, seems to be reducing in strength as it is convected downstream.

The final method used for visualizing the two sphere wake is to once again evaluate the vortex measure of Jeong and Hussain (1995). As mentioned in the previous chapter, the use of derivatives in this quantity tends to lead to non-smooth contours, and the results presented here show obvious signs of this. However, does provide a simple interpretation of the flow vortex within the wake.

Figure 8.14 shows the flow vortex when the spheres are separated by $3.5d$. As seen in previous visualizations, at this separation, the wake acts largely as two independent sphere wakes. The hairpin structures of the previous chapter are again visible, although unfortunately not as well resolved. It is also clear these vortices are not yet aligned with the axis.

Figure 8.15 again shows the hairpin structure seen in the single sphere flow, although with a separation of $2.5d$ the lining up of the vortex structures is clear. The individual hair-pins are still present, although slightly changed in form due to the interaction between the wakes.

At a separation of $1.5d$ the drastic change in flow pattern is apparent. The familiar hair-pin structure of the single sphere flow is no longer present, replaced with a three-component structure which was seen when viewing the axial vorticity. These three components can still be identified, with the large central vortex core still being seen. The C-shaped surrounding vortex is also seen clearly seen using this visualization. The final component of this large-scaled structure is the twin vortices joining the components. Again, these large scale structures occur in pairs, being aligned alternately in the left and right orientation previously mentioned.

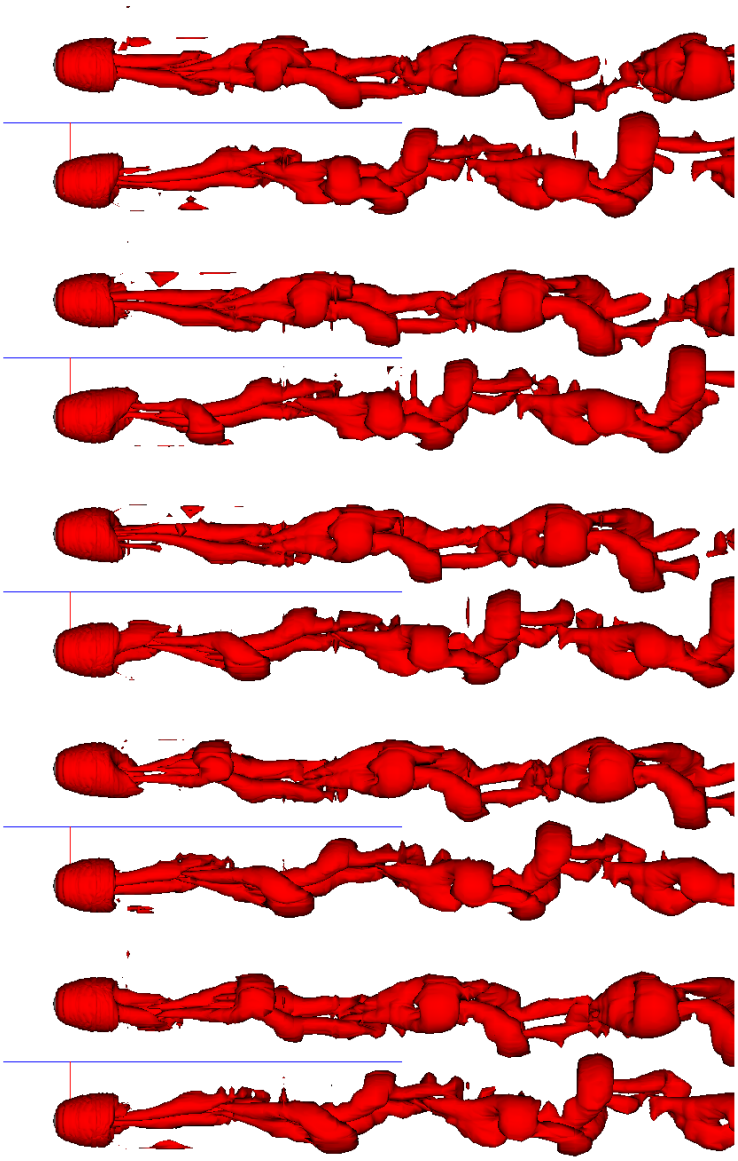

Figure 8.14: Vortex measure in wake of sphere, $Re = 300$. $S/d = 3.5$. Top view. Times are, from top to bottom, $t = 102.5$, 104, 105.5, 107, 108.5.

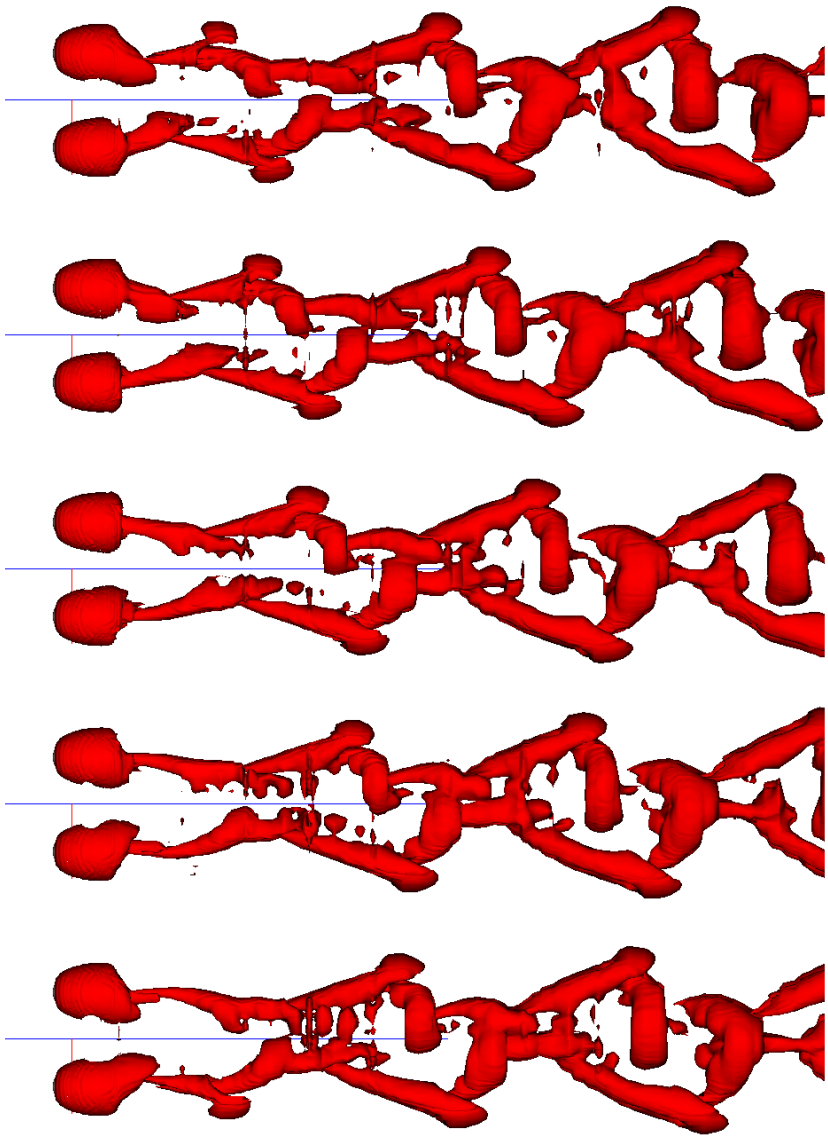

Figure 8.15: Vortex measure in wake of sphere, $Re = 300$. $S/d = 2.5$. Top view. Times are, from top to bottom, $t = 102$, 103.4, 104.8, 106.2, 107.6.

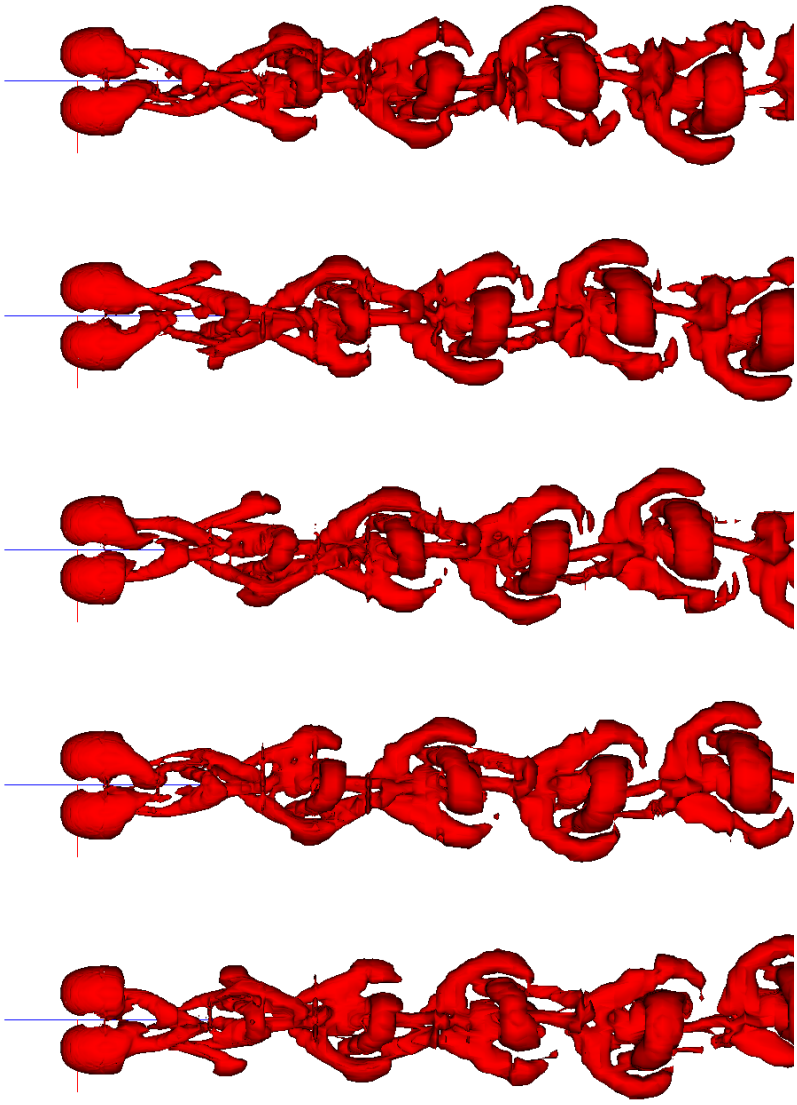

Figure 8.16: Vortex measure in wake of sphere, $Re = 300$. $S/d = 1.5$. Top view. Times are, from top to bottom, $t = 86$, 87.75, 89.5, 91.25, 93

8.7 Conclusion

By implementing a fully three-dimensional spectral element technique, interaction of flow past two spheres has been successfully simulated at several sphere separations. At a Reynolds number of 300, where the single sphere flow is seen to undergo simple shedding, it was shown that the character of the wake changes dramatically as the separation is reduced.

At a separation of 3.5 diameters, the wakes are seen to act largely independently. While it was not possible with the current resources to allow this flow to fully settle down, it is apparent that at this separation the two wakes exert only a very week influence on each other. Weak influences such as the outer container shape seem to have a similar order effect on the wake pattern to the wake interaction.

When the inter-sphere separation is 2.5 diameters, the wake interaction has a greater effect. While the basic wake structure of the two sphere wakes is essentially unchanged, the two wakes are seen to line up. This lining up causes the lifting forces seen in the single sphere flow to act along the line joining the spheres, causing spheres placed side-by-side to be forced in a sidewards direction. In a way similar to the single sphere flow, the wake forces where not symmetric along the plane of symmetry between the two spheres.

At a separation of 1.5 diameters, the changes in the wake structure were more dramatic. The hairpin structure apparent in previous sphere flows was no longer apparent, replaced by a more complicated wake structure. An alternating pair of vortex structures is produced by the two spheres, with each flow structure consisting of three main vortex pairs.

While the full three-dimensional simulation of the two sphere flow has proved to be a substantial computation task, these results demonstrate the interaction of compact bluff-body wakes is a rich in structure. While the current simulations give an insight into the structure of these wakes, further simulations offer a number of possibilities. As well as increasing the resolution of the current simulations, a number of intermediate separations are worth of investigation. It is also not clear from the current work whether hysteresis has a role to play in the wake structure; whether the initial state of the wake has any influence on it's final structure. As well investigating the effect of varying Reynolds number, the two sphere problem also offers several geometric configurations, including one sphere behind the other or offset at different angles.

Chapter 9

Conclusion

This dissertation has outlined the development of an object-oriented finite element and spectral element implementation. This code has been applied to the study of two physical problems; vortex breakdown in a confined swirling cylinder and interaction of compact bluff body flows.

Chapter 2 outlines the basic methods used in the course of the current work. The governing equation, the Navier-Stokes equations, are introduced, and basics of the finite element method are introduced as a means of discretisation for these equations. Differences in implementation between the finite element and spectral element method are discussed.

To approximate the Navier-Stokes equations in time, two approaches are introduced. The first, and seemingly most straightforward, is to assume that the flow is constant in time. To decouple the pressure and velocity in the steady system, a penalty method is used. Some relative advantages and disadvantages of such a scheme are examined. An alternate approach taken to approximate time in the Navier-Stokes, a high order projection method, is reviewed, with modification necessary to deal with axisymmetric coordinate systems also being discussed.

In Chapter 3, an overview of the program structure is given. It is seen that by using a object-oriented structure, much of the complexity inherent in the spectral element method can be abstracted. This abstraction is particularly useful when application of distributed memory programming models are considered. The second part of this chapter examines the parallel performance of several test problems. It has been shown that, even using relatively low-throughput, high-latency networking technology, significant speedups are achieved using up to 48 processors. Not surprisingly, the large three-dimensional simulations were seen to scale best. For the large, three-dimensional problems tackled in later chapters, parallel

spectral element methods provide a good match with the distributed workstation clustes used in this work.

The first problem examined using the current numerical implementation is vortex breakdown flow in a confined swirling cavity. A number of the principal mechanism to describe vortex breakdown are reviewed and compared. Of these theories, the vortex trapping mechanism of Darmofal and Murman (1994) is studied within the context of the confined apparatus. While this breakdown model has proved successful at predicting vortex breakdown in pipe apparatus, it's application to the confined flow is less straight-forward. In particular, onset of vortex breakdown in the cylinder apparatus appears gradually, rather than the sudden change in state observed in the pipe apparatus.

The first test of the wave trapping model for breakdown conducted was to evaluate a wave perturbation equation, using the steady swirling cavity solution as a base flow. By solving for the eigenvalues of possible perturbations, a criteria for the possibility of breakdown is established. When negative eigenvalues are achieved, it is possible for waves to travel back upstream, where it is suggested that the are trapped and amplified. Using this criteria, reasonable correlation was seen between the occurrence of negative eigenvalues and the onset of reverse flow. As with previous studies, negative eigenvalues occur at a Reynolds number somewhat lower than that required for breakdown.

To further test the idea of wave trapping in the confined cylinder, a time-dependant spectral element simulation is used to examine the onset of breakdown for a particular cylinder geometry and Reynolds number. By examining the stream-function at the appearance of the breakdown bubble, it is clear that the onset of breakdown has a feedback effect on the rest of the flow. The increase in bubble size, and more generally the widening of the central vortex core, causes a reduction in the overall circulation of the flow. This in turn reduces the core speed of the central vortex which acts to inhibit vortex breakdown. This feedback provides an explanation to the different nature of vortex breakdown in the confined mechanism, where the size of the breakdown bubble in steady flow is seen to grow gradually with increased Reynolds number.

The second physical problem examined in this thesis is the interaction of compact bluff body flows. To validate the ability of the current code to simulate wake flows, a series of simulations are performed on two dimensional cylinder wakes, were good agreement with previous results is seen in the frequency response of the wake, the drag observed on the cylinder and the pressure at the base of the cylinder. Further simulations are performed on sphere flow up to a Reynolds number of 200, where the wake of the sphere is axisymmetric.

Chapter 7 outlines a series of simulations of flow past a single sphere. With increasing Reynolds number, the flow is seen to change from a axisymmetric wake flow at a Reynolds

number of 200 to a planar symmetric 'double-threaded' flow at a Reynolds number of 250. Simulations are performed at a Reynolds number of 300, where the flow reproduces the previously observed double hairpin vortex. This shedding flow is used to form an initial condition for the interacting two sphere problem of Chapter 8.

Chapter 8 extends the single sphere simulations to deal with flow around two interacting spheres placed side by side. By varying the separation between the two spheres, several different wake structures where produced. At a relatively wide separation of 3.5 sphere diameters, the wakes of the individual spheres were seen to act largely independently. While it was not possible to fully simulate the time evolution of this flow, it was clear that any interaction between the two wakes was generally weak.

With two spheres separated by 2.5 sphere diameters, the two sphere wakes were seen to interact much more strongly. The two wakes were seen to line up on the vertical plane of the two spheres, with the lift forces of the individual spheres acting largely in the left-right direction along the line joining the spheres. The structure of the individual wakes are largely unchanged from that of the single sphere wake, although the drag on lift coefficients on the spheres are increased.

When the spheres are separated by 1.5 diameters, the flow undergoes a more dramatic change. The familiar double-hairpin structure of the single sphere flow, also seen at relatively large separations, is replace with a more complicated, three component vortex structure. This structure, with alternating left and right orientations, leads to an overall symmetric flow pattern, a notable difference from the previous observed sphere wake structures.

While the current implementation has proved successful in simulation a range of physical phenomenon, there is clearly room for improvement. The biggest contribution to the total execution time for large three-dimensional problems is solution of the pressure Poisson equation. While the current preconditioner, Jacobi preconditioning, is simple to implement, it is not particularly effective. Use of a multi-grid preconditioner seems to hold promise as an effective pressure preconditioner.

A second way to increase the speed of the spectral element technique is to use fewer elements. While this will, of course, usually produce less accurate solutions, the use of adaptive mesh refinement provides a mechanism for reducing the number of elements used while maintaining accuracy. The use of adaptive elements increases the complexity implementation, and the current object-oriented framework provides a good framework for implementation of adaptive mesh refinement.

Use of these improved techniques may be necessary for fully study of the interacting sphere problem. First and foremost, improved resolution is necessary to fully confirm the behavior of the interacting wake problem. There are also physical questions yet to be answered about

the interacting sphere flow. It is not clear if hysteresis has a role to play in the wake shape; it would be interesting to start a flow at an intermediate separation based on the flow patterns of close and distant sphere solutions. The effect of the outer container shape on the wake pattern is also worthy of further consideration. Different flow Reynolds numbers and problems geometries are also likely to dramatically influence the flow structure. All of these simulations are likely to take significant computational resources, and improved techniques combined with faster computers will almost certainly be required.

Appendix A

Nomenclature

The following quantities are also used throughout this thesis

$\mathbf{x}$	vector position.
(x, y, z)	position.
(r, θ, z)	axisymmetric position.
$\mathbf{u}$	vector velocity.
u_x, u_y, u_z	Cartesian velocity components.
u_r, u_θ, u_z	axisymmetric velocity components.
p	pressure.
$\overline{\Omega}$	complete domain of solution including boundaries.
Ω	domain of solution excluding boundaries.
$\partial\Omega$	essential boundary.
Γ	natural boundary.
ξ, (ξ, η, ζ)	position on master element.

To avoid confusion between z velocity and weight function $\mathbf{w}$, u_z will always be used to denote the z component of velocity.

Since a variety of notations are in common usage, it is useful to define the following conventions (mainly coinciding with Gresho and Sani (1998)).

ϕ	scalar variable.
$\mathbf{u}$	vector (lower case).
$\mathbf{A}$	tensor (upper case).
$\mathbf{e}_{(\alpha)}$	basis vector in direction α.
$\hat{\mathbf{u}}$	approximate vector quantity (nodal value).
$\hat{a}$	approximate scalar quantity (nodal value).
$\phi_j(x,y,z)$	global shape function j.
$\psi_i(x,y,z)$	global trial function i.
$\hat{\phi}_j(\xi,\eta,\zeta)$	element shape function j, a function of the master element position.
$\hat{\psi}_i(\xi,\eta,\zeta)$	element trial function i, a function of the master element position.
$\int_\Omega$, $\int$	integration on interior of domain.
$\int_{\partial\Omega}$	natural boundary integral.

The following summation convection is used: Indices without brackets are summed over, whereas bracket indices are never summed over. Greek indices are used to represent vector components and Latin indices represent indices of shape functions.

Appendix B

Cylindrical-Polar Stream Function

To evaluate the stream function in axisymmetric coordinates, we define the stream function ψ so that

$$\mathbf{u} = \nabla \times \left(\frac{\psi}{r} \mathbf{e}_\theta \right) \tag{B.1}$$

which for axisymmetric coordinate implies

$$u_r = -\frac{1}{r}\frac{\partial \psi}{\partial z} \tag{B.2}$$

$$u_z = +\frac{1}{r}\frac{\partial \psi}{\partial r}. \tag{B.3}$$

$$\tag{B.4}$$

The $1/r$ scaling is required to make ψ constant on streamlines (Acheson (1990), page 173.). Substituting equation (B.1) for the θ component of vorticity gives

$$(\nabla \times \mathbf{u})_\theta = \frac{\partial u_z}{\partial r} - \frac{\partial u_r}{\partial z} = +\frac{1}{r}\frac{\partial^2 \psi}{\partial r^2} + \frac{1}{r}\frac{\partial^2 \psi}{\partial z^2} - \frac{1}{r^2}\frac{\partial \psi}{\partial r}. \tag{B.5}$$

When $\mathbf{u}$ is know, the stream-function can be evaluated by solving the elliptic equation

$$\nabla^2 \psi - \frac{2}{r}\frac{\partial \psi}{\partial r} = \nabla \times \mathbf{u} \tag{B.6}$$

with appropriate boundary conditions on ψ.

Bibliography

Acheson, D. (1990). *Elementary Fluid Dynamics*. Oxford applied mathematics and computing science series. Oxford University Press Inc., New York.

Anderson, E., Bai, Z., Bischof, C., Blackford, S., Demmel, J., Dongarra, J., Du Croz, J., Greenbaum, A., Hammarling, S., McKenney, A., and Sorensen, D. (1999). *LAPACK Users' Guide*. Society for Industrial and Applied Mathematics, Philadelphia, PA, third edition.

Balay, S., Gropp, W. D., McInnes, L. C., and Smith, B. F. (2000). PETSc 2.0 users manual. Technical Report ANL-95/11 - Revision 2.0.29, Argonne National Laboratory.

Bar-Yoseph, P., Roesner, K., and Solan, A. (1992). Vortex breakdown in the polar region between rotating spheres. *Physics of Fluids*, 4(8):1677–1686.

Becker, E. E., Carey, G. F., and Oden, J. T. (1981). *Finite Elements, An Introduction*, volume I of *The Texas Finite Element Series*. Prentice-Hall.

Benjamin, T. (1962). Theory of the vortex breakdown phenomenon. *J. Fluid Mechanics.*, 14:593–629.

Benjamin, T. (1967). Some developments in the theory of vortex breakdown. *J. Fluid Mechanics.*, 28:65–84.

Beran, P. S. (1994). The time-asymptotic behavior of vortex breakdown in tubes. *Computers Fluids*, 23(7):913–937.

Berger, S. and Eriebacher, G. (1995). Vortex breakdown incipience: Theoretical considerations. *Physics of Fluids*, 7(5):972–982.

Bilanin, A. and Widnall, S. (1973). Aircraft wake siddiapation by sinusoidal instability and vortex breakdown. *AIAA Paper*, 73-107.

Bossel, H. (1969). Vortex breakdown flowfield. *Physics. Fluids.*, 12:498–508.

Bossel, H. (1971). Vortex computation by the method of weighted residuals using exponentials. *AIAA J.*, 9:2027–34.

Breuer, M. and Hänel (1993). A dual time-stepping method for 3-d viscous incompressible vortex flows. *Computers Fluids*, 22(4/5):467–484.

Brown, G. and Lopez, J. (1990). Axisymmetric vortex breakdown part 2. physical mechanisms. *J. Fluid Mechanics*, 221:553–576.

Chorin, A. (1967). The numerical solution of the navier-stokes equations for an incompressible fluid. *Bull. Amer. Math. Soc.*, 255:503.

Chorin, A. (1968). Numerical solution of the Navier-Stokes equations. *Mathematics in Computation*, 22:745–762.

Darmofal, D. (1996). Analysis of a conservation law model for axisymmetric vortices in pressure gradients with applications to vortex breakdown. In *AIAA 1996 Aerospace Sciences Meeting.*

Darmofal, D. and Murman, E. (1994). On the trapped wave nature of axisymmetric vortex breakdown. In *25th Fluid Dynamics Conference*, Paper 94-2318. AIAA.

Daube, O. (1991). Numerical simulation of axisymmetric vortex breakdown in a closed cylinder. *Lectures in Applied Mathematics*, 28:131–152.

Dongarra, J. J., Croz, J. D., Hammarling, S., and Hanson, R. J. (1988). An extended set of FORTRAN Basic Linear Algebra Subprograms. *ACM Transactions on Mathematical Software*, 14(1):1–17.

Dyke, M. V. (1982). *An Album of Fluid Motion.* Parabolic Press.

Escudier, M. (1984). Observations of the flow produced in a cylindrical container by a rotating endwall. *Experiments in Fluids*, 2:189–196.

Escudier, M. (1988). Vortex breakdown: observations and explanations. *Prog. Aerospace Sci.*, 25:189–229.

Escudier, M. and Zehnder, N. (1982). Vortex-flow regimes. *J. Fluid Mechanics*, 115:105–121.

Faler, J. and Leibovich, S. (1977). Disrupted states of vortex flow and vortex breakdown. *Physics of Fluids*, 20(9):1385–1400.

Fornberg, B. (1988). Steady viscous flow past a sphere at high reynolds numbers. *J. Fluid Mech.*

Gartshore, I. S. (1962). Some numerical solutions for the viscous core of an irrotational vortex. Technical report, NCR Can. Aero Rep.

Gottlieb, D. and Orszag, S. (1977). *Numerical Analysis of Spectral Methods: Theory and Applications*. SIAM-CMBS.

Grabowski, W. and Berger, S. (1976). Solutions of the navier-stokes equations for vortex breakdown. *J. Fluid Mechanics*, 75:525–544.

Graham, L., Thompson, M., and Hourigan, K. (1995). The torsionally driven cavity: A test case for comparison between experiment and prediction. In *Twelfth Australasian Fluid Mechanics Conference*, pages 295–298.

Gresho, P. and Sani, R. (1998). *Incompressible Flow and the Finite Element Method: Advection-Diffusion and Isothermal Laminar Flow*. John Wiley & Sons Ltd.

Hall, M. (1967). A new approach to vortex breakdown. In *Proc. 1967 Heat Transfer Fluid Mech. Inst.*, pages 319–40. Stanford Univ. Press.

Hall, M. (1972). Vortex breakdown. *Ann. Rev. Fluid Mech.*, 4:195–218.

Harvey, J. (1962). Some observations of the vortex breakdown. *J. Fluid Mechanics*, 14:585–592.

Jeong, J. and Hussain, F. (1995). On the identification of a vortex. *J. Fluid Mech.*, 285:69–94.

Johnson, T. and Patel, V. (1999). Flow past a sphere up to a Reynolds number of 300. *Journal of Fluid Mechanics*, 378:19–70.

Jones, M., Hourigan, K., and Thompson, M. (1998). An investigation of wave trapping as a cause of vortex breakdown in the torsionally driven cylinder. In Thompson, M. and Hourigan, K., editors, *13th Australasian fluid Mechanics Conference*, pages 175–178.

Karniadakis, G., Israeli, M., and Orzag, S. (1991). High-order splitting methods for incompressible navier-stokes equations. *J. Comp. Sphys.*, 97:414.

Karniadakis, G. E. and Sherwin, S. J. (1999). *Spectral/hp Element Methods for CFD*. Numerical Mathematics and Scientific Computation. Oxford University Press.

Karypis, G. and Kumar, V. (1997). A coarse-grain parallel formulation of multilevel k-way graph paritioning algorithm. In *8th Conference on Parallel Processing for Scientific Computing*.

Kim, I., Elghobashi, S., and William, A. (1993). Three-dimensional flow over two spheres placed side by side. *J. Fluid Mech.*, 246:465–488.

Kim, I. and Pearlstein, A. (1990). Stability of the flow past a sphere. *J. Fluid Mech.*, 211:73–93.

Kim, J. and Moin, P. (1984). Application of a fractional-step method to incompressible navier-stokes equations. *J. Computational Physics*, 59:308–323.

Kirkpatrick, D. (1964). Experimental investigation of the breakdown of a vortex in a tube. Technical Report CP 821, Aeronaut. Res Counc.

Leibovich, S. (1970). Weakly non-linear waves in rotating fluids. *J. Fluid Mechanics*, 42(4):803–822.

Leibovich, S. (1978). The structure of vortex breakdown. *Annual Review of Fluid Mechanics*, 10:221–246.

Leibovich, S. and Randall, J. (1973). Amplification and decay of long nonlinear waves. *J. Fluid Mechanics*, 3(481-493).

Lessen, M., Signh, P., and Paillet, F. (1974). The stability of a trailing line vortex. part 1. inviscid theory. *J. Fluid Mech.*, 63:753–763.

Lopez, J. (1990). Axisymmetric vortex breakdown part 1. confined swirling flow. *J. Fluid Mech*, 221:533–552.

Ludweig, H. (1962). Zur erklärung der instabilität der über angestellten deltaflügeln auftretenden freien wirbelkerne. *Z. flugwiss*, 10:242–249.

Ludweig, H. (1970). Vortex breakdown. *Dtsch. Luft Faumfahrt Rep.*

Magarvey, R. and Bishop, R. L. (1961). Transition rangs for three-dimenional wakes. *Can. J. Phys.*, 39:1418–1422.

Mager, A. (1972). Dissipation and breakdown of a wing-tip vortex. *J. Fluid Mech*, 55:609–28.

Moore, G. (1965). See http://www.intel.com/intel/museum/25anniv/hof/moore.htm.

Mory, M. and Yurchenko, N. (1993). Vortex generation by suction in a rotating tank. *European Jornal of Mechanics, B/Fluids*, 12(6):729–747.

Nakamura, I. (1976). Steady wake behind a sphere. *Phys. Fluids*, 19(5).

Natarajan, R. and Acrivos, A. (2001). The instability of the steady flow past spheres and disks. *J. Fluid Mech.*, pages 323–344.

Ormières, D. and Provansal, M. (1999). Transition to turbulence in the wake of a sphere. *Physical Review Letters*, 83(1):80–83.

Patera, A. (1989). A spectral method for fluid dynamics: Laminar flow in a channel expansion. *J. Comp. Phys.*, 122:83–95.

Peckham, D. and Atkinson, S. (1957). Preliminary results of low speed wind tunnel tests on a tothic wing of aspect ratio 1.0. Technical Report CP 508, Aeronaut. Res Counc.

Press, W. H., Teukolsky, S. A., Vetterling, W. T., and Flannery, B. P. (1992). *Numerical Recipes in C: the art of scientific computing.* Cambridge University Press, second edition.

Provansal, M. and Ormières, D. (1998). Bifurcation from steady to perodic flow in the wake of a sphere. *Fluid Mechanics*, 326(IIb):489–494.

Randall, J. and Leibovich, S. (1973). The critical state: a trapped wave model of vortex breakdown. *J. Fluid Mech*, 53:495–515.

Ronnenberg, B. (1977). Ein selbsjustierendes 3-komponenten-laserdoppleranemometer nach dem vergleichsstrahleverfahren, angewandt fü"r untersuchungen in ener stationären zylinder-symmetrischen drehströmung mit einem rückstromgebiet. *Max-Planck-Institut für Strömungsforschung*, Bericht 20.

Sakamoto, H. and Haniu, H. (1995). The formation mechanism and shedding frequency of vortices from a sphere in uniform shear flow. *J. Fluid Mech.*, 287:151–171.

Sarpkaya, T. (1971a). On stationary and traveling vortex breakdowns. *J. Fluid Mech.*, 45:545–59.

Sarpkaya, T. (1971b). On stationary and travelling vortex breakdowns. *J. Fluid Mechanics*, 45:545–559.

Sarpkaya, T. (1974). Effect of the adverse pressure gradient on vortex breakdown. *AIAA J.*, 12:602–7.

Schroeder, W., Martin, K., and Lorensen, B. (1998). *The Visualization Toolkit.* Prentice-Hall, second edition.

Shirayama, S. (1992). Flow past a sphere: Topological transitions of the vorticity field. *AIAA Journal*, 30(2):349–358.

Snir, M. and Gropp, W. (1998). *MPI: The Complete Reference (2-volume set).* MIT Press.

Spall, R. (1993). Linear stability of swirling flows computed as solutions to the quasi-cylindrical equations of motion. *International Journal for Numerical Methods in Fluids*, 17:291–300.

Spall, R., Gatski, T., and Grosch, C. (1987). A criterion for vortex breakdown. *Phys. Fluids*, 30:3434.

Squire, H. (1960). Analysis of the "vortex breakdown" phenomenon. part 1. Technical Report 102, Aero. Dept., Imperial Coll., London.

Strikwerda, J. (1984). Finite difference methods for the Stokes and Navier-Stokes equations. *Siam J. Sci. Stat. Comput.*, 5:56–68.

Taneda, S. (1956). Experimental investigation of the wake behind a sphere at low reynolds numbers. *J. Phys. Soc. Japan*, 11(1104).

(Thau), T., Lee, R., and Sirignano, W. (1983). Hydrodynamics and heat transfer in sphere assemblages - cylindrical cell models. *Intl J. Heat Mass Transfer*, 23:1265–1273.

(Thau), T., Lee, R., and Sirignano, W. (1984). Heat and momentum transfer around a pair of spheres in viscous flow. *Intl J. Heat Mass Transfer*, 27:1253–1262.

Thompson, M., Hourigan, K., and Sheridan, J. (1996). Three-dimensional instabilities in the wake of a circular cylinder. *Experimental Thermal and Fluid Science*, 12:190–196.

Tomboulides, A. G. and Orszag, S. A. (2000). Numerical investigation of transitional and weak turbulent flow past a sphere. *J. Fluid Mech.*, 416:45–73.

Tsai, C. and Widnall, S. (1980). Examination of group-velocity criterion for breakdown flowfield. *Physics of Fluids*, 23(5):864–70.

Tsitverblit, N. (1993). Vortex breakdown in a cylindrical container in the linght of continutation of a steady solution. *Fluid Dynamics Research*, 11:19–35.

Vogel, H. (1968). Experementelle ergebnisse über die laminare strömung in einem zylindrichen gehäuse mit darin rotierender scheibe. *Max-Planck-Institut für Strömungsforschung*, Bericht 6.

Wang, S. and Rusak, Z. (1997). The dynamics of a swirling flow in a pipe and transition to axisymmetric vortex breakdown. *J. Fluid Mech.*, 340:177–223.

Werlé, H. (1960). *Rech. Aéronaut.*, 74:23–30.

Williamson, C. (1988). Defining a universal and continuous Strouhal-Reynolds number relationship for the laminar vortex shedding of a circular cylinder. *Phys. Fluids*, 31:2742.

Williamson, C. (1996). Three-dimensional vortex dynamics in bluff body wakes. *Experimental Thermal and Fluid Science*, 12:150–168.

Wu, J. and Faeth, G. (1993). Sphere wakes in still surrondings at intermediate Reynolds numbers. *AIAA J.*, 31:1448.